Master Thesis in Geosciences

Seismic surface wave analysis for the determination of soil shear-strength in sites exposed to landslides

Karl Magnus Nielsen

UNIVERSITY OF OSLO
FACULTY OF MATHEMATICS AND NATURAL SCIENCES

Seismic surface wave analysis for determination of soil shear-strength in sites exposed to landslides

Karl Magnus Nielsen

Master Thesis in Geosciences

Discipline: Petroleum Geology and Geophysics

Department of Geosciences

Faculty of Mathematics and Natural Sciences

UNIVERSITY OF OSLO

June 2, 2008

Tutor: Valerie Maupin (UiO)
This work is published digitally through DUO – Digitale Utgivelser ved UiO
http://www.duo.uio.no
It is also catalogued in BIBSYS (http://www.bibsys.no/english)

Acknowledgements

First of all I would like to thank my supervisor Valerie Maupin at the University of Oslo (UiO) for being helpful during the whole process of writing this assignment. My co-supervisor at the International Centre for Geohazards (ICG, Oslo), Isabelle Lecomte also deserves credit for being helpful and supportive throughout this period.

I would also like to thank Adnand Bitri and Gilles Grandjean at Bureau de Recherches Géologiques et Minières (BRGM, Orléans, France) for letting me visit BRGM and for giving me knowledge about spectral analysis of surface waves.

Other people that I would like to thank for different reasons in relation with this work are Oddvar Longva at the Geological Survey of Norway (NGU, Trondheim) and Arnstein Orten at the IT-division for the department of Geosciences, UiO.

And finally, thanks to all my family and friends for being supportive.

Abstract

Due to its topography and geological history, Norway is subject to high landslide hazard. On the 20th of June, 1996, a submarine land failure near the village of Finneidfjord (Mid-Norway) developed into a retrogressive quick clay slide. 4 people lost their lives. Due to this incidence, the area has been location for several geophysical investigations. During the last one, in the summer of 2007, the International Centre for Geohazards (ICG, Oslo) collected ground penetrating radar, resistivity measurements and seismic data. Analysis of seismic surface waves has received increasing attention from different geophysical communities lately. This assignment, done in collaboration with ICG, is focusing on analysis of the Finneidfjord data with a method called multichannel analysis of surface waves, or MASW. The final objective of this method is to obtain a shear-wave velocity profile with depth. Calculation of a phase velocity versus frequency plot, known as a dispersion image, and velocity inversion are key operations in this method. A visit to Bureau de Recherches Géologiques et Minières (BRGM, Orléans, France) was a part of this thesis work to get training in software and new developments of the MASW technique. Dispersion properties of surface waves are first introduced, then the MASW method is explained and both advantages and limitations discussed. In the end this method is applied to the seismic data collected in the Finneidfjord area in the summer of 2007. The other geophysical data are also presented together with a geological interpretation. Different parts of the investigation area hold separate geological properties and no clear evidence for quick clay is found.

Table of contents

1. Introduction

Due to its topography, Norway is a country which is prone to geohazards. In Mid- and Southeast-Norway where large quantity of quick clay is present, landslides constitute a great threat. During the last couple of millions of years Scandinavia has been covered several times by kilometer thick ice-sheets. The last time this happened was from around 110 000 to 10 000 years before present (Elverhøi 2000). Scandinavia was pressed down by the weight of the ice and when the ice retrieved the relative sea level was 200-220 m higher than what it is today (Høeg 2000). Clay particles eroded by the retrieving ice sheet were deposited in different areas of the fjords produced by the ice. Due to the electrostatic forces of the ions in the saltwater, the flat shaped clay particles were stacked upon each other like playing cards in a card house with large pores filled with water. After the ice retrieved, isostatic forces lifted the marine clay to a level above sea level. During the years, water percolating through the marine clay has removed the ions binding the structure together. If the salt content in the pore water is reduced to under 5 g/liter (Bjerrum 1954) the clay becomes quick (sensitive). Which means that if in addition the exterior pressure exceeds a limit value, the clay structure collapses and the whole material is transformed into a thick liquid. Increase in exterior pressure might be related to ground motion by earthquakes or explosives, loading of rock material onto new areas or construction work. A rise in pore pressure due to heavy precipitation will also weaken the strength of the layer (Longva *et al.* 2003). Quick clay materials do not need a steep descent to be transported. A nearly even terrain surface is all that is needed (Hansen *et al.* 2007).

There have been several large quick clay slides in Norway in the past century. Some of the most famous are the quick clay slide in Trøgstad (Southeastern Norway) in 1967 where 4 people died when a whole area with several buildings were transported 20-200 m away (Furseth 2006). Or the slide in Verdal (Mid-Norway) in 1893 where 116 casualties were reported. One of the most recent large quick clay slides took place in Finneidfjord (Northern Norway) the night of the 20th of June 1996 (Fig. 1.1). Investigation of the morphology of the slide and observation made by eye witnesses suggest that the slide started submarine (Longva *et al.* 2003). Eye witnesses observed bubbles and whirls out on the fjord. Around 30 minutes later, a driver driving on the main road E6 which is located next to the fjord, felt the road shaking and stopped the car. He observed that the beach below the road was gone. Only a

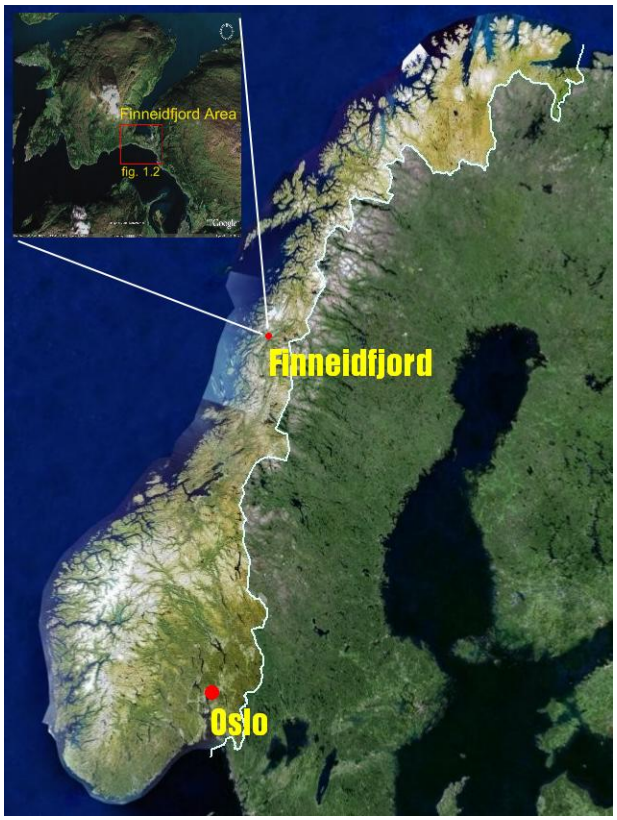

Figure 1.1 Location and overview of the Finneidfjord area. Background photo large image from www.norgeibilder.no. Background photo small image maps.google.no

couple of minutes later, 250 m of the main road E6 broke in three parts and went out into the fjord. The slide also caught a car with one person inside. A nearby house loosened from the ground and sank into the mud and out into the water. Three persons inside did not manage to get out. This slide only lasted for 5 minutes, but triggered slope failure of 1 million m^3 of sediments (Longva *et al.* 2003).

Due to the quick clay slide, the Finneidfjord area has been the location for several geophysical surveys. Janbu (1996) made a reconstruction of the slide by studying available information such as eye witness interviews and sea bottom video investigations. In the following year the Geological Survey of Norway (NGU) carried out a swath bathymetry survey using multibeam echosounder. They also performed high resolution seismics in 1997 and 1998. In addition sediment cores were collected in 1998 and 2001. The conclusion is that this was a retrogressive slide, which means that it started submarine and moved progressively towards land in 5 different stages (Janbu 1996). The high resolution seismic reveals a well defined reflector in large parts of the area at depths varying from 1 to 9 m (Fig. 1.2 right). It is suggested that this strong reflector may be free gas trapped in porous sand layers in between layers of silty clay (Best *et al.* 2003). This layer has been identified as the detachment layer (Longva *et al.* 2003). Several possible trigger mechanisms have been proposed. Gregersen (1999) suggests that the main trigger mechanism is dumping of 12 000 m^3 – 15 000 m^3 of rock material in the fjord's shoreline. These materials were related to tunnel construction work in the nearby area. Another explanation is that excess of pore pressure due to heavy rainfall and a possibly damaged water pipeline led to a further weakening of the initial detachment layer (Longva *et al.* 2003). Several submarine slides have also taken place in the foreshore region since 2006 (Sleipnes 2007). The largest one took place July/August 2006 when 40 000 m^3 of material was transported from the foreshore

region to greater depths. Figure 1.2 (left) displays different important localities marked with yellow numbers. Slide scar is actually visible on the shoreface around 450 m west of line 3 (Fig. 1.2 left, site nr. 5). Road construction work in the area is the most likely cause according to the Norwegian road authorities (Sleipnes 2007). The last submarine slide occurred on the 3rd of November 2006 when 30 000 m^3 of offshore sediments was transported from the foreshore regions to greater depths (Fig. 1.2 left, site nr. 4). This time the Norwegian road authorities concluded that explosives connected with road construction could not be the direct cause of the slide, even though the area was exposed to over 40 mm of precipitation in the few last days before the slide took place (Meteorologisk institutt). Due to the road construction work and the fact that this is a place were there might be a risk for future severe slides, the Norwegian road authorities have performed geotechnical investigations both on-land and off-shore. This has taken place in the western part of the area, see overview in figure 1.2 (left). The data from sediment cores presented in the report indicates that the area is covered by unconsolidated sediments that vary in thickness from 1.8 m to 15.9 m or layers of up to 2 m with dry clay (Sleipnes 2007). Below this package consolidated moraine material was found in most of the core samples, while bedrock (gneiss) was present in just a few. A clay layer with thickness of 10 m has also been found (Fig. 1.2 left, site nr. 2). These clays are not sensitive and hold a shear strength that varies from 15 to 40 kPa. On the contrary a sensitive silt layer has been detected off shore, 2-3 m below the sea bottom (Fig. 1.2 left, site nr. 3). But

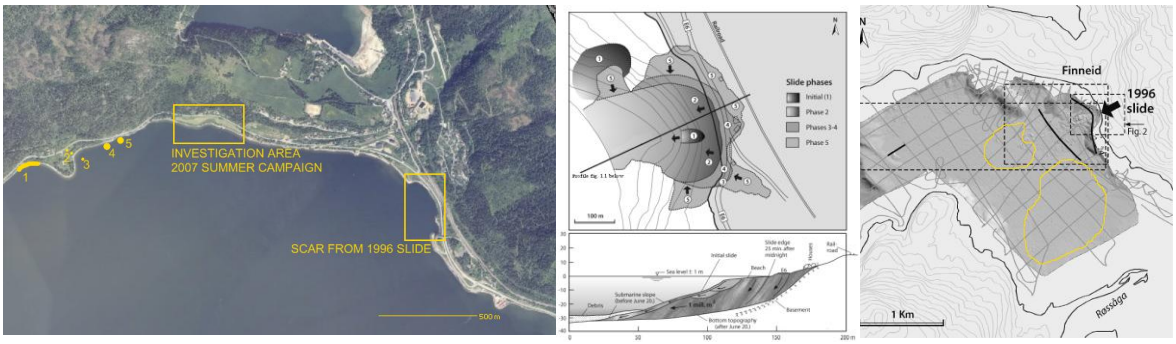

Figure 1.2 Left: Overview of the Finneidfjord area, rectangles displaying the slide scar from the 1996 slide and the 2007 geophysical summer campaign. The Norwegian road authorities have made investigations in the western part of the area and found these important features: site 1, silt and clay material in the shoreline. Site 2, two core samples detecting a 10 m thick layer of clay, not sensitive. Layer is decreasing in thickness towards west. Site 3, detection of a 1 m thick sensitive silt layer. Site 4, slide scar from the last submarine slide in the area in November 2006 involving 30 000 m^3 of sediments. Site 5, slide scar from the submarine slide in July/August 2006. 40 000 m^3 of material transported to greater depths. Yellow rectangle: investigation area for the 2007 summer campaign. Background photo from www.norgeibilder.no **Middle top:** The 5 different stages of the retrograde slide which started submarine and ended subaerial. After Janbu (1996). **Middle below:** Cross section of the slide. Modified after Janbu (1996) and Longva *et al.* (2003). **Right:** Area investigated by NGU. Gray shaded area: swath bathymetry data gathered. Thick black lines and grey grid: high resolution seismic. Yellow areas: detection of free gas trapped in sediments. Modified after Longva *et al.* (2003).

this has only been verified for one of the boreholes. Additional data suggests that the water table is located 0 - 4.5 m below the ground. The Norwegian road authorities concludes that there are no problems related to the ground stability for the existing or the new road, by the premises that no additional rock material is being blown out or dumped in the shoreline or the sea bottom. The area is extremely exposed if a further development of the submarine slides takes place even though rock material is not dumped or blown out (Sleipnes 2007).

To acquire more knowledge about the area, a geophysical campaign took place in the summer of 2007 in an area west of the 1996 slide (Fig 1.2 left). This field work was lead by the International Centre for Geohazards (ICG, Oslo) which also is a collaborator for this master thesis. Different geophysical data will be presented later (Chapter 3). This thesis will focus on a method for determining the shear-strength of the near-surface by analyzing the seismic surface waves, better known as multichannel analysis of surface waves or MASW. During this thesis, I used software for MASW developed at Bureau de Recherches Géologiques et Minières (BRGM, Orléans, France), which I visited at the beginning of the project in order to learn how to use the software. In the first part the surface waves' dispersion properties will be explained. Then the method for surface wave analysis will be detailed before applying it to the Finneidfjord data.

2. Background

2.1 Surface wave data analysis

Spectral analysis of surface waves (SASW) has during the recent years obtained increasingly attention from the geophysical community. This is a fast and non-invasive method for calculating the subsurface' shear-wave velocity with depth (Nazarian *et al.*1983) and/or for determining the lithology. To describe how surface waves are related with the shear-wave velocity some surface wave background is necessary. Information is acquired from the books Stein and Wysession (2003), Reynolds (1997), Kearey *et al.* (2005) and selected articles.

Surface waves are seismic waves trapped in the upper part of the subsurface. There are two types of surface waves; Love and Rayleigh. The difference is the particle motion. The particle motion of a Love wave is perpendicular to the propagation direction and consists of SH waves

trapped in the upper part of the crust. The motion of the Rayleigh wave is more complex and is a combination of P and SV waves, the result is a retrograde ellipse (Fig. 2.1). When seismic sources are triggered such as explosions or earthquakes, most of the energy is transformed into Rayleigh waves. This is one of the reasons why the Rayleigh waves are dominant in a seismogram. Another reason is that the energy spreads two dimensionally which means that at a distance r from the source, the energy decays with r^{-1}. Body waves decay with r^{-2}, hence at large distances the Rayleigh-waves are dominant (Rayleigh 1885). In addition the energy decreases exponentially with depth.

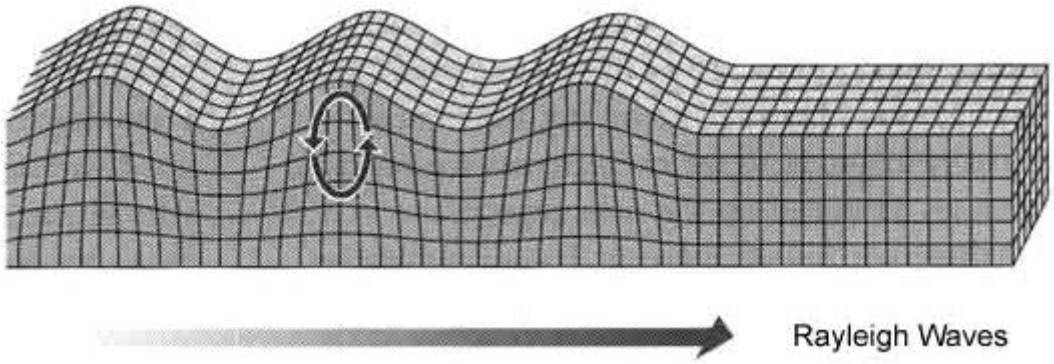

Figure 2.1 Shows the particle motion and the propagation direction of the Rayleigh wave. After Bolt (1982).

Surface waves and dispersion

As opposed to body waves, the surface waves can be dispersive which means that the velocity is frequency dependent. The velocity belonging to a certain frequency is called the phase velocity, V_{phase}. Low frequencies penetrate deeper into the ground than high frequencies. The only setting where non-dispersion qualities exist is in a homogenous half-space. Depth of penetration is proportional to the wave's wavelength. Since velocity increases with depth in most vertically heterogeneous model, the low frequencies usually arrive first in a seismogram. Therefore wavelength is directly linked with depth (Socco and Strobbia 2004). To find a general relationship between the phase velocity velocity (in the horizontal direction) and the shear-wave velocity two conditions must be satisfied. The first one is that a free surface boundary condition is present. The second one is that the displacement vanishes at infinite depth. By using equations for P- and SV- potentials in an homogeneous Poisson's half-space ($V_p^2/V_s^2 = 3$), one find that the apparent velocity, also called surface waves' phase velocity is:

$$V_{phase} = 0.92\, V_s \tag{1}$$

Hence the Rayleigh velocity is less than the shear-wave velocity. This relation is also approximately valid in models which are more complex than a homogeneous half-space.

The surface wave propagation is a multimode phenomenon. After introducing Fourier transformation both in space and time, to multichannel seismic data, we observe that the maximum energy aligns along lines in the frequency versus wavenumber is plane. One mode corresponds to one line (Fig. 2.2). Each frequency (f) within a mode holds a wavenumber (k) and the apparent phase velocity V_{phase} can easily be calculated with equation 2.

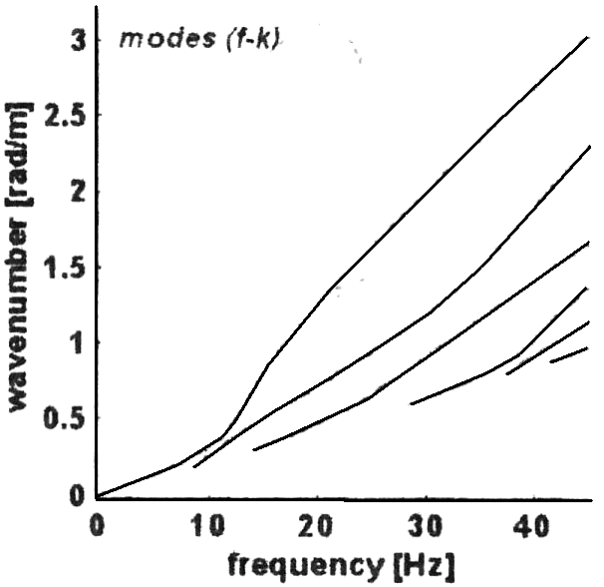

Figure 2.2 After Fourier transformation in time and space. Each line represents different modes and is located at the energy maxima. After Socco and Strobbia (2004).

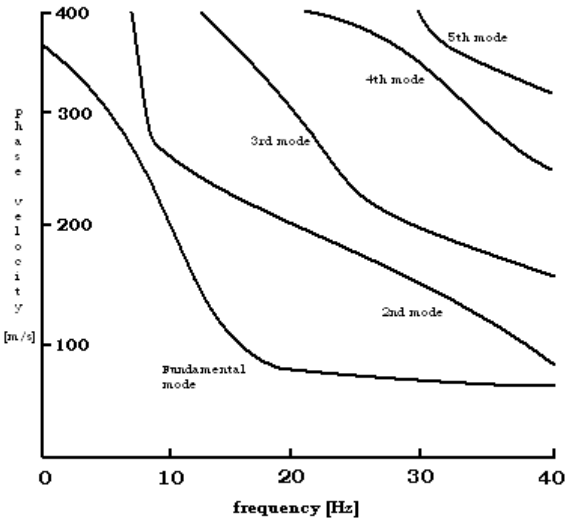

Figure 2.3 Displaying synthetic dispersion curves. Each curve is located at the energy maximum. Different frequencies within a mode, travel with different velocities. Modified after Socco and Strobbia (2004).

$$V_{phase} = \frac{2\pi f}{k} \qquad (2)$$

Equation 2 clearly shows the dispersive qualities of surface waves. The different modes experience different stresses, have different particle displacements and reaches different depths. After transformation by equation 2, the data in figure 2.2 can be put in a phase velocity vs. frequency plot (Fig. 2.3). Maximum energies belonging to different modes are represented as curves. The 1.st and slowest mode is called the fundamental mode, while the higher ones are called overtones. The fundamental mode is usually the most energetic, but velocity inversion in layers might result in high energy overtones.

In an early work with surface waves, Nazarian *et al.* (1983) determined the 1-D shear-wave velocity profile for structures down to 100 m. Only two receivers were used, and phase differences between them were utilized.

Multichannel analysis of surface waves (MASW) was introduced by Park *et al.* (1999 a, b). A seismic array with a number of receivers with regular spacing was put out in

the field. In this experiment the seismic source could both be a sweep source (IVI Minivib) or an impulse source (sledgehammer, weight drop etc.). Sweep sources were preferred if they could be frequency and amplitude optimized for the target. But impulse sources could be transformed into swept ones by using integral operations. After the data were acquired, an integral transformation from the time-offset domain to the phase velocity-frequency domain was applied to obtain a dispersion image (mathematical approach in Appendix A.1). A general description of this procedure is given in the next section. After picking velocities and running depth inversion, the result was a 1-D V_s-profile with depth.

2.2 Computing the dispersion diagram

To calculate the dispersion image, let there first be a single shot gather and apply Fourier transformation to each trace. The next step is to go through every frequency and apply different time shifts Φ to the different traces. This phase shift is related to the trial phase velocity by the relation: The first trace read into the program is the reference trace. The time shift Φ, dependant on the value given, moves the rest of the traces into alignment with the reference trace (Fig. 2.4). Then summation over the traces is added for a final slant stack. A value of Φ will result in a constructive interference and a large amplitude value when the traces are added which corresponds to the true phase velocity. Contrary to a bad chosen value of Φ which will result in destructive interference hence a small amplitude value in the end. This process is repeated for every frequency and the final result is represented in a phase velocity versus frequency plot where different colors represent different energy values (Fig. 2.5). It is now easy to see that more traces will lead to better resolution in the final dispersion image. An important remark to notice is that the maximum energy spread related to one

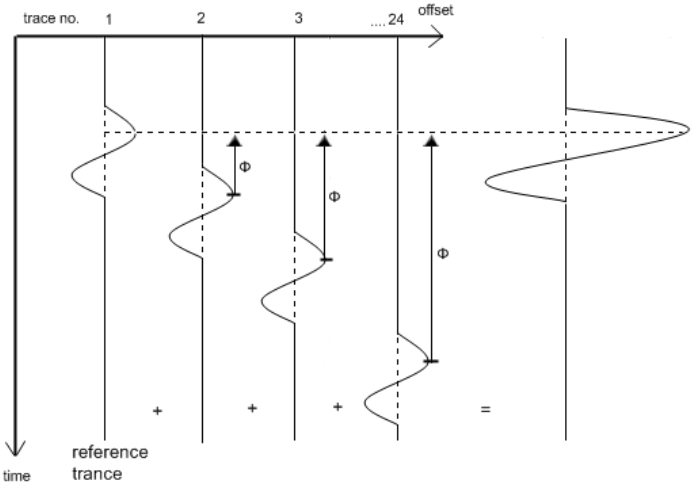

Figure 2.4 The principle for calculating the dispersion image. Every trace in a shot gather is transformed to the frequency domain by Fourier transformation. Each frequency is analyzed separately and different time shift values (linked with different phase velocities) of Φ is applied to align the peak amplitude value of the different traces. The first trace acts as a reference trace. A summation over the different traces is done resulting in a stacked trace. A good chosen Φ will result in a large peak amplitude. Less good values cause destructive interference hence low amplitude.

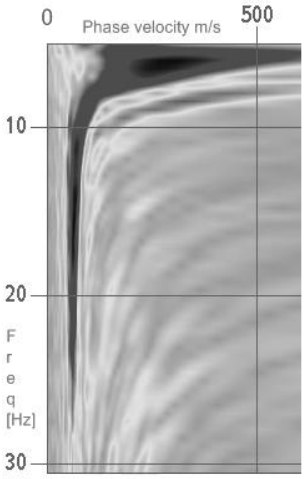

specific frequency is wider for low frequencies than for higher ones. This depends on the velocity uncertainty related to frequency. A change in Φ for low frequencies will not affect the final amplitude of the slant stack as much as if the same change was introduced for a higher frequency. Lower frequencies define the deepest layers in the final model, which mean that the velocity uncertainty is smaller for shallow layers than for deeper ones.

Figure 2.5 Displays a calculated dispersion image. High energy, here represented by dark color, indicates true phase value for a given frequency.

2.3 Inversion

Making the model

The next step is to make a finite 1-D model. The first this task is to create an initial shear-wave velocity versus depth model, then calculate the dispersion curves for this model and compare these synthetic data with real data from the field. After each iteration (calculation) the program updates the initial model, so that this model produces data which match better with the real data. Having a good initial model improves the convergence of the inversion algorithm and reduces the number of iterations. The initial model is based on the criteria defined by Orozco (2003). 4 parameters are set before the calculation can start; P-wave velocity (V_p), shear-wave velocity (V_s), density (ρ) and thickness of different layers. The next element to decide is which parameters are fixed during the inversion. According to Tokimatsu *et al.* (1991) changes in V_p and ρ have very little effect on the dispersion curve, hence they can be fixed. The number of layers has to be limited in accordance with the number of data to avoid over- or under-representation of the model (Socco and Strobbia 2004). Too many layers leads to lower resolution in the different layers and distinct lithological interfaces do not become visible. Too few layers will increase the individual resolution in the different layers, but the pitfall is that one layer only might show the average of two or more layers. To make a good compromise the number of layers is fixed at the number of points defining the picked dispersion curve. The only parameter allowed to change is then V_s.

To set the different parameters in the initial model the dispersion image picks are utilized. Each pick consists of a frequency and a phase velocity (V_{phase}). The depth of investigation (z) of each frequency is found by equation 3. V_s is then calculated by equation 4. Finally the p-wave (V_p) velocity and density (ρ) are calculated by equations 5 and 6.

$$Z = 0.53\,\frac{V_{phase}}{freq.} = 0.53\,\lambda \tag{3}$$

$$V_s(z) = 1.17\,V_{phase} \tag{4}$$

$$V_p(z) = 1.3\,V_s \tag{5}$$

$$\rho(z) = 2.5 - 0.0002\,(4000 - V_p) \tag{6}$$

The initial model is then utilized to obtain a final model by the inversion algorithm by Herrmann (2002). The thickness and depth of a layer influence on how this layer is sampled by the surface waves, hence the resolution of the different layers are different. All Rayleigh wave frequencies travel in the upper layers, while the lowermost layers are visible only to long period waves. If change in thickness and/or velocity in a layer affects the dispersion curve drastically, it means that this layer is well resolved. The model resolution matrix which diagonal holds a number between 0 and 1 can be helpful to determine if a layer is well resolved or not. Non diagonal elements express how the layer affects the other layers in the model (Menke 1989). Figure 2.6 explains the general process between how the picked velocities are linked up with the calculated dispersion curve and the final velocity inverted model. The velocities picked are represented by blue dots (Fig. 2.6 left). With these values the initial model is calculated by equations 3, 4, 5 and 6. After a chosen number of iterations a calculated dispersion curve is obtained (Fig. 2.6 middle) and it is easy to observe the mismatch between this red curve and the picked velocities (black dots). The frequency axis from the dispersion image is transformed into an axis with period as unit. From this calculated dispersion curve a final model is obtained (Fig. 2.6 right). The black dashed line overlapping the final velocity model represents the model before the last iteration.

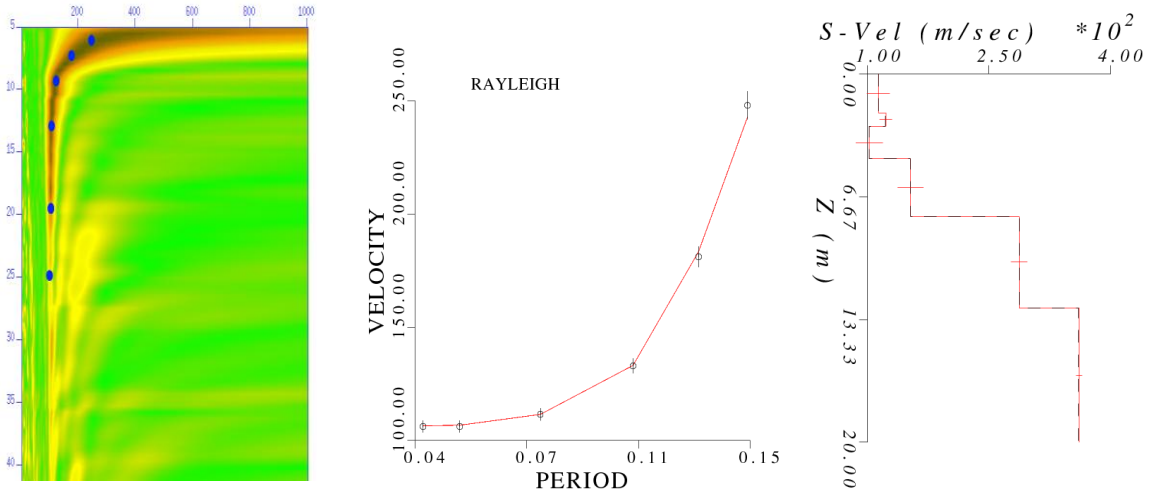

Figure 2.6 Left: Dispersion image with picked velocities represented as blue dots. Horizontal axis is phase velocity. Vertical axis is frequency. **Middle:** Velocity picks from the dispersion image are used to obtain the calculated dispersion curve shown in red color and it is possible to compare the mismatch between this line and the picked velocities (black dots). **Left:** The calculated dispersion curve is used to make the final velocity model, here represented as a red line. The dashed black line represents the model before the last iteration.

When the shear-wave velocity with depth is obtained it is possible to calculate the shear modulus (μ) which is an important geotechnical parameter:

$$\mu(z) = \rho V_s^2 \tag{7}$$

MASW and the computation of a 2-D V_s-profile

The MASW technique introduced by Park *et al.* (1999 a, b) was being developed further by Xia *et al.* (1999) and Miller *et al.* (1999) by interpolating several 1-D shear-wave velocity profiles into a 2-D shear-wave plot. In an experiment for mapping bedrock structures Miller *et al.* (1999) were using 48-channel shot records to calculate 1-D dispersion images. For each shot (distance to the closest receiver was 8 ft and the receiver spacing was 2 ft) a 1-D shear-wave velocity profile was made. Then the source moved 4 ft. A new shot gather was recorded and a new 1-D shear-wave velocity profile was made. This process was repeated along the entire profile (total of ca. 400 ft). After all the 1-D shear-wave velocity profiles were created, an interpolation technique composed a 2-D profile of the entire line. Figure 2.7 displays such a 2-D profile and it clearly shows the boundary between unconsolidated sediments over bedrock. Another special notice is the vertical low velocity zone above station number 2050.

This has been interpreted as a palaeochannel infilled with weathered rock or a fracture/fault zone. In comparison with borehole data there is less than 1 ft of difference in the depth to bedrock.

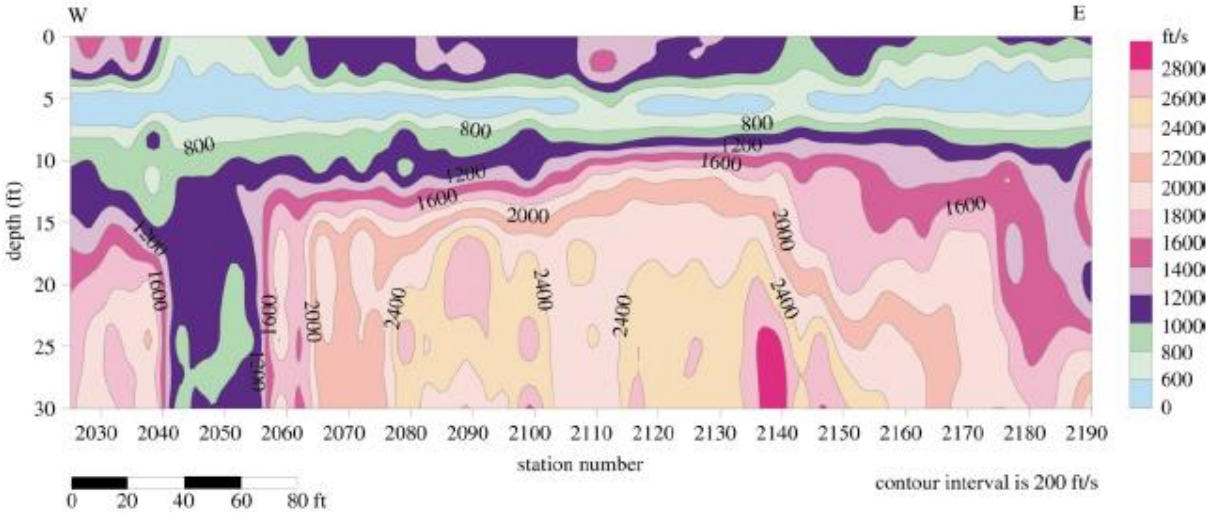

Figure 2.7 A 2-D shear-wave velocity profile. The clear boundary between unconsolidated sediments and bedrock is visible at depth around 12 feet. The vertical low velocity zone above station number 2050 is interpreted to a palaeochannel filled wit weathered rock or a fracture/fault zone. After Miller *et al.* (1999).

A similar technique was utilized by Bohlen *et al.* (2004). In an experiment of recording Scholte-waves (waves similar to Rayleigh-waves, but trapped in the interface between seabed and water column) only one ocean-bottom-seismometer was put out. But several shots from different positions were recorded to study the variation of the Scholte-wave dispersion. After acquisition, different offset windows were chosen for calculation and inversion of the dispersion curves. Lateral variation of shear-wave velocity is obtained by running this process along the seismic profile.

2M-SASW

In order to increase the resolution with the method of Park *et al.* (1999 a, b), one need to make the receiver array longer. This is inconvenient. Grandjean and Bitri (2006) introduced new algorithms which increase the resolution further without increasing the receiver array. Their key step is grouping the receivers into different receiver gathers and perform summation over different dispersion images. For each shot a local dispersion image is computed within a receiver distance window (RDW) which contains a set of receivers. The main assumption is that the layers within this RDW are laterally homogenous. After computing the dispersion images for all the different shots registered by the same RDW, a summation term is

introduced, which sums over the local dispersion images made within the same RDW to create a local dispersion image stack (Appendix A.2). This will increase the signal-to-noise ratio and the resolution of the dispersion images (Grandjean and Bitri 2006). The length of the RDW should be long enough to produce clear dispersion images, but too many traces may mix the effect of lateral velocity changes, therefore a compromise has to be settled. This technique calculates the local dispersion image under the RDW, which implies that the resulting velocity profile is limited to an average velocity within the RDW. This technique is referred to as 2M-SASW: Multifold and Multichannel SASW (Grandjean and Bitri 2006). Further on this means that independent of where the source is located (far or near the first receiver, or on the opposite side of the array), the same apparent dispersion image should be obtained. Of course will the distance to the source influence modal separation, near- and far-field effects etc., but the overall pattern in the image will be the same. Figure 2.8 shows two different dispersion images from the same array, but with shots from opposite sides. They are almost identical and show the dispersion properties under a RDW which is 10 m long (6 geophones).

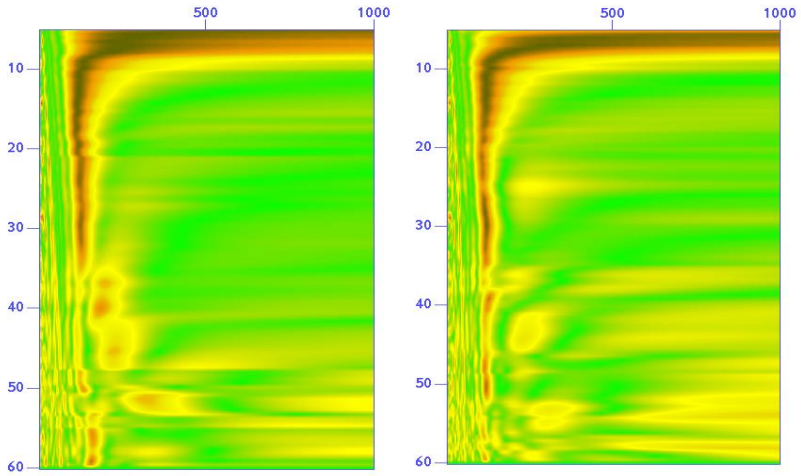

Figure 2.8 Dispersion images obtained from single shots, but from opposite sides of the receiver array. The theory (Grandjean and Bitri 2006) states that these images should be identical. The overall pattern is the same, and the same velocity profile would be the result if inverted. Horizontal axis is phase velocity in m/s. Vertical axis is frequency in Hz. Number of receivers is 6, distance from source to nearest receiver is 10

A general walk through for obtaining a 2-D V_s-profile is then as follows:

1. One defines a length for the RDW, e.g. 10 m. For an array with receiver spacing of 2 m, this will mean that the dispersion is calculated within a window of 6 receivers.
2. For each shot in the seismic survey, both outside and inside the receiver array, a dispersion image is calculated within the same RDW. In the end all the different dispersion images is summed to improve resolution.

3. After picking velocities and inverting these, a 1-D average V_s-profile for the RDW is obtained.
4. Then the RDW is moved e.g. 2 m and a new dispersion image is computed, which means that the velocity profiles are made for 0-10 m, 2-12 m, 4-14 m etc. of the receiver array.
5. Finally all the 1-D velocity profiles are put together and interpolated to a 2-D V_s-profile.

Incomplete usage of the 2M-SASW technique

When working with the 2M-SASW one can use an approximate summation principle. This idea is to define a RDW and gather the traces from all the shots from the survey, then calculate the dispersion image from this gather (Fig. 2.9). At first this looks like the technique mentioned earlier, and the program uses the same algorithm for calculating the dispersion image (Appendix A.2). The error lies at the fact that the first trace read into the program is used as a reference trace for not only the shot belonging to this trace, but for all the traces within the RDW for all the shots. The correct procedure would be to sum the different dispersion images that were calculated for each shot. This incorrect method of calculating the dispersion image, gives the impression that the image is giving dispersion characteristics beneath the RDW. But in reality, this dispersion image is the sum of dispersion characteristics for the distances from the different shots to the RDW. I tried this method on the seismic data from the 2007 summer campaign. The dispersion images had high resolution and allowed for picking phase velocities at low frequencies, but since they display an average velocity for a large area they were not used for velocity inversion.

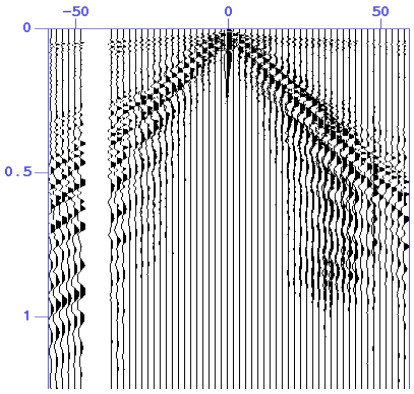

Figure 2.9 Shows a shot gather displaying all the shots from a seismic survey. The RDW consists of 6 receivers, which means that all the traces in this figure comes from these 6 receivers, but from different shots. E.g. the 6 traces to the far left in the figure represent the 6 receivers in the RDW for the shot furthest away to the right side of the array. The error in the method lies in the point that the first trace in this gather is used as a reference trace for velocity calculations for all the other traces. The final result will then not display the dispersion characteristics beneath the RDW, but sum the dispersion characteristics for the distances from the shots to the RDW. Vertical axis is time in seconds. Horizontal axis is distance in meters for the respective trace to the shot.

Since I didn't have the module for summing the different dispersion images together, I only carried out dispersion analysis with a single shot for each velocity inversion. But different RDW are defined so that in the end all the 1-D profiles are put together to obtain a 2-D V_s-profile. This will not lead to as good quality for the dispersion images as the summed 2M-SASW method.

2.4 Pitfalls and limiting parameters related to MASW

Seismic acquisition is the operation of collecting seismic data from the field from a known source in a known location. This may take place either on land or off shore. Well planning is important. The first issue to get into consideration is what is the purpose of the project? Is it to map the interior of the Earth, locate fault zones in the upper crust or maybe look for water reservoirs in the upper tens of meters of the ground? Surface waves propagating in the crust and upper mantle, often regards periods between 5-10 s and sometimes up to 800 s (Keilis-Borok *et al.* 1989). The source is usually an earthquake or large amount of dynamite and the receivers are often three component seismometers. Near surface seismic operates on a different level. The periods can be as small as e.g. 0.02 s. And the receivers consist of light, portable and cheap vertical component geophones. The geophone consists of a transducer which converts the vertical ground motion into an electrical signal. If the soil is soft, the geophones are plugged 10 cm down into the ground. Is it on hard grounds like tarmac or cement, the geophones are put directly on ground with no penetration. To ensure good coupling a metal plate is often used. To choose between on-land sources there are a numerous possibilities; sledgehammer, dynamite, shotgun, weight drops or vibrators. The choice depends on the environmental setting and the desired frequency spectrum. The natural high amplitude of Rayleigh waves compared to body waves makes them useful even in environments where the coherent noise is high (Miller *et al.* 1999).

Array length and number of receivers

The array length is important when it comes to modal separation. For geotechnical studies, typical array length can vary from 2 to 200 meters (Park *et al.* 2007). The length affects the wavenumber resolution Δk, hence long arrays allows for better separation of the different modes. The maximum detectable wavelength is not affected by the array length. Wavelengths longer than the array length can be observed (Socco and Strobbia 2004). The maximum wavelength is dependent on the geological setting of the site. Short arrays also have positive

effects. According to Socco and Strobbia (2004) they are less sensitive to lateral variations, less affected by high-frequency attenuation and given the number of channels, produce less severe spatial aliasing. But short arrays do not allow for modal separation as good as long ones. If a higher mode is interfering with the fundamental one, picking correct velocities can be difficult and may result in an incorrect velocity inversion. If surface wave dispersion is analyzed within an array, a short array would lead to lack of resolution, but a more precise location of the velocity profile. In contrast will a longer array obtain a more accurate velocity profile with depth, but the location is harder to point out (Grandjean and Bitri 2006). This is due to the fact that the velocity is calculated as an average within the array length, there for lateral velocity changes will be harder to recognize in a long array.

In multichannel analysis of surface waves it is common to use 12-48 or more receivers (Socco and Strobbia 2004). The number of receivers is of course linked with array length and receiver spacing and affects the uncertainty of the data. For an estimated wavenumber and a given value of phase uncertainty, a relation between array length and number of receivers states that increasing the array length or number of receivers will reduce the uncertainty (Socco and Strobbia 2004). Figure 2.10 shows the effect of increasing array length and number of receivers. The modes become more focused and separated. And energy that might be noise seems to disappear.

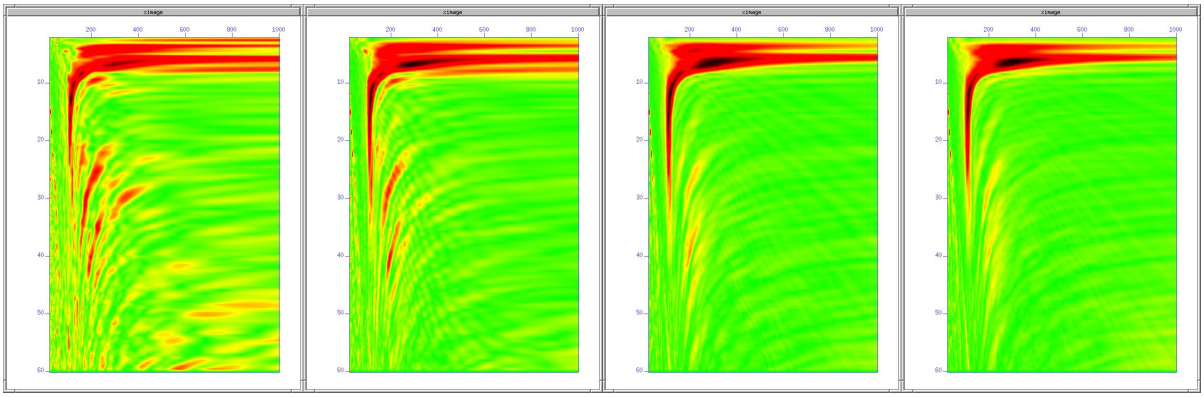

Figure 2.10 Shows the effect of increasing the array length and number of receivers from left to right. Modal separation becomes better. The modes are more focused, and random noise disappears. Array length: 2 m, 10 m, 30 m and 46 m. Number of receivers: 2, 6, 16 and 24. Receiver spacing is 2 m. Horizontal axis is phase velocity in m/s. Vertical axis is frequency in Hz.

Receiver spacing

The receiver spacing is important when it comes to the aspect of aliasing. The maximum frequency recorded without aliasing is easily found using the equation for the Nyquist frequency sampling theorem (Eqn. 8).

$$f_{nyq} = \frac{1}{2\Delta t} \tag{8}$$

Where Δt is the sampling interval in time. On the right hand side we can substitute $\Delta t = \Delta x/c$, where c is the velocity and Δx is the receiver spacing. Then the expression looks like this:

$$f_{nyq} = \frac{c}{2\Delta x} \tag{9}$$

Energy related to $f > f_{nyq}$ will be aliased. Further by replacing $c = f\lambda$, where λ is wavelength, the expression looks like this:

$$\lambda_{min} = 2\Delta x \tag{10}$$

Equation 10 indicates that the minimum wavelength detectable is equal to twice the receiver spacing. According to Socco and Strobbia (2004) will this limitation particularly affects the possibility of inferring information of the upper layers, but they also note that attenuation of high frequencies is a much more limiting factor for detection of the highest frequency.

The influence of the source offset

There are other issues to contemplate than array length, number of receivers and receiver spacing when doing seismic surveys. Near- and far-offset effects influences the ground roll and hence the dispersion image. Optimal recording of ground roll requires the Rayleigh wave to be planar. Due to geometrical spreading, Rayleigh waves can only be treated as planar horizontally traveling waves after traveling a certain distance (x_s) from the source point (Richart *et al.* 1970). Stokoe *et al.* (1994) suggests that the plane-wave propagation of surface waves does not occur in most cases until the distance from the source to the nearest receiver is greater than half of the maximum desirable wavelength λ_{max} (Eqn. 11)

$$x_s \geq \frac{1}{2}\lambda_{max} \tag{11}$$

If the offset is to close, undesirable near-field effects may occur as lack of linear coherency in phase at lower frequencies (Fig. 2.11 middle). Another important feature is the investigation depth. It is a normally accepted that the penetration depth for a Rayleigh wave is equal to the wavelength λ (Richard *et al.* 1970). The depth of maximum sensitivity, on the other hand is limited to about half of the maximum wavelength λ (Eqn. 12) (Rix and Leipski 1991).

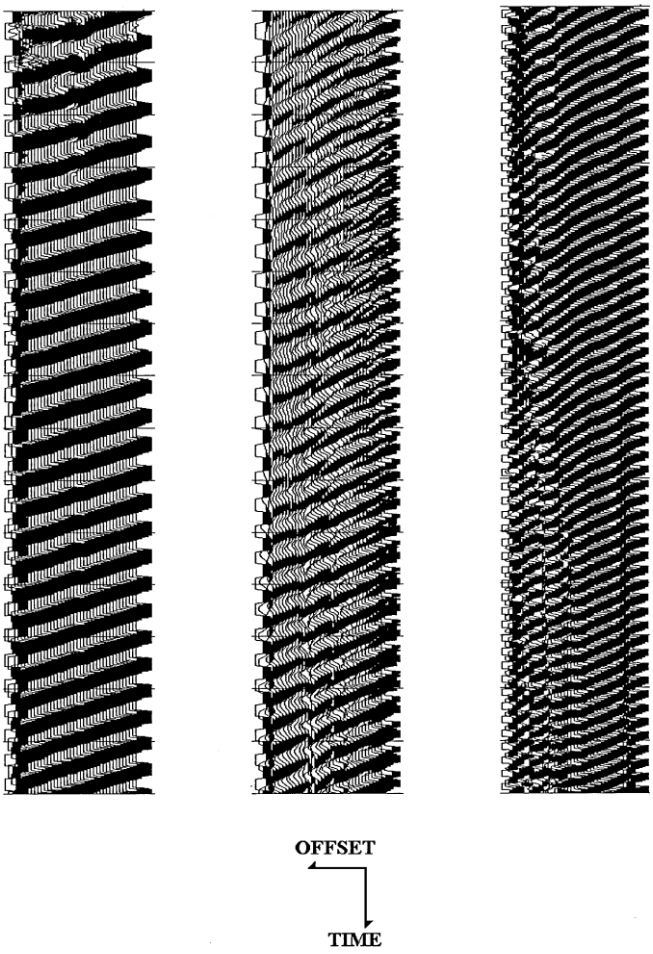

Figure 2.11 Rayleigh wave field data using a sweep source. Show differences in quality regarding near- and far-offset effects. The distance from the source to the nearest receiver is 27 m, 1.8 m and 89 m (from left to right). **Left:** Distance from source to nearest receiver is optimal. **Middle:** Near-field effects such as lack of linear coherency in phase are present. **Right:** Far-offset effect that is identified by decreased slopes in comparison to earlier arrivals. This will lead to a higher apparent velocity. After Park *et al.* (1999b).

$$z = \frac{1}{2}\lambda_{max} \tag{12}$$

By combining equations 11 and 12 it is a good rule of thumb that the offset from the source to the first receiver should be equal or greater than the desirable investigation depth (Eqn. 13) (Park *et al*. 1999b).

$$x_s \geq z \tag{13}$$

When it comes to far-offset effects it is with surface waves as with all acoustic energy traveling in the Earth. High frequency components attenuate more rapidly with distance away from the source than low frequencies (Bullen 1963). The S/N-ratio especially in the high frequency band will also decrease with larger offsets. Another possibility

might be that the high frequency components of the surface waves will not dominate higher frequency components of the spectrum due to contamination of body waves. According to Park *et al.* (1999b) this contamination of the surface waves result in a decrease of the ground roll slope (increased apparent phase velocity) (Fig. 2.11 right). Another effect might be reduction in the linear coherency of a specific frequency in the seismogram due to interference between low velocity ground roll and high velocity body waves.

These far-offset effects influence the highest frequency for which we can pick the phase velocity. Since the highest frequencies propagate in the uppermost layers, they define the minimum thickness of the shallowest layer. Stokoe *et al.* (1994) defines a relation between the phase velocity c_{min} for the highest frequency picked f_{max} and the thickness of the first layer h_1 (Eqn. 14)

$$h_1 \geq \frac{1}{2}\lambda_{min} = \frac{c_{min}}{2f_{max}} \qquad (14)$$

This equation can be used as a rough estimation for the minimum definable thickness of the shallowest layer.

Near- and far-offset effects are strongly dependent on the geological setting and the experimental conditions. Hence an optimal source-offset distance is difficult to determine.

If the test site is covered with cement or asphalt surfaces, there will in addition be coupling problems, limited amounts of vertical propagating body waves, and complex high-frequency trapped and guided waves (Miller *et al* 1999).

Velocity picking

Picking velocities is one of the most important steps in MASW. This is due to the fact that the velocity profile after the inversion is extremely sensitive to only small changes in the picked velocities. A well resolved dispersion image with good modal separation is necessary for correct picking, but the dispersion curve is limited to a certain frequency range, may interfere with other modes and/or can be discontinuous. Another phenomenon can be that the maximum energy is not always related to the fundamental mode. The maximum energy can in

some cases perform jumps to another mode for then to jump back to the original one. Higher modes can hold maximum energy for short frequency intervals, especially if there are high velocity layers in low velocity zones, hence energy related to modes are dependent on the geologic setting rather than the source spectrum and the seismic survey geometry.

The first and last velocity picks are the most critical ones for the velocity inversion and for the appearance of the final model. The highest frequency picked in a dispersion image defines the thickness and the velocity property of the uppermost layer. While the lowest frequency picked decides the depth of the model. Figure 2.12 shows the differences in the final velocity model when the first and last pick are included and excluded. Note the different scales for the two V_s profiles. The general pattern is that the velocity profile in the shallow and deep part has large differences while the models are similar in the middle. Figure 2.12 also clearly shows that the resolution of the dispersion image which allows for picking velocities at the lowest frequencies is crucial for the appearance of the final velocity profile.

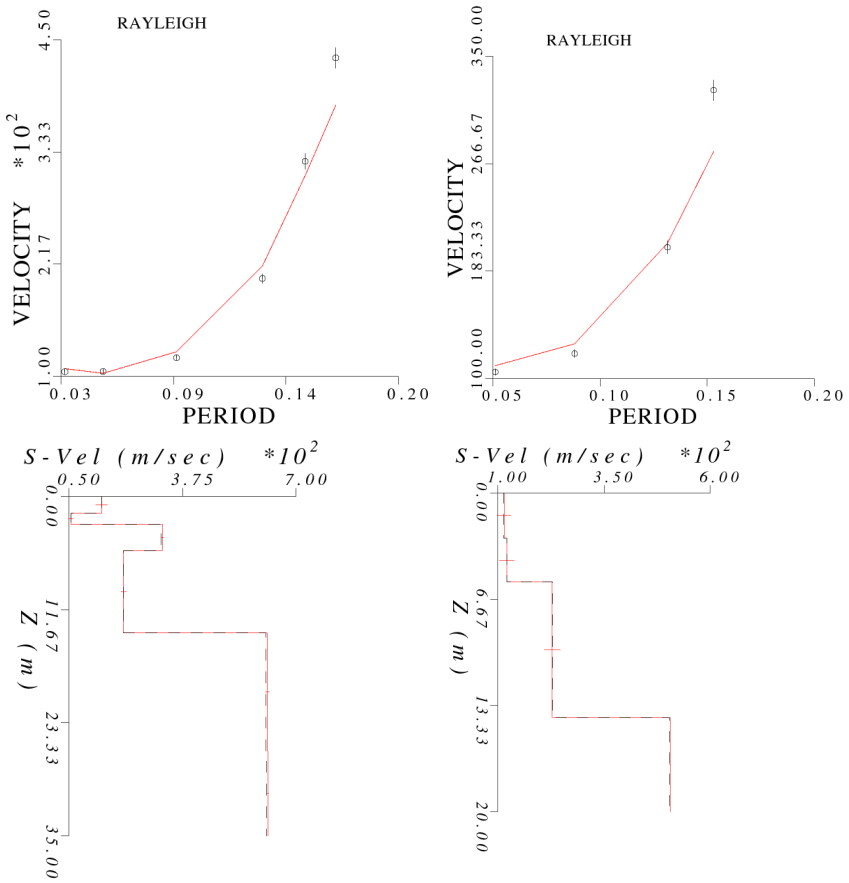

Figure 2.12 Differences in result of the final model when the first and the last pick are included and left out. The left model with all the picks inverted reaches greater depths and have a more complex velocity profile in the shallow layers than the inverted model with fewer picks (below right). But the interface between two layers at ca. 14 m depth is present in both models, but with a higher velocity in the deepest layer for the left model. These figures show that the first and last pick defines the velocity and thickness of the most shallow and deepest layer in the final model. Upper left and upper right figure show velocity picked (black marks) and calculated dispersion curve (red).

Influence of lateral inhomogeneities, dipping layers and a priori information

In surface wave velocity analysis it is assumed that the layers beneath the surface are flat and horizontally, imposed by the inverse problem required for the data interpretation. If there are topography variations and/or non-horizontal heterogeneities in the medium under the array of receivers, these assumptions break down and can drastically distort the dispersion image (Bodet *et al.* 2004a). At low frequencies the surface wave velocities are systematically underestimated. O'Neill (2003) concludes that even if the assumption of flat homogenous layers is acceptable, the surface wave dispersion measured in the field does not usually correlate with the theoretical dispersion. Another important feature to consider is that the dispersion data determined under a spread, describe an equivalent average flat medium (Bodet *et al.* 2004b), but that this assumption is not valid when dipping layers are present. If there is a two layer model with dipping interface (Fig. 2.13), the surface waves which are propagating on the up-slope side have a tendency to only investigate the first layer. This will result in a lower apparent velocity dispersion curve than the reference model, which after the inversion give lower velocities in both layers. On the other hand, surface waves propagating on the down-slope side will travel in both layers. This will result in a dispersion curve which has higher apparent phase velocities. If the dip increases, the error becomes larger and the spread length is even a more limiting factor (Bodet *et al.* 2004b).

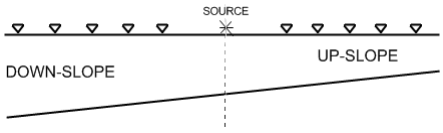

Figure 2.13 Shows the definition of the down-slope and up-slope case. The source is placed in the middle.

There have also been other experiments studying the effects of lateral heterogeneities and dipping layers and the effect this have on the dispersion image. For instance Bodet *et al.* (2004a) used laser-Doppler vibrometer measurements to provide controlled analogues of field acquisitions. By doing this in the laboratory, all the parameters were controllable and the uncertainties of the method could be well studied. Figure 2.14 displays the model used in the experiment. The model consisted of an aluminum box (ca. 20 x 20 x 30 cm) with a thinner layer of 3 mm plexiglas on top of it. This represented a 2-layer case with increasing density and seismic velocity with depth. The coupling layer has a thickness of ~1 mm. Occasionally air bubbles were caught between the plexiglas and the aluminum box. This was a good representation of heterogenic impurities. The source was a 6 mm in diameter piezoelectric transducer with dominant frequencies between 150 and 250 kHz. On the receiver side, a laser-Doppler vibrometer measured the absolute particle velocity on the surface via the Doppler

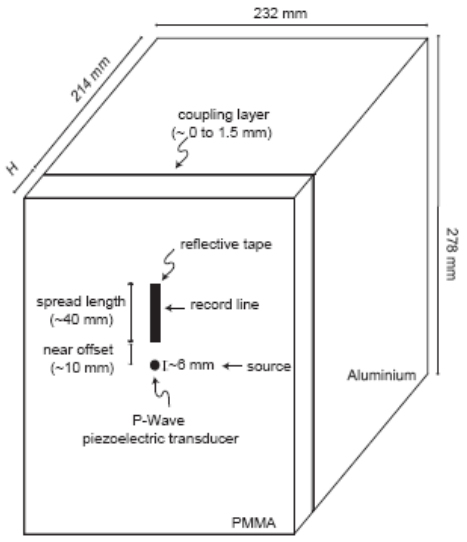

Figure 2.14 The model's basic geometry. A PMMA (plexiglas) plate represents the upper layer while the aluminum box represents the second layer half space. The source is a piezoelectric transducer. The record line is covered with tape for better reflectivity of the laser light which records the vibrations. After Bodet *et al.* (2004a).

shift (van Wijk 2003). This instrument sent out laser light to the plexiglas surface where it was reflected back. Once the surface started to vibrate, the frequency was shifted by the Doppler effect and the shifted laser light was recorded. Reflectivity tape was put on the plexiglas to improve the signal-to-noise ratio. The vibrometer scanned along a line to represent a real seismic array. This technique recorded typically 101 seismic traces with 0.4 mm spacing. The dominant wavelength of the Rayleigh waves was about 6 mm.

Two lines were recorded; one with irregular coupling layer between the plexiglas and the aluminum box and one with a clean interface. Figure 2.15 (middle) shows the dispersion images with the theoretical dispersion curves as white lines. Since the Rayleigh wave's main wavelength is almost twice the first layer thickness, it is possible to pick velocities in a great frequency range without being limited neither by the spread length nor by the frequency band of the source (Bodet *et al*. 2004a). Another important remark is that a higher mode almost overlaps the fundamental one for the line recorded with impurities in the coupling layer (Fig. 2.15 middle right). This clearly illustrates the high

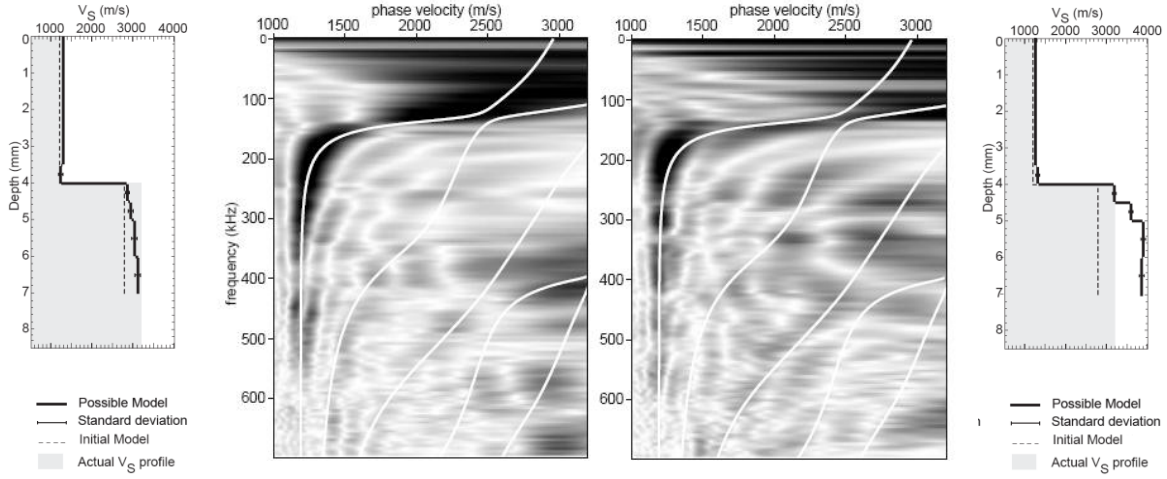

Figure 2.15 Displays the dispersion images and velocity profiles after inversion for a 3 mm thick plexiglas layer over aluminum. White lines in dispersion images represent calculated dispersion curves. Thick black line in the final velocity profile is final model, gray shaded area is actual velocity while dashed line is a priori information. **Left:** The case with a clean coupling layer between the plexiglas and the aluminum. **Right:** The case with heterogene impurities (air bubbles) in the coupling layer. After Bodet *et al.* (2004a).

uncertainty when picking velocities in the low frequency area.

Figure 2.15 (left) shows the inversion results for the experiment with a clean coupling layer (line 3). A priori information represented as a dashed line, was added to give a hint of the interface depth (in addition to empirical estimates of S-wave velocities and density). This dashed line can be looked at as an initial model. The interface appeared around 4 mm depth and with a velocity of 2.6 km/s. This is typical of the poor resolution of the method at low frequencies (Bodet *et al.* 2004a). This illustrates why the spread length parameter is of great importance when it comes to modal separation. Figure 2.15 (right) displays the dispersion image and the final velocity model for the line with irregular coupling. The presence of heterogeneities (air bubbles) reduced the dispersion image and hence the quality of the inversion process. The velocity in the aluminum half-space was overestimated.

In the final experiment by Bodet *et al.* (2004a), the interface between the plexiglas and the aluminum half space was dipping (1.37 degrees). Figure 2.16 (top) displays the schematic geometry. Two lines were recorded, one up-slope and one down-slope. Figure 2.16 (right) displays the dispersion image and the velocity model computed for the up-slope case. By looking at the dispersion image, it is hard to pick correct phase velocities at low frequencies.

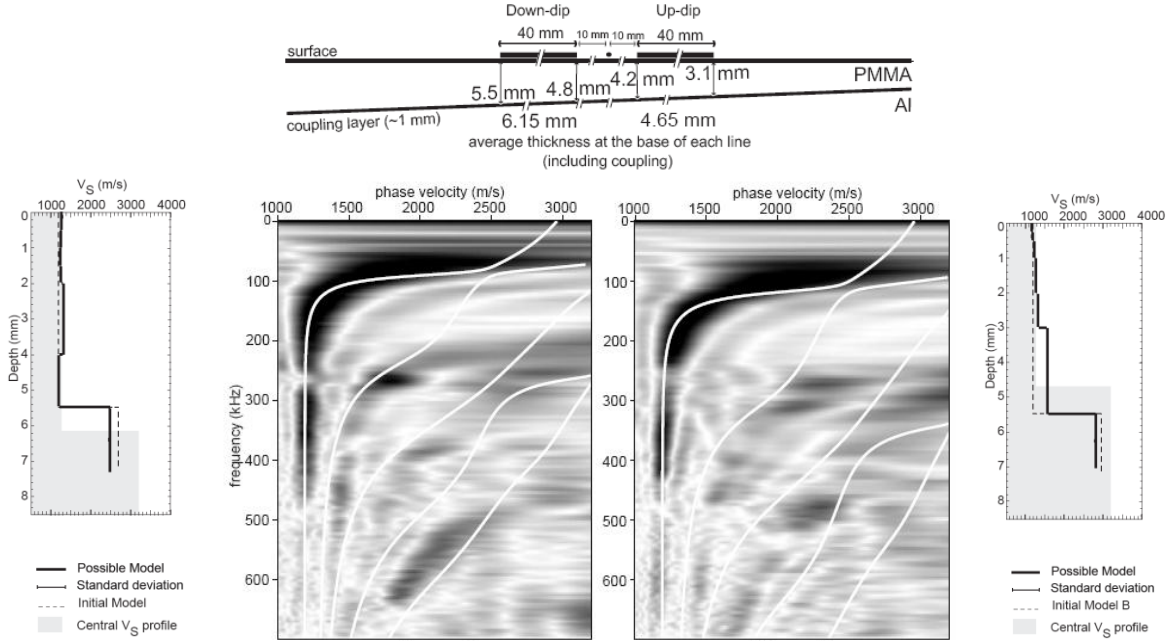

Figure 2.16 Top: Schematic geometry for the dipping layer model. **Below:** Dispersion images for the down- and the up-slope case. White lines represent theoretical dispersion curves. The final velocity model represents an average upper layer of 6.15 mm (down-slope) and 4.65 mm (up-slope) for the upper layer. Thick black line represents the final model, grey shaded area is actual velocity and dashed line is wrong a priori information After Bodet *et al.* (2004a).

The final model (thick black line) represents average velocity values for an equivalent flat layered model. Wrong a priori information (dashed line) regarding the interface depth and the second layer velocity was added to check the stability of the method. Neither the interface depth nor the correct aluminum velocity were obtained after the velocity inversion. Figure 2.16 (left) displays the dispersion image and the velocity model for the down-slope case. Again wrong a priori information regarding the interface depth and second layer velocity was added. For this case it was even a more significant mismatch between the real aluminum velocity and the velocity obtained in the final model and the correct depth of interface is not found. For both the up-slope and the down-slope case the final velocities for the second layers were underestimated, even though Bodet *et al.* (2004b) suggest that the velocities for the down-slope case usually are being overestimated.

These experiments by Bodet *et al.* (2004a) clearly show why a well resolved dispersion image is important when picking velocities, especially in the low frequency area. And that different models can result in identical dispersion images. Other important factors to remember when working with analysis of surface waves are that non horizontal layers and lateral heterogeneities will affect the dispersion image drastically; hence incorrect 1-D velocity profiles will be generated.

We have now taken a look at theory regarding surface wave dispersion and given an introduction to spectral analysis of surface waves included a velocity inversion technique. In the following chapter this method is applied to seismic data gathered in the Finneidfjord area the summer of 2007. Other geophysical data such as resistivity measurements and ground penetrating data will also be presented.

3. Finneidfjord summer campaign 2007

The last geophysical data collection in the Finneidfjord area took place in July 2007, when a group of people from the International Centre for Geohazards (ICG, Oslo), the University of Oslo (UiO), the University of Strasbourg (France), Vassar College (USA) and the Norwegian Geological Survey (NGU, Trondheim) did geophysical field studies to increase the knowledge about the area. Ground penetrating radar (GPR), resistivity measurements and

active/passive seismic are among the methods used. Figure 3.1 displays the geometry of the geophysical acquisitions with starting point 0 m for a reference profile at the western side of the investigation area. Ending point was at 380 m distance on the east side. 50 MHz GPR data and resistivity measurements were recorded along the whole profile. Two grids were investigated with both 250 MHz GPR and OhmMapper in addition to two GPR common mid-point (CMP) measurements. Three seismic lines represented with blue color were chosen with starting point at the distances 40 m, 120 m and 280 m.

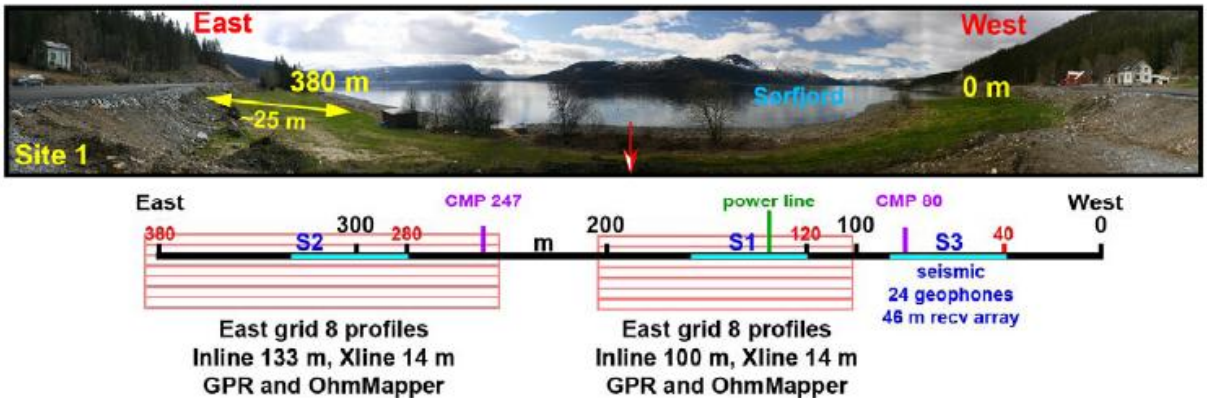

Figure 3.1 Reference profile with starting point 0 m at the western side of the location. Ending point is located at 380 m on the east side. Seismic lines are represented with blue color. The red grids mark location of area investigated with 250 MHz GPR and OhmMapper. Two locations for GPR CMP measurements are also displayed. After Lecomte *et al.* (2008).

I will summarize here the results obtained with GPR and resistivity, and present an analysis of the surface waves and a P-wave tomography.

3.1 Ground penetrating radar (GPR)

To get a first impression on how the subsurface looked like and what to expect from further geophysical investigations a GPR 50 MHz rough-terrain Ramac antenna was used along a reference line defined from 0 m (west) to 380 m (east) (Fig. 3.1). The 50 MHz rough-terrain antenna is easy to use for one person and gives fast and effective results. The data from this antenna are shown in figure 3.2. One can clearly point out two different elements (Fig. 3.2). The first one is the area on the eastern part of the profile from distance 340 m and out. In this section, the radio waves penetrate deeper and with less attenuation than in the rest of the profile even though no clear reflectors are visible. Interpretation has suggested it to be bedrock (gneiss) which outcrops to the surface further east (outside the profile). The second

event is a reflector forming a channel-like structure starting at distance 170 m and ending around 340 m. As with the eastern part of the profile, there is less attenuation of the radar waves above this reflector, while below there is zero visibility. It is also possible to track this reflector at shallower depths further to the western part of the profile. GPR methods are efficient in finding the watertable, but there are limitations. The ratio between the capillary zone (distance between dry and fully saturated medium) and the wavelength of the incident radio waves needs to be small in order for the radio waves to detect the changes in resistivity as an interface (Reynolds 1997), hence low frequencies radio waves have a better chance of detecting watertables than high frequencies radio waves.

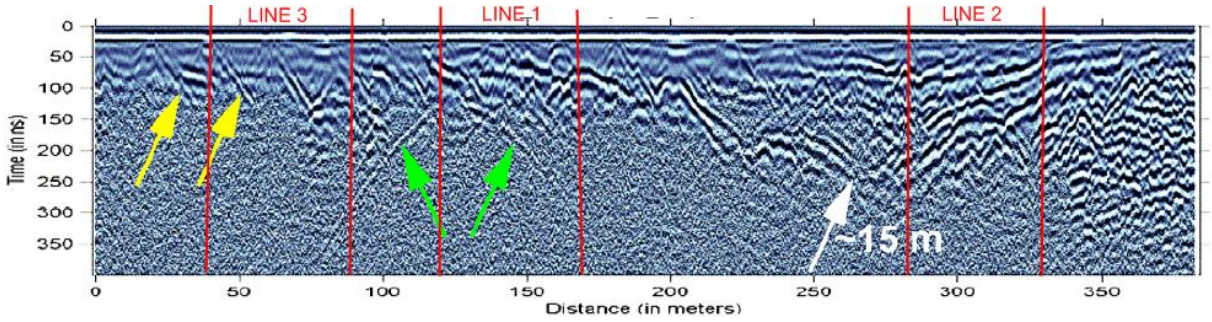

Figure 3.2 GPR data from a 50 MHz unshielded rough-terrain Ramac antenna. Yellow arrows indicate diffraction hyperbolas due to 50 cm wood sticks every 20 m used for coordinate reference. Green arrows indicate diffraction hyperbola as a result of a power line crossing the area. White arrow points at the lowest point of what seems to be a palaeochannel at ca. 15 m depth. After analyzing this GPR profile, it was decided that the three seismic lines were selected such that the different properties of the area were mapped. Line 1 with starting point at 120 m, line 2 at 280 m and line 3 at 40 m. Each line is 46 m long. Modified after Lecomte *et al.* (2008).

The CMP GPR data from distance 247 m on the reference line (Fig. 3.1) is displayed in figure 3.3. The 100 MHz data (Fig. 3.3 right) shows two possible reflectors indicated with red and white arrows, while the 50 MHz data (Fig. 3.3 left) penetrates deeper but the resolution is worse and only the deepest reflector is visible. After depth conversion, a 2-layered model is presented with interfaces at 1.7 m and 5.2 m. The velocities are 0.095 m/ns and 0.056 m/ns for layer 1 and 2 respectively. CMP data from distance 80 m on the reference profile (Fig. 3.1) has not been analysed at this point, but image from this location can be viewed in appendix B.4. Neither has the GPR data from the two grids.

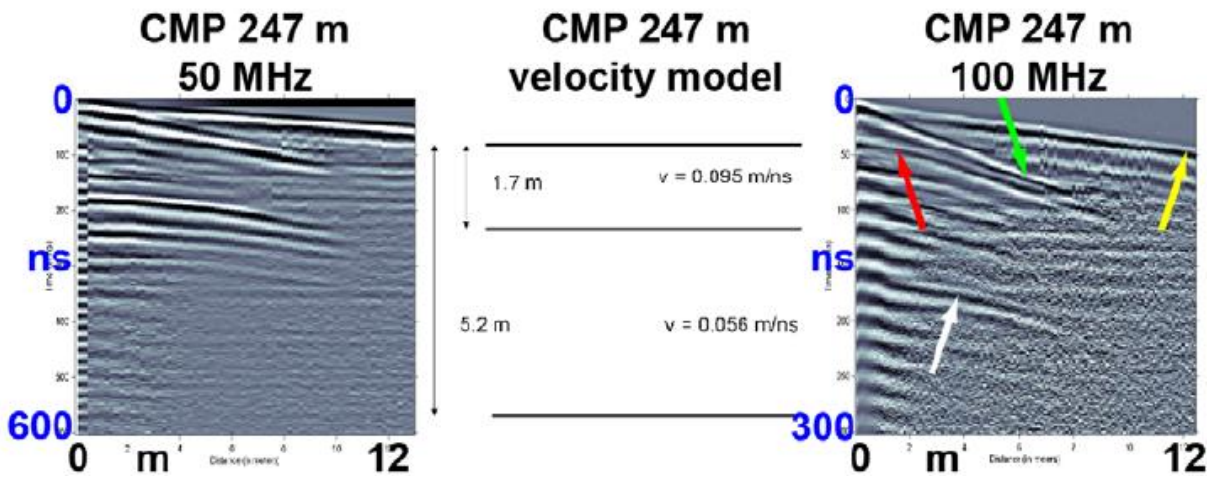

Figure 3.3 Right: 100 MHz GPR CMP investigation at 247 m on the reference line (Fig. 3.1). Yellow arrow indicates the air wave, green arrow the direct wave, red and white arrows 2 possible reflectors. **Left:** 50 MHz GPR CMP data at same location. Reflector marked with red arrow in the right figure is difficult to detect while the other possible reflector is visible at around 175 ns at 0 offset. **Middle:** Model after depth conversion of the two GPR CMP data. After Lecomte *et al.* (2008).

On the basis of the GPR information, three 46 m long seismic lines were planned in order to map out the different properties of the area.

In all three lines, single shots for calculating the dispersion images were used. After trial and error for determining the number of receivers used in the computation of the dispersion images and the source-nearest receiver distance, it was decided that the receiver distance window (RDW) was set to 20 m and the source-nearest receiver distance to 10 m. These distances are optimal when it comes to a compromise between dispersion image resolution and the amount of energy attenuated. A RDW of 20 m included 10 or 11 geophones. After the first dispersion image was calculated for the first RDW: 0-20 m, the RDW was moved 5 meters further into the receiver array. This time the dispersion image was calculated for 5-25 m, the next one for 10-30 m, and so on. The last RDW in each line is set to 30-46 m (9 geophones). Since the sources are not triggered with equal spacing for the different lines, the distance to the nearest receiver may vary from 8 – 15 m.

3.2 Surface wave data analysis

The equipment used in this seismic survey consisted of a 24-channel Geode Exploration Seismograph from Geometrics connected to a laptop for controlling the settings and easy

access of viewing the raw data. 4.5 Hz vertical component geophones, in the total number of 24, spaced 2 m apart were used in three different lines (Fig. 3.4). As source a seismic gun with shotgun rounds was first tested, but too low amplitude response on the seismogram lead to the decision of not to use it. As opposed to a 5 kg sledgehammer on a metal plate which resulted in good seismogram quality. The sampling rate was set to 4 kHz (0.25 ms).

Figure 3.4 An overview on the investigation area with the three seismic lines displayed. Line 1 in the middle, line 2 in the eastern part and line 3 in the western part of the area. Each seismic line is 46 m long. The main road in the area with local houses located north of the investigation area. Background photo from www.norgeibilder.no.

Figure 3.5 shows the frequency spectrums corresponding to different shots from different lines. Most of the energy is related to a frequency range from 5 Hz to around 60 Hz. But due to rapid attenuation of the high frequencies, the expected frequency range for picking velocities is expected to be smaller, maybe from 5 Hz to around 40 Hz for line 1 and line 3 (Fig. 3.5 left and right), and up to 50 Hz for line 2 (Fig. 3.5 middle).

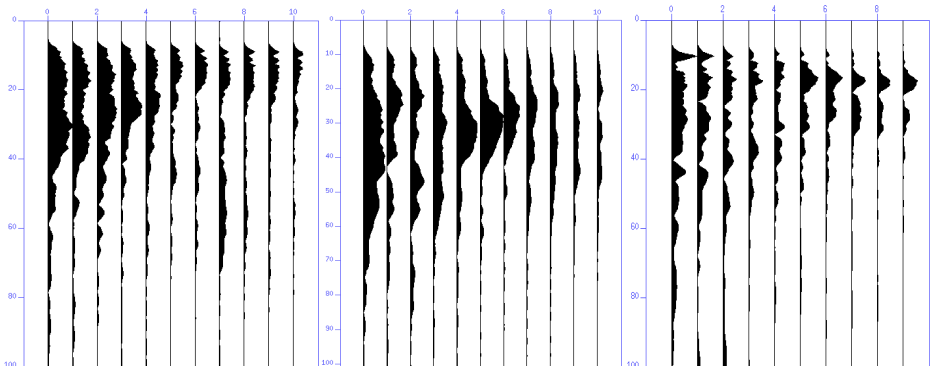

Figure 3.5 Frequency spectrums for each trace from 3 randomly chosen shots from line 1, 2 and 3 (left to right). Typical frequency range is 5-60 Hz. Higher frequencies are attenuated more rapidly with offset than lower ones.

Line 1

According to the 50 MHz GPR image (Fig. 3.2), line 1 holds the most flat lying layers with small lateral changes in velocity. Figure 3.6 shows the dispersion images for selected shots. From left to right the RDW is set to 0-16 m, 6-26 m, 16-36 m and 26-46 m with 0 value at distance 120 m on the reference line (Fig. 3.1). The dispersion images show small or no changes relative to each other. This reinforces the theory that the area is laterally homogenous and that the velocity contrast is horizontally stable with offset. Velocities were picked for the different shots and the 1-D velocity inversions were carried out.

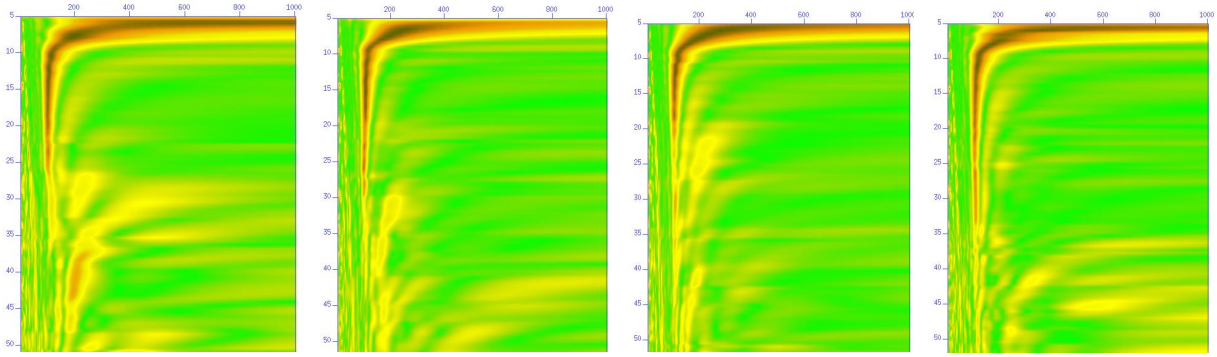

Figure 3.6 Dispersion images from different parts of the receiver array for line 1. The different images are almost identical which indicates that there are small lateral velocity variations. The RDW is sat to 16 m (9 geophones) in the figure to the far left, while the rest 20 m (11 geophones). From left to right the RDW is sat to: 0-16 m, 6-26 m, 16-36 m and 26-46 m, with 0 value at 120 m on the reference line (Fig. 3.1). Horizontal axis is velocity in m/s. Vertical axis is frequency in Hz.

Figure 3.7 displays the calculated dispersion curve and the inverted 1-D velocity profile for RDW: 6-26 m. One can observe that the curve follows a path which not looks optimal for the short periods. This will lead to the high velocity anomaly at 2.5 m depth. Further on all the different 1-D profiles were put next to each other and the velocities interpolated with the program Surfer 8. Figure 3.8 shows the 2-D shear-wave velocity profile from line 1. All the different 1-D velocity profiles with complete resolution coefficients can be viewed in appendix B.1. The layers are relatively flat and it may seem that the increasing velocity with depth is changing gradually from around 100 m/s in the uppermost part of the profile to 500 m/s at maximum depth (15 m). But comparing the 2-D profile with the different 1-D plots reveals a relatively large velocity contrast at around 7 m. Another thing to comment is the local high velocity anomaly at 16 m offset at ca. 2.5 m depth, the velocity here is around 300 m/s, while the surrounding material holds 150 m/s. This might be a result of a not so good

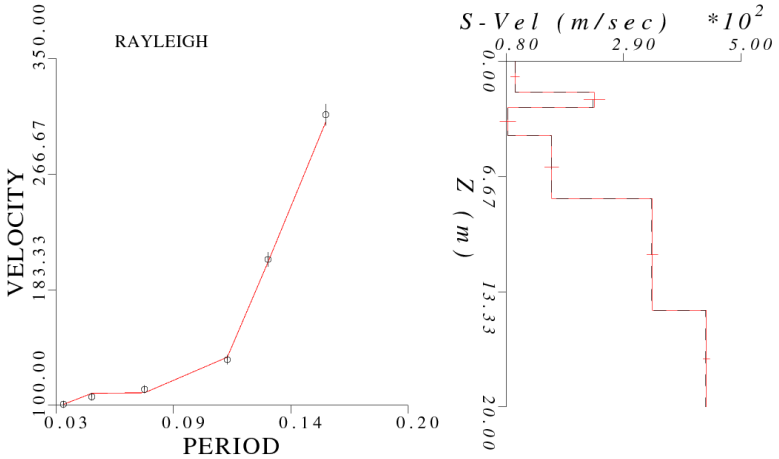

Figure 3.7 Displays the picked velocities, the calculated dispersion curve and the inverted velocity profile for a selected shot from line 1. RDW is set to 6-26 m. The calculated dispersion curve (left) does not look optimal for short periods; especially the calculated line between the second and the third velocity pick (from left). This will lead to the large velocity inversion in the 1-D velocity profile (right).

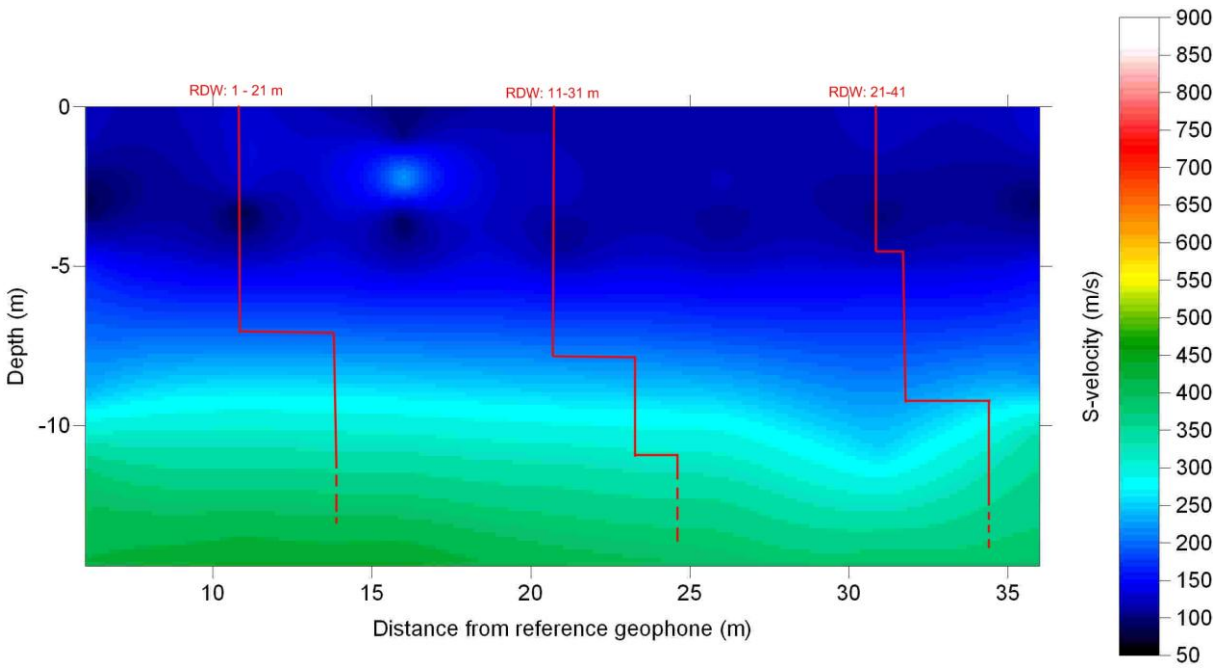

Figure 3.8 2-D shear-wave velocity profile from line 1. The figure displays relatively flat lying homogeneous layers. The velocity is apparently gradually increasing from around 100 m/s to 450 m/s. But comparing the profile with the different 1-D velocity profiles (simplified in this figure) reveals that there is a large velosity contrast at around 7 m throughout the unit. All the 1-D velocity profiles can be viewed in appendix B.1.

velocity inversion. The resolution coefficient for the upper layer in each 1-D inversion is always close to 1, while the value for the second layer is usually small, which can be related to the fact that the second layers often obtain lower velocities than the first ones. This is not visible on the 2-D plot, but easier to see on each 1-D profile. The rest of the resolution coefficients vary from 0.4 to 0.8.

Line 2

The 50 MHz GPR data, indicate that line 2 contains more lateral heterogeneities than line 1 (Fig. 3.2). Figure 3.9 displays the dispersion images from selected shots. From left to right the RDW is set to 0-20 m, 10-30 m, 20-40 m and 30-46 m with 0 value at the distance 280 m on the reference profile (Fig. 3.1). The different dispersion images indicate that the velocities with depth are changing laterally. The phase velocities at a given frequency are increasing as the RDW is moving from west to east (from left to right). Velocities were picked and the inversion process carried out. Figure 3.10 displays the calculated dispersion curve and the inverted 1-D velocity profile for a selected shot (RDW: 5-25 m). While 10 Hz holds a phase velocity of 120 m/s for line 1, the phase velocity varies from 300 m/s to 500 m/s for the same frequency for line 2. As with line 1, the velocity of the second layer in each 1-D inversion is slower than for the uppermost layer, but this time the resolution coefficient is relatively high

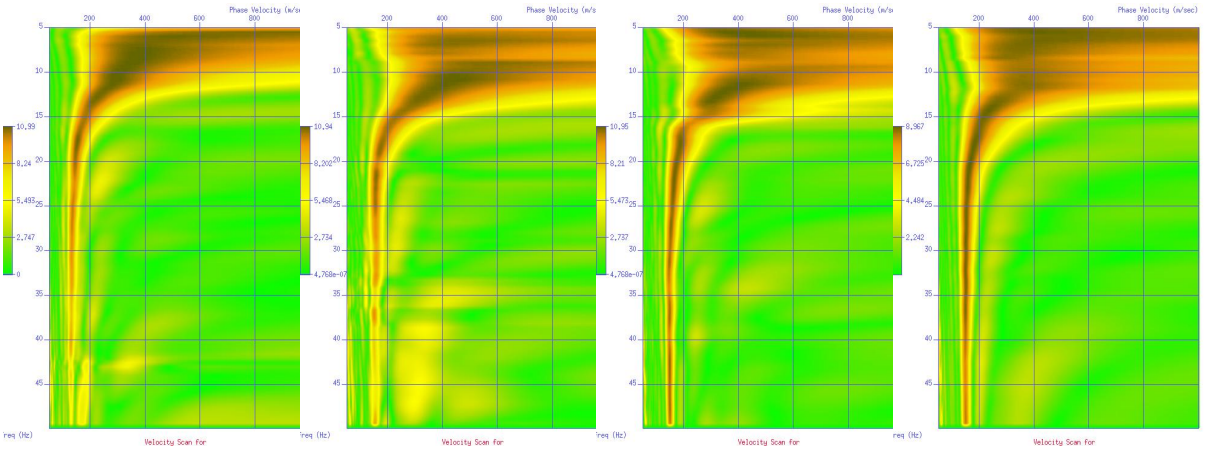

Figure 3.9 Dispersion curves for line 2 with RDW value 0 at 280 m on the reference line (Fig. 4.2). The different images are changing with different RDW's. The apparent phase velocities are increasing as the RDW are moving from west to east (from left to right). RDW values are set from left to right: 0-20 m, 10-30 m, 20-40 m and 30-46 m, which includes 11 geophones for the three first images and 9 for the last one.

for this layer. The resolution coefficients are also decreasing with depth, so that the values for layer 5 and 6 are often very small. A complete collection of the different 1-D velocity inversions with correlation coefficients can be found in appendix B.1. After the velocity inversion is completed, the 1-D velocity profiles were put beside each other and interpolated to obtain a 2-D velocity profile. The result is displayed in figure 3.11 and clearly suggests a structure which contains lateral velocity differences. The velocities are varying from about 100 m/s in the uppermost part of the profile to around 900 m/s at 20 m and below. The image is revealing a trend suggesting that layers are dipping west. This results in higher velocities at shallower depths in the eastern part of the profile.

The maximum depth of the final model is around 22 m which is deeper than for line 1. This is not because the dispersion diagram resolution is better for line 2 than for line 1, and allows lower frequencies to be picked. The reason for a greater maximum depth is due to that the phase velocity for a certain frequency is far greater for line 2 than for line 1.

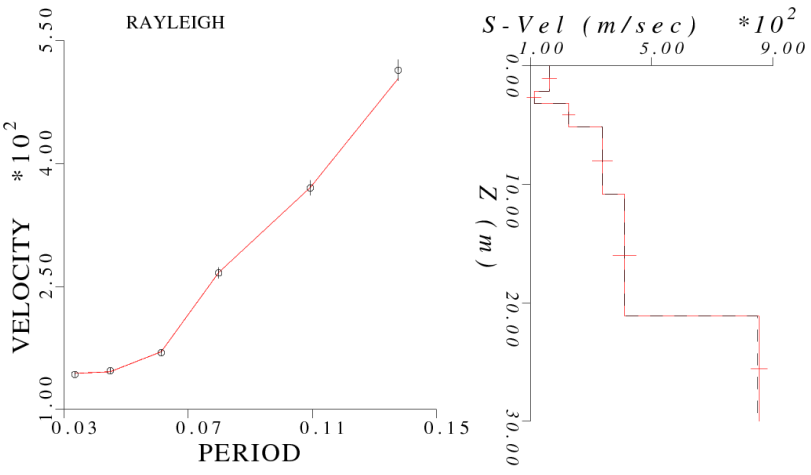

Figure 3.10 Displays the picked velocities and the calculated dispersion curve from a selected shot from line 2. RDW is set to 5-25 m. By comparison with figure 4.7 it is possible to observe that the velocities are generally higher for all periods. The period range is on the other hand quite equal. This indicates that the different maximum depths obtained for line 1 and line 2 is due to the higher velocities rather than the minimum frequency picked.

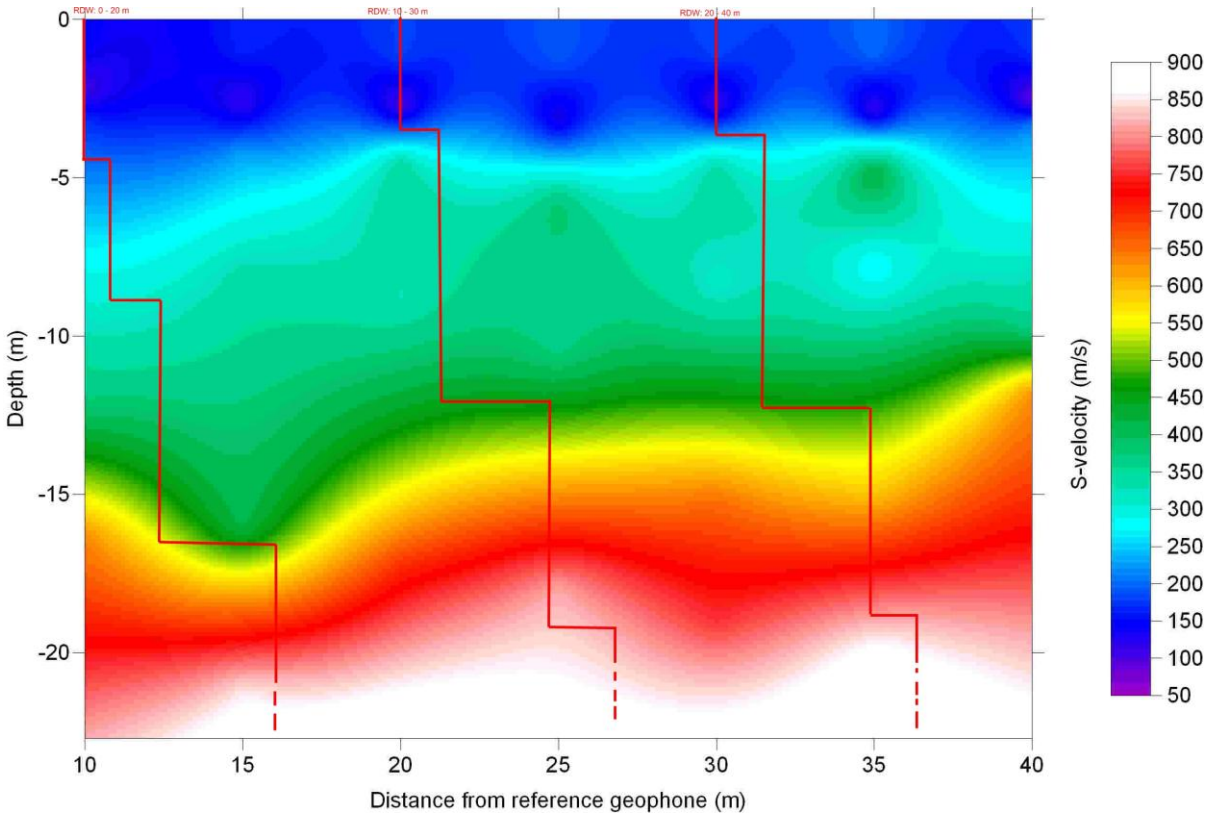

Figure 3.11 2-D shear-wave velocity profile from line 2. The figure displays a structure with lateral velocity differences. The general trend is that the high velocity zone (yellow and red) is at shallower depth in the eastern part of the profile (right) and dipping towards west (left). The most shallow part holds a velocity of around 100 m/s while the maximum velocity is located at 20 m and more (900 m/s). Three simplified 1-D velocity profiles are displayed as red lines (RDW from left to right: 0-20 m, 10-30 m and 20-40 m. A complete collection of the 1-D velocity profiles can be found in appendix B.1.

Line 3

It can be seen in figure 3.2 that the most shallow layers below line 3 are more or less horizontal, and one could expect similar simple dispersion images as in line 1. This is not the case. Figure 3.12 displays selected dispersion images from line 3. The RDW is set from left to right: 0-20 m, 10-30 m, 20-40 m and 30-46 m, with 0 value at 40 m on the reference profile (Fig. 3.1). The dispersion images are totally different from those for the two other lines. It is difficult to track and follow the fundamental mode in all dispersion images except one (Appendix B.1, Line 3, RDW: 5-25 m). In addition the dispersion curves are discontinuous. Another phenomenon is that the maximum energy seems to jump on to another mode for then to come back to the original one (Fig. 3.12 far left). In other images it looks as if there are several fundamental modes and that one mode is in the shadow of the other (Fig. 3.12 number three from left). Picking velocities for inversion was a difficult task and the results contain large uncertainties. Figure 3.13 displays the calculated dispersion curve and the 1-D velocity profile for this shot. It is possible to observe that the calculated dispersion curve almost

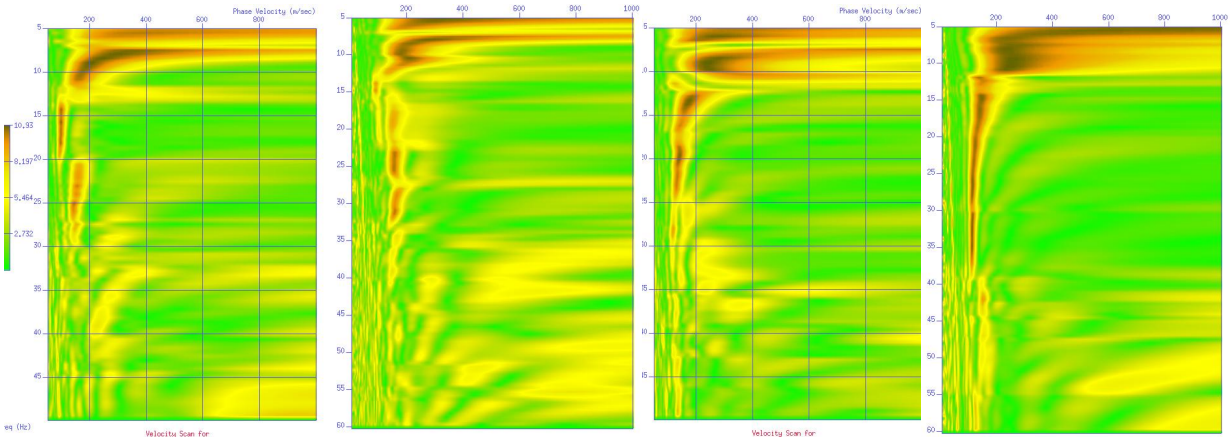

Figure 3.12 Dispersion curves for line 3, with RDW = 0 at 40 m on the reference line (Fig. 3.1). These dispersion images are characterized by discontinuous modal curves, maximum energy jumps from one mode to another and then back (far left) and the appearance of "several" fundamental modes (nr. 2 and 3 from left). Large uncertainties are related to the velocity picking. RDW are set to (from left to right): 0-20 m, 10-30 m, 20-40 m and 30-46 m, which includes 11 geophones for the three first images and 9 for the last one.

follows a straight line. The different 1-D velocity profiles were put beside each other and interpolated. Figure 3.14 displays the 2-D velocity plot after inversion and interpolation of the 1-D plots. The velocity distribution is almost identical to the one for line 1, with the velocity increasing from around 100 m/s at the most shallow layer to around 500 m/s at 15 m depth, but one large difference stands out. In the middle of the figure from 15 m to 35 m from the reference geophone, a high velocity anomaly is indicated. In this part the velocity reaches 550 m/s to 650 m/s. The correlation coefficients for the different layers for line 3 are generally lower than the ones for line 1 and 2. This might be in connection with the large uncertainties when picking velocities. By studying the picks from one dispersion image to the other (Appendix B.1), one can notice that there is no clear trend. The picks do not follow any smooth curve but look noisier.

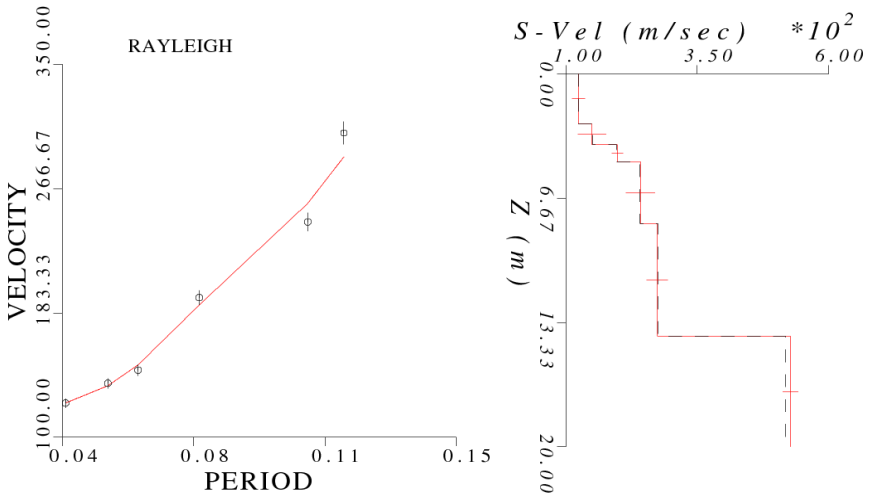

Figure 3.13 Displays the picked velocities, the calculated dispersion curve and the 1-D velocity profile for a selected shot from line 3. RDW is set to 20-40 m. The corresponding dispersion image can be viewed in figure 4.12 (nr. 3 from the left). It is possible to observe that the calculated dispersion curve follows a straight line more than a curve.

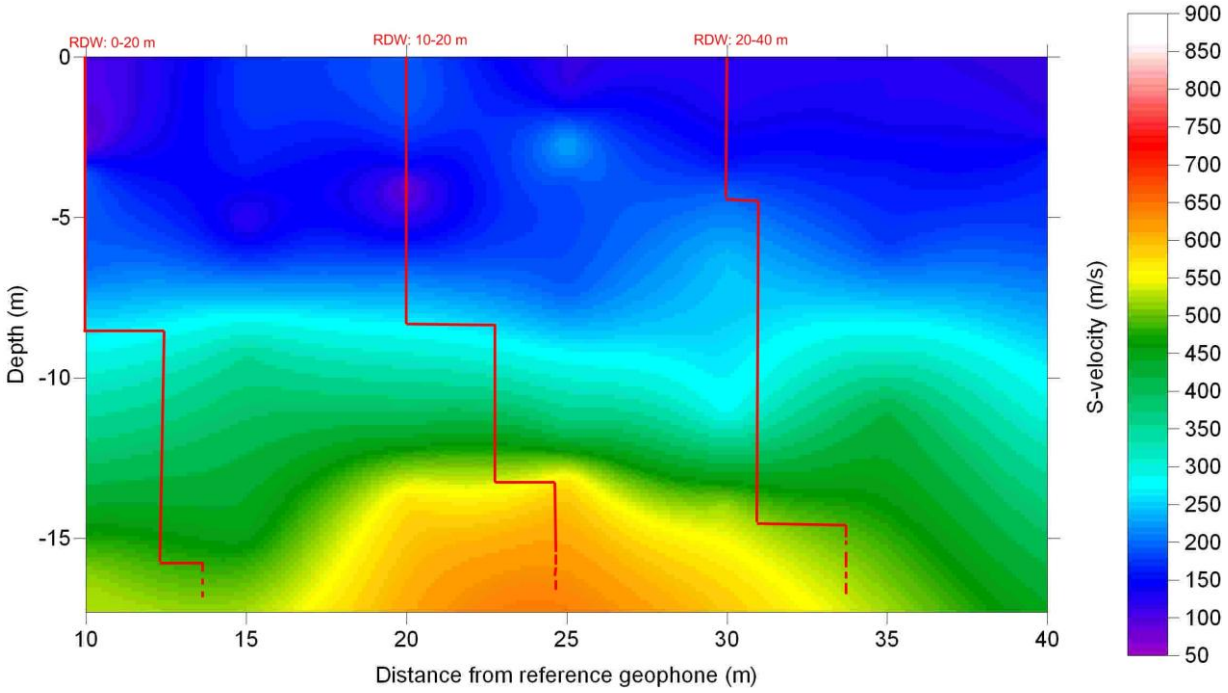

Figure 3.14 2-D shear-wave velocity profile from line 3.The figure displays relative flat lying velocity characteristics in the upper part of the profile with velocities ranging from 100 m/s up to 450 m/s. A high velocity zone can be viewed at ca. 15 m depth in the middle part of the profile (15-35 m from the reference geophone), where velocity exceeds 600 m/s. Three 1-D velocity profiles are displayed as red lines (RDW from left to right: 0-20 m, 10-30 m and 20-40 m). A complete collection of the 1-D velocity profiles can be vied in appendix B.1.

3.3 P-wave tomography by Java Tomography Software (JaTS)

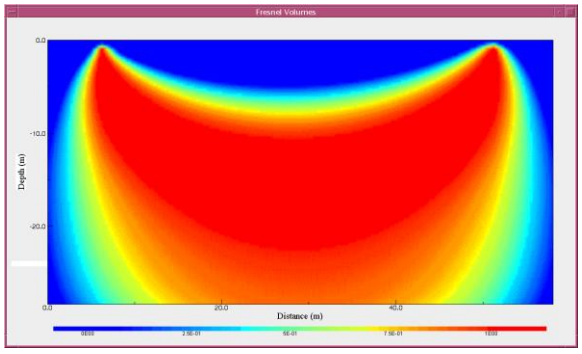

Figure 3.15 Display the principle of the JaTS tomography program. The Fresnel wave path between a specific source and receiver are utilized to calculate the travel time, based on the SIRT method. When this is carried out for several sources and receivers, lateral velocity anomalies can be detected.

To utilize the seismic data optimally a P-wave tomography was carried out. The program analyse the first arrivals in the seismogram and utilizes the Fresnel wave paths as kernel to obtain a 2-D P-wave velocity profile (Grandjean and Sage 2004) (Fig. 3.15). The algorithm is based on the simultaneous iterative reconstruction technique (SIRT), which analyses only one data at the time. For example wave paths and corresponding travel times between one source and receiver nr. 2, nr. 3 and nr. 4 separately. This reduces the amount of data processed simultaneously by the computer dramatically. All the shots in the seismic survey are used, both outside and inside the receiver array. An initial model is defined at the beginning and

after n numbers of iterations a final model is obtained. The brightness of the color represents the degree of resolution. The different initial models were set after considering the 50 MHz GPR data. This data provided information that suggested that the layers in the initial model for line 1 and 3 should be flat lying, while layers in line 2 should be slightly dipping towards west. All data from the P-wave tomography can be viewed in appendix B.2.

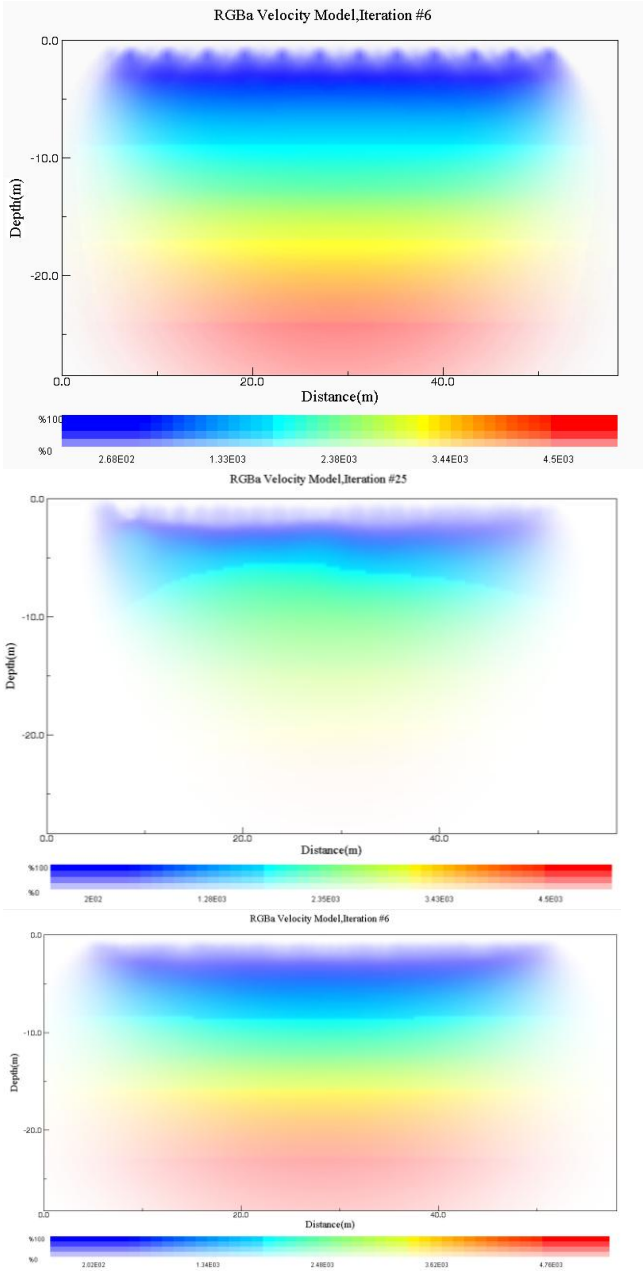

Figure 3.16 P-wave velocity profile for line 1,2 and 3 (from top to bottom) by using JaTS. Line 1 and line 3 display flat lying layers while line 2 contains laterally velocity heterogeneities. The resolution for line 1 and 3 is significantly better than for line 2. Velocities range from 200 m/s to around 4800 m/s. Zero on the x-axis corresponds to a distance 40 m, 120 m and 280 m on the reference profile (Fig. 3.1) for line 1, 2 and 3 respectively.

Figure 3.16 displays the final P-wave velocities for line 1, line 2 and line 3 (from top to bottom). As expected the final model for line 1 displays flat lying layers with gradual increasing P-wave velocities from around 270 m/s in the most shallow layers to 4500 m/s at ca. 24 m depth (Fig 3.16 top). Line 3 is almost identical with 200 m/s in the shallow part of the profile, increasing to 4760 m/s at 23 m depth (Fig. 3.16 bottom). 6 iterations were needed to obtain the final results. The resolution is fairly good down to approximately 27 m for both lines. One can also observe that the resolution is poorer towards the flanks due to that this area is not exposed to that many Fresnel wave paths. Line 2 contains as expected the least laterally homogeneous structure of the three lines (Fig. 3.16 middle). The most shallow part holds the same velocity as line 1 and 3 (around 200 m/s), but the area below 6 m is characterized by a doming like velocity structure with the top point at a distance of 22 m and decreasing towards the flanks. The resolution with depth is quite poor with good visibility only down to around 10 m

Now that both V_p and V_s data are calculated, it is interesting to see how they are linked together by computing either Poisson's ratio (σ) by equation 15 or simply looking at the V_p/V_s – ratio with depth.

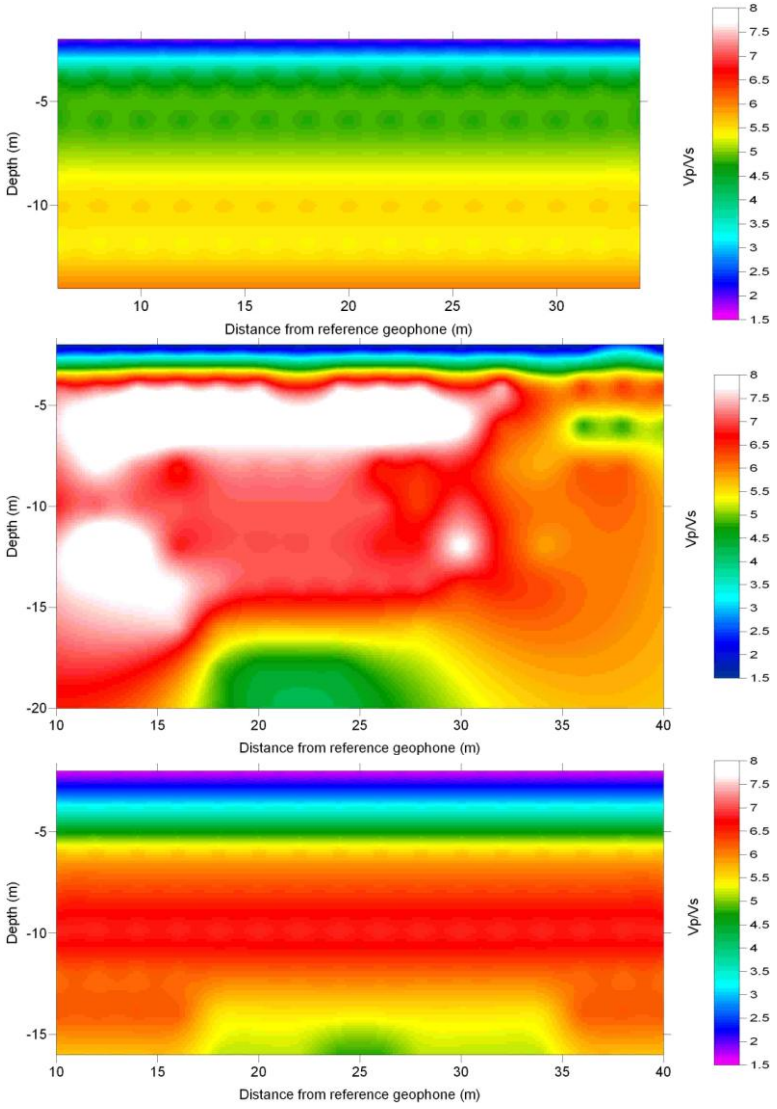

Figure 3.17 The V_p/V_s – ratio with depth calculated for the seismic lines 1, 2 and 3 (from top to bottom) on the reference profile (Fig. 3.1). P- and S-wave velocities are picked manually from the respectively 2-D profiles at every 2 m offset and at every 2 m depth. A clear boundary is located at a depth around 2-2.5 m where the ratios increase from around 3.2 to 4.5 and further. This is due to a more rapidly increasing in the V_p relative to the V_s. Line 1 and 3 hold values that are changing less laterally than line 2. This is due to the more lateral velocity variations for line 2.

$$\sigma = \frac{0.5\left(\frac{V_p}{V_s}\right)^2 - 1}{\left(\frac{V_p}{V_s}\right)^2 - 1} \qquad (15)$$

P- and S-wave velocities were picked manually from the respective 2-D profiles every 2 m offset and at every 2 m depth. Poisson's ratio with depth was calculated for line 1, 2 and 3, but the results were not very discriminated due to high V_p/V_s - ratios. The value of σ increased rapidly from 0 towards 0.5 at 2.5-4 m depth. Since it shows much more variation with depth, we prefer to show the V_p/V_s – ratio. Figure 3.17 display the V_p/V_s – ratio for line 1, 2 and 3 (from top to bottom). In all three images a clear boundary is visible at around 2 m (more abrupt for line 1 than for line 2 and 3), where the ratios increase from around 3.2 to 4.5 and further. This is due to the fact that the V_p is increasing more rapidly than the V_s at this depth. At greater depths the ratios are more stable, except than for line 2 where the most laterally velocity heterogeneities are present, hence a more varying V_p/V_s - ratio. The maximum ratios for line 2 and line 3 are significantly higher than the

maximum ratio for line 1 (ratio value of 8 and 7 for line 2 and line 3, while only 5.5 for line 1).

3.4 Resistivity measurements

The final geophysical measurements of the 2007 Finneidfjord summer campaign were resistivity measurements. Two different systems were tested. First an electrode-based system (ABEM Terrameter SAS 4000, Lund system, with electrode selector ES 10-64), then secondly a capacitive-coupled system (Geometrics OhmMapper). The electrode-based system was tested along two 600 m long profiles. One overlapping the reference line (Fig. 3.1), the other parallel to the first one, but further north (~20 m). The OhmMapper was used on the extended reference line and on the two grids displayed in figure 3.1. The OhmMapper data will not be presented in this assignment, but can be viewed in the appendix B.3 where a complete record of the resistivity measurements can be found.

Figure 3.18 (top) shows the 600 m resistivity profile from the extended reference line, using the electrode-based system with gradient configuration. A thin package with resistivity

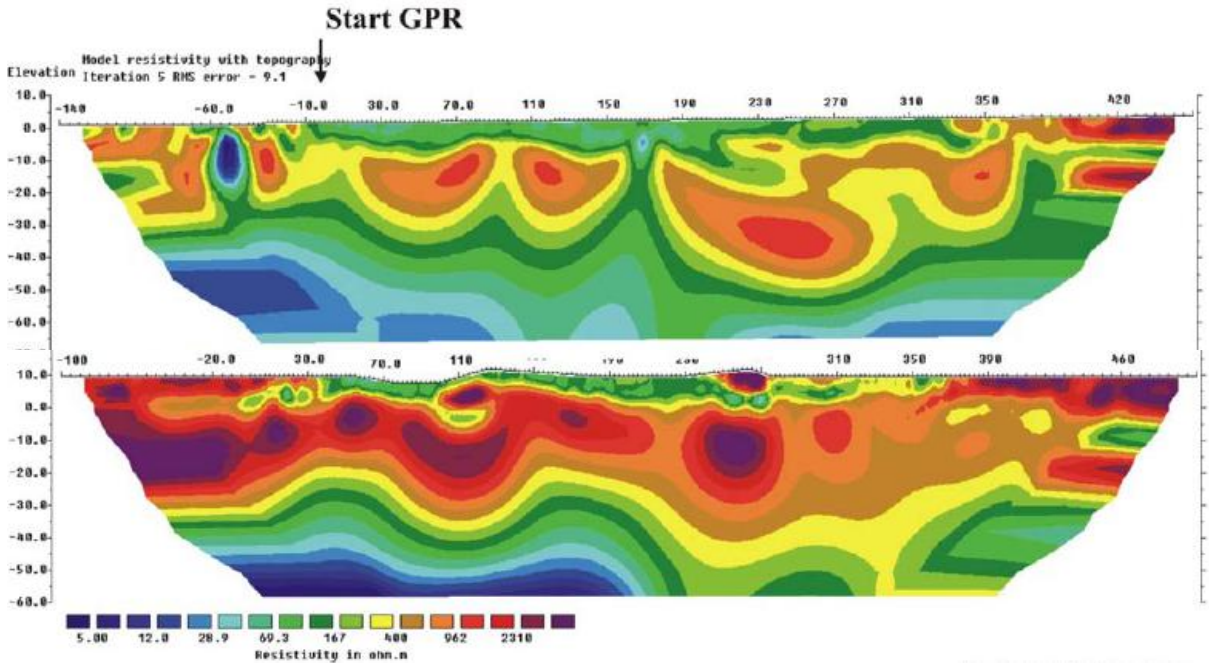

Figure 3.18 Top: Resistivity profile using an electrode-based system with gradient configuration. The line is an extension of the reference line in figure 3.1. Higher resistivity is located on the flanks, while a thin package of lower resistivity (50-100 Ohmm) is present in the middle part of the profile at shallow depths. This package is also visible in the profile below which runs parallel to the first one but ~20 m further north, here the resistivity values are generally higher. After Lecomte *et al.* (2008).

between 50 – 100 Ohmm is visible at shallow depths within the area of -10 m to 330 m on the reference line. Another characteristic feature is the very high resistivity in the easternmost area. The western flank also show signs of high resistivity. Figure 3.18 (bottom) displays the resistivity profile parallel to the extended reference profile, but ~20 m further north. The first feature to notice is that the resistivity values are generally higher in this area, while the general pattern with higher resistivity on the flanks for shallow depths is the same. The thin package with low resistivity is also present, but it is even thinner than the one from the line further south.

4. Discussion

4.1 Dispersion image quality

The most disappointing point related to the work with surface wave analysis is the problems of manage the 2M-SASW program to run optimally. The dispersion images for line 1 holds quite good resolution, but the quality of the dispersion images for line 2 and indeed line 3 would probably have been better if the summation principle of the dispersion images had worked properly. Instead only one shot was used and the quality is accordingly.

According to Stokoe *et al.* (1994) and equation 11, with the average source to nearest receiver distance of X_s = 10 m, the maximum pickable wave length should not exceed 20 m to avoid near field effects. This approximation seems to fit the resolution of the data. Frequencies and corresponding phase velocities which gives a wave length larger than this, almost always appear with very high uncertainties. In my velocity picking I have always crossed both these limits; hence layers and velocities at the deepest part of the V_s-profiles hold large uncertainties. This also comes through by the resolution coefficients (decreasing value with the depth of the layers), and by the criteria by Rix and Leipski (1991) (Eqn. 12) when the maximum investigation depth with reliable results is only 10 m. This is of course in accordance with Park *et al.* (1999b) that combined these two criteria (Eqn. 13). Larger X_s distances were tried out in hope of better modal separation and higher resolution in the low frequency area, but attenuation in the whole frequency specter made this impossible.

The inversion procedure presents a result that almost always contains a velocity inversion in the second and/or the third layer (Appendix B.1). This is the case for all three lines. By taking a second look at the calculated dispersion curve for the respective shots, it can be observed that even with a smooth velocity picking and a relatively smooth calculated dispersion curve, the result holds a velocity inverted layer (Fig. 4.1). This effect can be the result of an incorrect set program parameter.

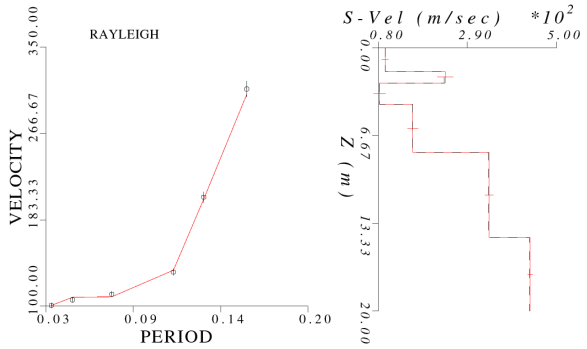

Figure 4.1 An example after the shear-wave velocity inversion. A velocity inversion is visible in the third layer even though the velocities picked and the calculated dispersion curve represents a gradually increasing velocity. Figure taken from line 1, RDW 6-26, appendix B.1.

The interpretation of the 2-D V_s-profile should be carried out with the consideration that this image is created by an average of the V_s within a RDW. That is when looking at the e.g. 2-D V_s-profile of line 2 (Fig. 3.11) at 20 m distance from the reference receiver, the velocities that are displayed are average velocities of the RDW: 10-30 m. Within 20 m the geological structure beneath the surface can change a lot and the main assumption of flat lying, horizontal layers may be invalid. With an optimal use of the 2M-SASW (Grandjean and Bitri 2006) a much smaller RDW could be utilized, hence better lateral resolution of the model. Another remark is the color scaling of the 2-D profiles. At the first appearance it may look like there is an abrupt interface between two layers at the yellow boundary in figure 3.11, but a closer look at the color scale reveals that the yellow part of the scale only represents a small velocity range. Therefore it is important to study the 1-D V_s-profiles separately to locate abrupt changes in velocity. By comparing selected 1-D V_s-profiles with the 2-D plot (Fig. 3.11) it is possible to observe that there is not an abrupt interface at the yellow color, but around 1 m further up in the dark green area (for 2 of the 3 1-D profiles).

The dispersion images from line 1 display good resolution for both high and low frequencies, and the shape of the fundamental mode does not change with the different RDWs. Frequencies can be picked in a range from around 7.5 Hz up to 35 Hz. The area holds small or no lateral velocity changes.

For line 2 the dispersion images are not that well focused for low frequencies, but velocities can be picked down to about 10 Hz. If the 50 MHz GPR data (Fig. 3.2) provides a priori information which suggests that there are dipping layers (towards west), then the dispersion images from this area should display lower apparent phase velocities than the real ones (Bodet *et al.* 2004b). This is because the source is placed such that the waves are traveling in an up-slope direction (Fig. 2.13). This may build up under the fact that the deepest areas of the 2-D V_s-profile for line 2 (Fig. 3.11) should contain higher velocities. There is no upper frequency limit for picking velocities for line 2. But from an interpretation point of view, frequencies higher than ~35 Hz will only display too thin upper layers. Another point is that the velocity is constant above a certain frequency (~20 Hz for line 2). It should be expected that the depth of investigation would be larger for line 1 than for line 2, due to lower minimum frequency picked. But the velocities corresponding to line 2 are higher and this results in an investigation depth of 25-30 m in comparison with 20 m for line 1.

The dispersion images from line 3 are poorly resolved with not so good modal separation. According to Socco and Strobbia (2004), higher modes can be dominant at normally dispersive sites. Figure 3.12 (far left) may show this phenomenon. The maximum energy is performing a jump onto a second mode for later to jump back to the original one. The rest of the dispersion images are also dominated by discontinuity and the difficulty of tracking the fundamental mode. Figure 4.2 displays the same dispersion image as in figure 3.12 (far left) only difference is that an interpretation of the different modes is added. The lowest available velocity is associated with the fundamental mode (Socco and Strobbia 2004). If this statement is valid, then in figure 4.2 the fundamental mode is represented by the red line, while the black line represents an overtone. If the black line is mistaken as the fundamental mode, then the velocity will be overestimated. And further at lower frequencies, what is the fundamental mode and overtone? It may be possible that the fundamental mode is shadowed by a high energetic overtone. Evidence for this might be that there is

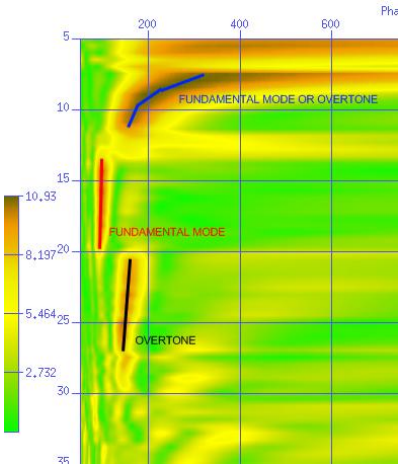

Figure 4.2 Displays a dispersion image with the problems related to discontinuity of energy maxima corresponding to fundamental mode and overtones. Black line represents energy maximum for an overtone. Red line represents energy maximum for the fundamental mode while blue line is energy maximum for either one of the modes. Example taken from line 3, RDW: 0-20 m, appendix B.1.

some high energy at very low frequencies which seems to disappear behind the maximum energy at higher frequencies. A better resolved dispersion image might have answered these questions. I chose to follow the red and blue line when picking velocities.

4.2 Geological setting

The 50 MHz GPR rough-terrain equipment is indeed a helpful tool to get hold of a fast overview of the geologic setting in the area. It provides useful information for planning further geophysical investigations and where to apply them.

What is interesting comparing the different dispersion images from line 1, 2 and 3 is that they all have their own characteristics. This indicates that the geologic setting is probably changing quite a lot from line to line, even though the lines are not far from each other. Line 1 provides the best dispersion images with a well focused fundamental mode for both low and high frequencies. The fact that the dispersion images do not change when moving the RDW through the receiver array indicate that the area below the receiver consists of flat lying layers with no velocity changes with offset. The P-wave tomography and the 50 MHz GPR data also support this. There are evidences that there is a lithological interface at around 6 m – 7 m depth below line 1. The 50 MHz GPR data display a possible reflector at this depth; in addition the visibility is decreasing below. All the different 1-D V_s-profiles display a velocity contrast with typical V_s of 150 m/s in the uppermost layer and 400 m/s below 6 m – 7 m. The P-wave tomography does not indicate an abrupt interface, but the velocity is increasing from around 270 m/s at the surface to around 1800 m/s below this depth. The uppermost material visible in the Finneidfjord area consisted of loose, unconsolidating moraine material most likely left behind after the last ice age (10000 years ago). The seismic velocities, 270 m/s for the P-wave and 100 m/s for the S-wave, fit with that material (Reynolds 1997, Kearey *et al.* 2005). Figure 3.18 (top) displays a resistivity value of ~70 Ohmm, which is acceptable for Quaternary deposits or clays (Reynolds 1997). On the contrary the seismic velocities are too slow to be related with clays (V_p = 1000-2500 m/s, Reynolds 1997, Kearey *et al.* 2005). The layer below does not allow penetration of 50 MHz radar waves, which is typical for water saturated materials and marine clays with high conductivity. On the contrary the material at this depth holds resistivity values from 170 Ohmm – 400 Ohmm which are too high to be clay (1-100 Ohmm) (Reynolds 1997). A possible explanation for why the GPR resolution is poor below 7 m might be that there are layers of clay present, but too thin to be detected by

seismic. The OhmMapper image from the same area (Appendix B.3) holds quite different values than the electrode-based system. Here larger values are present at depths as shallow as 2 m.

For line 2 the higher velocities in the dispersion images from west to east is an indicator that a fast velocity layer is moving towards the surface. From the 50 MHz GPR data (Fig. 3.2) and the 2-D V_s-profile (Fig. 3.11) the channel-like structure at ~15 m depth might be interpreted as an old erosional surface and/or a channel system related to transgression and regression for the last period with ice in the area. P-wave tomography does not display this structure. Instead a dome-like shape is visible at 7 m depth (Fig. 3.16 middle). It must be taken into consideration that the resolution is quite poor. The resistivity values below line 2, display generally higher values at shallower depths than for line 1, and at the eastern flank (right) the values are around 400 Ohmm even at the surface. This might be related with the higher seismic velocity in this area.

Line 3 is the most difficult part of the area to interpret, due to low resolution in the 50 MHz GPR data and the shear-wave dispersion images. Why is the attenuation of the radar waves in this area much larger than in the subsurface beneath line 1 and 2? Water saturated rocks and clay attenuate electromagnetic waves rapidly, but the resistivity values for this area do not differ from the values from line 1. As with line 1, there might be the possibility of the presence of clay layers or clay lenses, but too thin or too small so that neither the resistivity - nor the seismic measurements detect them.

A closer look at the GPR CMP interpretation in figure 3.3 reveals that the electromagnetic-wave (em-wave) velocities for the 2-layer model (0.095 m/ns for the first 1.7 m and 0.056 m/ns for the next layer) fit with em-wave velocities for unsaturated/saturated sediments based on work by van Heteren *et al.* (1998), Davis and Annan (1989), Theimer *et al.* (1994) and van Overmeeren (1994). According to their work em-wave velocities for unsaturated sand and gravel, clay or till hold values ranging from 0.9 up to 0.13 m/ns. Saturated sediments obtain lower values: 0.05 – 0.08 m/ns for the same type of sediments. Other data to support the idea of the location of the watertable is the V_p/V_s – ratio with depth in figure 3.17. An increase in the ratio at around 2 m may represent the watertable. The different seismic properties between the P- and S-waves, makes it not possible for S-waves to “see” the watertable while the P-wave will experience a suddenly increase in velocity. Investigation from the Norwegian road

authorities also states that the watertable is located at depths between 0 and 4.5 m below the ground in the area west of the 2007 summer campaign (Fig. 1.1 left) (Sleipnes 2007). It is important to remember that the V_p/V_s – profiles are produced by manual velocity picking from two different 2-D velocity profiles with different uncertainties from the start. Therefore the reliability of the plot might contain large uncertainties which must be considered.

The general higher resistivity values from the data collected in the area ~20 m further north of the reference profile (Fig. 3.18 below) is probably due to that the bedrock is at shallower depths in this area. Geological maps from the Norwegian Geological Survey (NGU) confirm this finding.

Figure 4.3 displays a possible interpretation of the 50 MHz GPR image (Fig. 3.2). As mentioned earlier, a possible interpretation of the area might be that the reflector visible at 7 m depth below line 1, and continuing east to form a channel-like structure (Fig. 3.1, 200-350 m on the reference profile), is an old erosional surface or part of a channel system in connection with the last ice age. If so the material is more compacted than the overlying material and this might be the explanation of the increase in V_p, V_s, the high resistivity value and the strong reflector on the 50 MHz GPR data. The evidence for the gneiss in the easternmost part of the figure is of course this GPR image in addition to resistivity values above 2300 Ohmm and the fact that gneiss was visible at the surface just east of this profile.

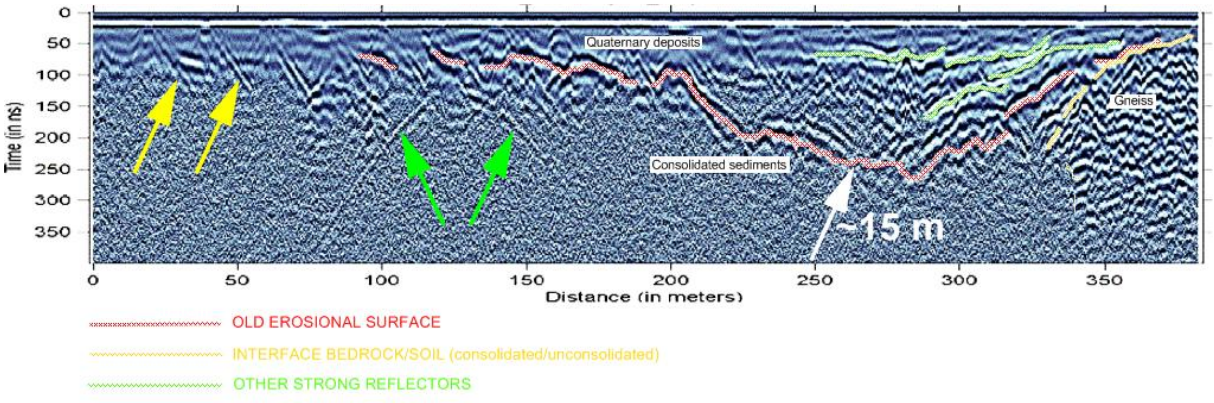

Figure 4.3 A possible interpretation of the area added to the 50 MHz GPR profile. The red line indicates a strong reflector belonging to a possible erosional surface or a part of a channel system in connection with the last ice age. Above this interface the area is filled with unconsolidated Quaternary deposits, while beneath the sediments are more compacted. The yellow line marks the interface between bedrock and overlying sediments. The green lines represent other discontinuous strong reflectors. Yellow and green arrows point out diffraction hyperbolas. Modified after Lecomte *et al.* (2008).

The channel-like structure might function as a drainage channel in periods with heavy precipitation. If the pore pressure increases and thin clay layers are present, even though there is no clear proof for that, a weak detachment layer may be formed. Longva *et al.* (2003) supports the theory that excess of pore pressure was one of the trigger mechanisms in the 1996 slide. If in addition an explosion from construction work is taken place nearby, this may also contribute as a trigger mechanism for a future slide. This has happened before in the area to the west (Fig. 1.1 left) and might happen again if not precautions are taken into consideration (Sleipnes 2007).

A possible idea for future work in the area might be to do a seismic CMP reflection analysis for better determination of the different layers and to gain better understanding of the western part of the area. Another operation could be to collect some sediment cores for correlation with the geophysical data. Three locations for these samples could probably be at distances 70 m, 150 m and 300 m on figure 4.3. That would provide lithological information concerning the presence of clay layers and determine the differences in geological setting beneath line 1, line 2 and line 3. It would also be interesting to study the 250 MHz GPR data from the two grids displayed on the reference profile (Fig. 3.1) in addition with the OhmMapper data from the same area. These results will be available from ICG in the near future. Unfortunately too small amount of passive seismic data were recorded in the summer campaign 2007 to give significant results. Other present projects related to the area: Eugene Morgan (exchange student from Tufts University, Massachusetts) is doing his pre-ph.D work, also at ICG, on the role of free gas in destabilizing the offshore slope. Creation of a 3-D model of the present-day gas quantity beneath the fjord bed is one of the problems related to this study.

5. Conclusions

- An optimal method for how to summarize the different dispersion images related to the 2M-SASW program would be helpful to obtain even better dispersion image resolution. This would provide better modal separation and higher accuracy in velocity picking in the low frequency area. The result would be better resolution for the different layers in the final model. The RDWs could be set to a smaller distance for a velocity average of a smaller area, hence a more correct 2-D V_s-profile.

- The 50 MHz GPR equipment is a fast and reliable method for gaining an overview of the area and for planning further geophysical investigations.

- The geological setting related to line 1, line 2 and line 3 is completely different. This comes through with the different results at the respective locations acquired by the different geophysical tools (P- and S-wave velocity profiles, GPR data and resistivity). The importance of the different qualities related to the different geophysical tool must not be underestimated. Data from only one type of investigation is not reliable all alone.

- The watertable is most likely to be found at depths of 2-2.5 m, by studying the V_p/V_s-ratio and the GPR CMP data. In addition was information from the Norwegian road authorities helpful.

- Clay is not directly detected by the different geophysical tools. But there might be clay layers or clay lenses too thin or too small for direct localization. This is more probable in the western part of the reference profile (Fig. 3.1). The future collection of sediment cores could probably verify this in addition to be helpful to correlate lithological boundaries with the geophysical data.

References

Best A.I., Clayton C.R.I., Longva O. and Szuman M. 2003. The role of free gas in the activation of submarine slides in Finneidfjord. *First International Symposium on Submarine Mass Movements and their Consequence.* European Geophysical Society-American Geophysical Union-European Union Geosciences Joint Meeting. Nice, France, April 6-11. Kluwer, 491-498.

Bjerrum, L. 1954. Geotechnical properties of Norwegian marine clays. *Géotechnique* 4, 49–69.

Bodet L., van Wijk K., Bitri A., Abraham O., Cote P., Grandjean G. and Leparoux D. 2004a. Surface wave dispersion inversion when the 1D assumption breaks down. Submitted to *Journal of Environmental & Engineering Geophysics,* October 2004.

Bodet L., Abraham O., Bitri A., Leparoux D. and Côte P. 2004b. Effect of dipping layers on seismic surface waves profiling: a numerical study. In *Symposium on the Application of Geophysics to Engineering and Environmental Problems, Proceedings.* Colorado Springs, Colorado. February 22-26, 2004.

Bohlen T., Kugler S., Klein G. and Theilen F. 2004. 1.5D inversion of lateral variation of Scholte-wave dispersion. *Geophysics* 69, 330-334.

Bolt B.A. 1982. *Inside the Earth.* San Francisco: Freeman. 191 pp.

Bullen K.E. 1963. *An introduction to the theory of seismology*. New York: Cambridge University Press. 381 pp.

Davis J.L. and Annan A.P. 1989. Ground-penetrating radar for high-resolution mapping of soil and rock stratigraphy. *Geophysical Prospect* 3, 531-551.

Elverhøi A. 2000. Om istider og klima I fortid og framtid. *In* Bjørlykke K. (ed.) *Geologi, miljø og ressurser*. Institutt for geologi ved Universitetet i Oslo. 79-88.

Furseth A. 2006. *Skredulykker I Norge*. Oslo: Tun Forlag. 207 pp.

Grandjean G. and Bitri A. 2006. 2M-SASW: Multifold multichannel seismic inversion of local dispersion of Rayleigh waves in laterally heterogeneous subsurfaces: application to the Super-Sauze earthflow, France. *Near Surface Geophysics* 4, 367-375.

Grandjean G. and Sage S. 2004. JaTS: a fully portable seismic tomography software based on Fresnel wavepaths and a probabilistic reconstruction approach. *Computers & Geosciences* 30, 925-935.

Hansen L., Eilertsen R.S., Solberg I.L., Sveian H. and Rokoengen K. 2007. Facies characteristics, morphology and depositional models of clay-slide deposits in terraced fjord valleys, Norway. *Sedimentary Geology* 202-4, 710-729.

Herrmann R.B. 2002. Computer *programs in seismology*. Department of Earth and Atmospheric Sciences, Saint Louis University.

Høeg K. 2000. Problemer med tunnel, damanlegg, skredfare eller oljereservoiret – spør ingeniørgeologen. *In* Bjørlykke K. (ed.) *Geologi, miljø og ressurser*. Institutt for geologi ved Universitetet i Oslo. 229-240.

Janbu N. 1996. *Raset i Finneidfjord – 20. juni 1996*. Unpublished expert's report prepared for the County Sheriff of Nordland. (Report 1.1).

Kearey P., Brooks M. and Hill I. 2005. *An introduction to geophysical exploration*. Oxford: Blackwell publishing. 262 pp.

Keilis-Borok V.I., Levshin A.L., Yanovskya T.B., Lander A.V., Bukchin B.G., Barmin M.P., Ratnikova L.I. and Its E.N. 1989. *Seismic surface waves in laterally inhomogeneous Earth*. Dordrecht: Kluwer academic publishers. 304 pp.

Lecomte I., Bano M., Hamran S.E., Dalsegg E., Nielsen K.M., Nielsen M.H., Douillet G., Frery E., Guy A. and Volesky S. 2008. Submarine slides at Finneidfjord (Norway): Geophysical investigations. In *Symposium on the Application of Geophysics to Engineering*

and Environmental Problems, proceedings 56, version 2. Philadelphia, Pennsylvania. April 6, 2008.

Longva O., Janbu N., Blikra L.H. and Bøe R. 2003. The 1996 Finneidfjord slide; seafloor failure and slide dynamics. *Advances in natural and technological hazards research* 19, 531-538.

Menke W. 1989. *Geophysical data analysis: Discrete inverse theory*. International geophysics series 45. New York: Academic Press. 289 pp.

Meteorologisk institutt. 2006. *Klimatologisk månedsoversikt Oktober/November.* Available at: http://met.no/Forskning/Publikasjoner/metno_info/2006 (Accessed 30.05.2008)

Miller R.D., Xia J., Park C.B. and Ivanov J. 1999. Multichannel analysis of surface waves to map bedrock. *The Leading Edge* 18, 1392-1396.

O'Neill A. 2003. *Full waveform reflectivity for Modeling, Inversion and Appraisal of Seismic Surface Wave Dispersion in Shallow Site Investigations.* PhD thesis, the University of Western Australia, School of Earth and Geographical Sciences (North).

Orozco C. 2003. *Inversion method for spectral analysis of surface waves (SASW).* PhD thesis, Georgia Institute of Technology, Georgia, USA.

Park C.B., Miller R.D. and Xia J. 1999a. Multimodal analysis of high frequency surface waves. In *Proceedings of Symposium on the Application of Geophysics to Engineering and Environmental Problems.* Oakland, California. March 14-18, 1999. 115-121.

Park C.B., Miller R.D. and Xia J. 1999b. Multichannel analysis of surface waves. *Geophysics* 64, 800-808.

Rayleigh J.W.S. 1885. On waves propagated along the plane surface of an elastic solid. *Proceedings of the London Mathematical Society* 17, 4-11.

Reynolds J.M. 1997. *An introduction to applied and environmental geophysics.* Chichester: John Wiley and sons. 796 pp.

Richart F.E., Hall J.R. and Woods R.D. 1970. *Vibrations of soils and foundations*. New Jersey: Prentice-Hall, Inc. 414 pp.

Rix G.J. and Leipski E.A. 1991 Accuracy and resolution of surface wave inversion. *In* Bhatia S.K. and Blaney G.W. (eds.) *Recent advances in instrumentation, data acquisition and testing in soil dynamics*. American Society of Civil Engineers, 17-32.

Sleipnes A. 2007. *Geoteknikk RV808-01: Varpen XE6 – Hemnesberget fl. Undersjøiske utglidninger ved Kleivneset*. Statens vegvesen Region nord. (Report nr. 2005/041536-015).

Socco L.V. and Strobbia C. 2004. Surface-wave method for near-surface characterization: a tutorial. *Near Surface Geophysics* 2, 165-185.

Stein S. and Wysession M. 2003. An *introduction to seismology, earthquakes, and earth structures*. Oxford: Blackwell publishing.

Stokoe K.H., II, Wright G.W., James A.B. and Jose M.R. (1994) Characterization of geotechnical sites by SASW method. *In* Woods R. D. (ed.) *Geophysical characterization of sites*. New Dehli: Oxford Publishers.

Tokimatsu K., Kuwayama S., Tamura S. and Miyadera Y. 1991. Effects on multiple modes on Rayleigh wave dispersion characteristics. *Soils and foundations* 31-2, 153-163.

Theimer B.D., Nobes D.C. and Warner B.G. 1994. A study of the geoelectrical properties of peatlands and their influence on ground-penetrating radar surveying. *Geophysical Prospect* 42, 179-209.

van Heteren S., Fitzgerald D.M., McKinlay P.A. and Buynevich I.V. 1998. Radar facies of paraglacial barrier systems: coastal New England, USA. *Sedimentology* 45, 181-200.

van Overmeeren R.A. 1994. Georadar for hydrogeology. *First Break* 12, 401-408.

van Wijk K. 2003. *Multiple scattering of surface waves*. PhD thesis, Colorado School of Mines, Golden, Colorado, USA.

Xia J., Miller R.D. and Park C.B. 1999. Configuration of near surface shear wave velocity by inverting surface wave. In *Proceedings of Symposium on the Application of Geophysics to Engineering and Environmental Problems.* Oakland, California. March 14-18, 1999. 95-104.

Nazarian S., Stokoe K.H. and Hudson W.R. 1983. Use of spectral analysis of surface waves method for determination of moduli and thickness of pavement system. *Transportation Research Record* 930, 38-45.

Appendix

A.1 Wavefield transformation method

According to Park *et al.* 1999a the dispersion image can be obtained by the following method:

After a seismic acquisition, there will be a shot gather represented in the offset-time (x-t) domain as u(x,t). The Fourier transformation is applied on the time axis to obtain U(x,ω):

$$U(x,\omega) = \int u(x,t)e^{i\omega t}\, dt \tag{16}$$

U(x,ω) can then be expressed by two separate terms:

$$U(x,\omega) = P(x,\omega)A(x,\omega) \tag{17}$$

Where P(x,ω) and A(x,ω) represents the phase and amplitude spectrum. In U(x,ω), every frequency is separated from each other. The phase spectrum, P(x,ω), contains all the information about the arrival time, hence dispersion properties. While the amplitude spectrum, A(x,ω), holds information such as attenuation and geometrical spreading. Therefore P(x,ω) can be expressed as $e^{-i\Phi x}$, and consequently the spectrums as:

$$U(x,\omega) = e^{-i\Phi x} A(x,\omega)$$

where $\Phi = \omega / c_\omega$, ω is frequency in radian and c_ω is the phase velocity for ω. Attenuation and geometrical spreading with offset is compensated for, by applying normalization of U(x,ω).

$V(\omega,\varphi)$ is calculated by the following integral transformation of U(x,ω) :

$$V(\omega,\varphi) = \int e^{i\varphi x}\ [U(x,\omega)/|U(x,\omega)|]\ dx$$
$$= \int e^{-i(\phi-\varphi)x}\ [A(x,\omega)/|A(x,\omega)|]\ dx \qquad (18)$$

This integral transformation can be thought of as summing each frequency over offset after applying an offset-dependent phase shift φ. Many different values of φ are tried for each ω. The optimal shift for a given frequency is the one that results in the largest energy after summation over offset x, and is given by:

$$\varphi = \Phi = \omega/c_w \qquad (19)$$

Finally to obtain the frequency-phase velocity image I(ω, $\mathbf{C}_\omega$) from V(ω, φ) simply transform a coordinate transform $\mathbf{C}_\omega = \omega/\varphi$. For a given ω in the dispersion image, there will be peaks along the phase velocity axis that satisfy equation 19 for a given ω. The dispersion curve is found by connecting several peaks on different frequencies to form a line.

A.2 Further development by Grandjean and Bitri (2006).

Grandjean and Bitri's (2006) new algorithm is based on equation (18) by Park *et al.* (1999a). Further they introduce for a laterally contrasting media, a restricted narrow receiver distance window (RDW) ($x_1 - x_2$) for which the dispersion image is calculated. With x_1 and x_2 being the limits of the RDW, equation 18 can be rewritten as

$$E(\omega,c_\omega)_{x_1}^{x_2} = \int_{x_1}^{x_2} e^{-i\left[\Phi-\frac{\omega}{c_\omega}\right]x}\ [A(x,\omega)/|A(x,\omega)|]\ dx \qquad (20)$$

Equation 20 allows computation of the dispersion image from only a single shot gather and therefore only a limited number of traces. To increase the number of traces used for

computation of the dispersion image, the next shot along the same profile is used within the same RDW. A new quantity is introduced $E_L(s,\omega,c_\omega)_{x_1}^{x_2}$, representing the local dispersion image for a shot from a distance s:

$$E_L(s,\omega,c_\omega)_{x_1}^{x_2} = \int_{x_1}^{x_2} e^{-i\left[\Phi-\frac{\omega}{c_\omega}\right]x}\,[A(s,x,\omega)/|A(s,x,\omega)|]\,dx \tag{21}$$

A summation term for the different dispersion images computed within the same RDW is done, so that the dispersion images can be stacked together, increasing the signal-to-noise ration and hence the resolution:

$$E_L(\omega,c_\omega)_{x_1}^{x_2} = \iint_{x_1}^{x_2} e^{-i\left[\Phi-\frac{\omega}{c_\omega}\right]x}\,[A(s,x,\omega)/|A(s,x,\omega)|]\,dx\,ds \tag{22}$$

B.1 Figures related to the shear-wave velocity inversion

Figures upper left: vertical axis, time in seconds. Horizontal axis, distance to source in meters

Figures upper right: vertical axis, frequency in Hz. Horizontal axis, velocity in m/s

Line 1

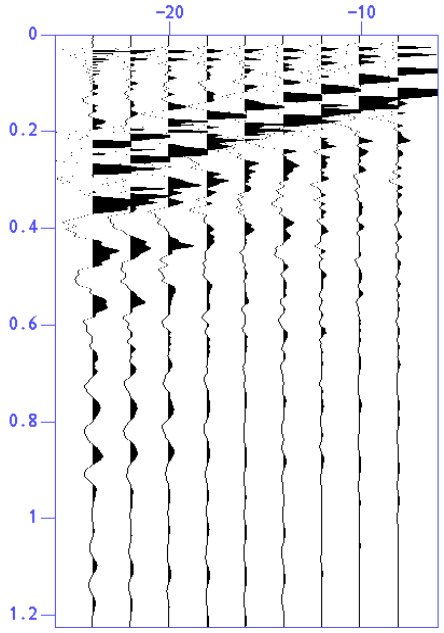

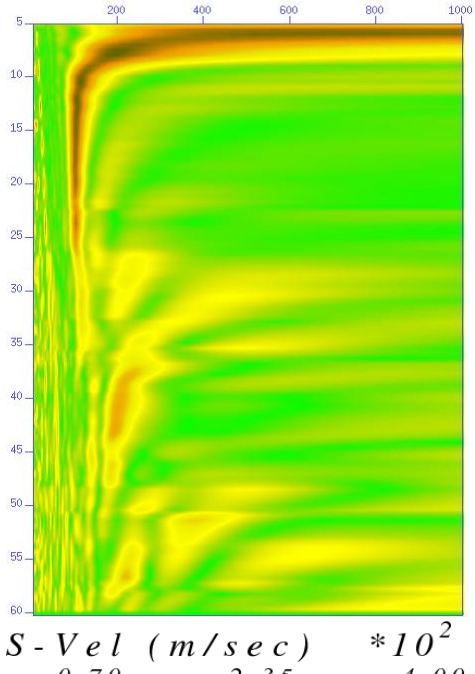

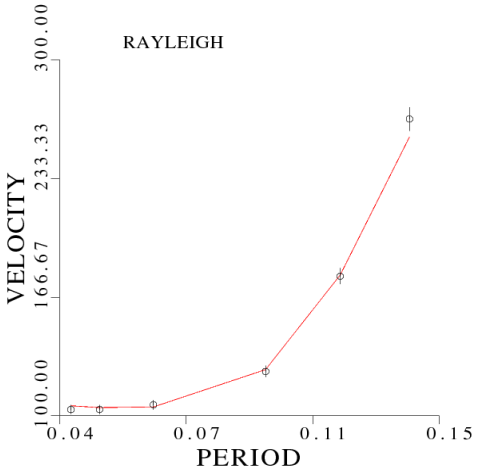

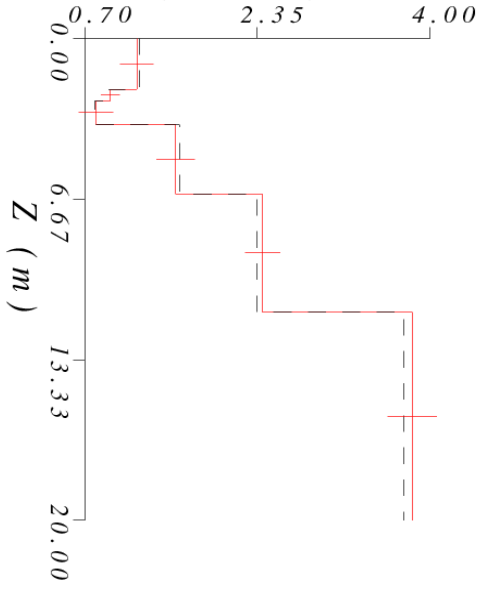

Distance receiver array: 0 – 16 m, 9 geophones. Distance source – first receiver: 8 m

Correlation coefficient: Layer 1 : 0.90

Layer 2 : 1.0E-01

Layer 3 : 0.75

Layer 4 : 0.60

Layer 5 : 0.53

Layer 6 : 0.41

Line 1

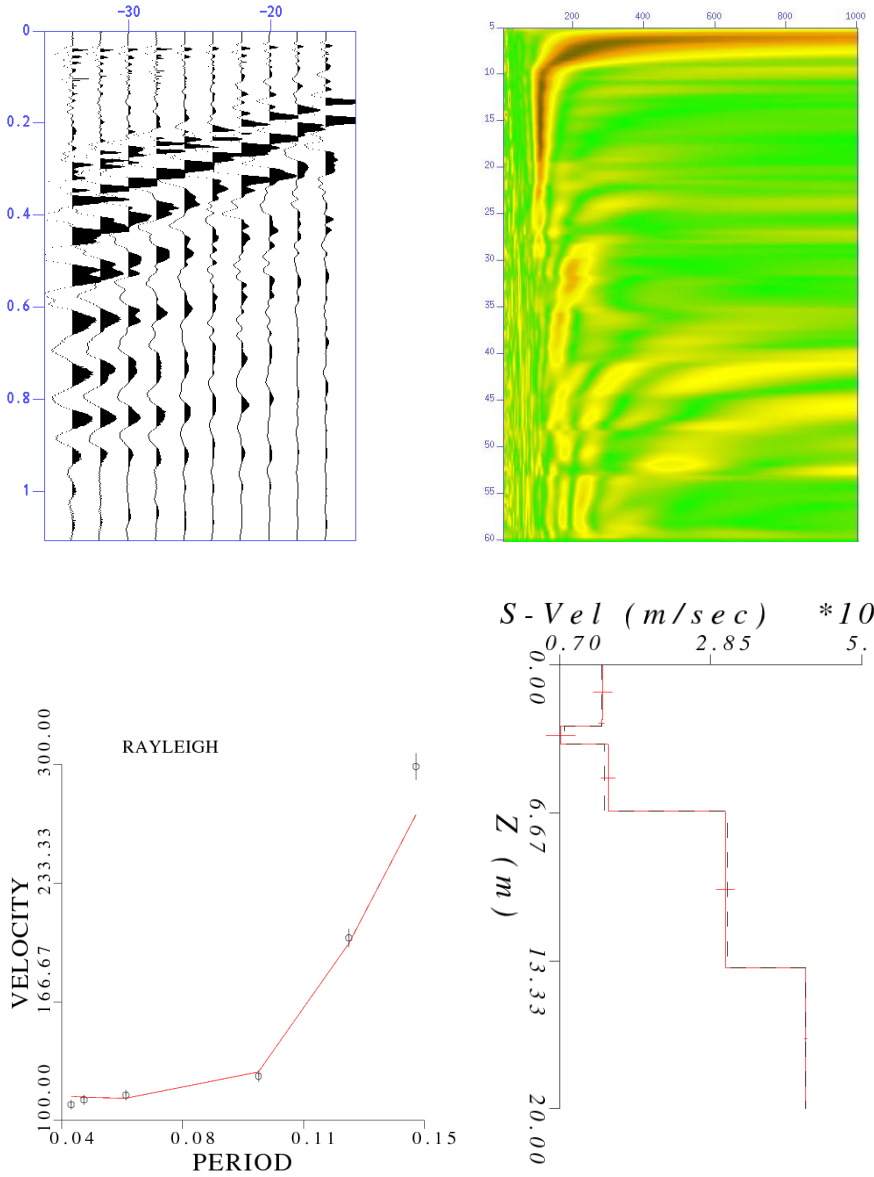

Distance receiver array: 1 – 21 m, 10 geophones. Distance source – first receiver: 15 m

Correlation coefficient: Layer 1 : 0.88

Layer 2 : 2.0E-02

Layer 3 : 0.51

Layer 4 : 0.20

Layer 5 : 0.13

Layer 6 : 1.5E-03

Line 1

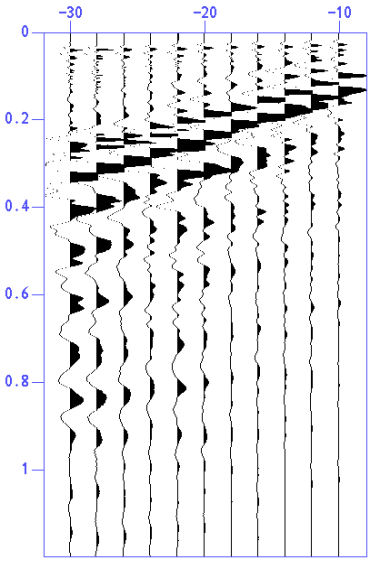

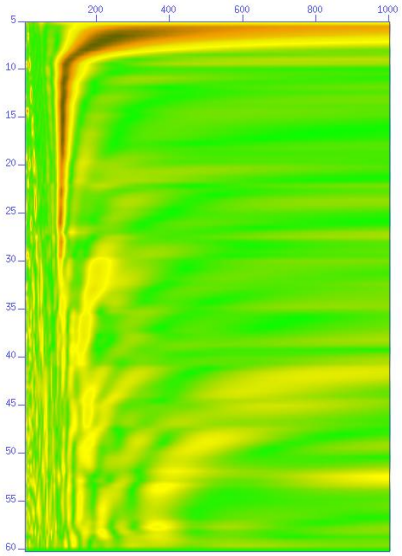

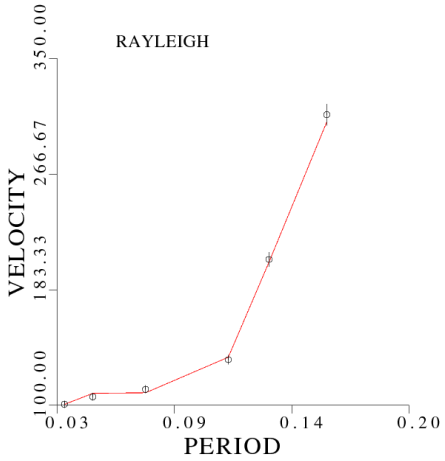

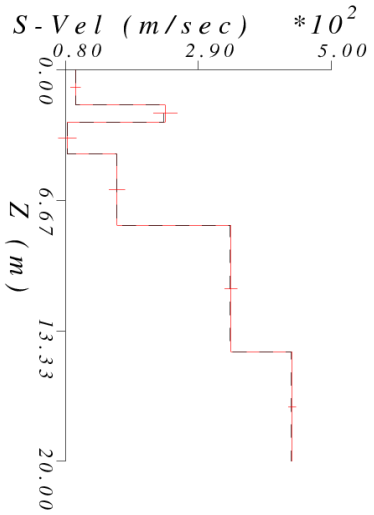

Distance receiver array: 6 – 26 m, 11 geophones. Distance source – first receiver: 10 m

Correlation coefficient: Layer 1 : 0.98

Layer 2 : 0.29

Layer 3 : 0.88

Layer 4 : 0.87

Layer 5 : 0.11

Layer 6 : 2.5E-02

Line 1

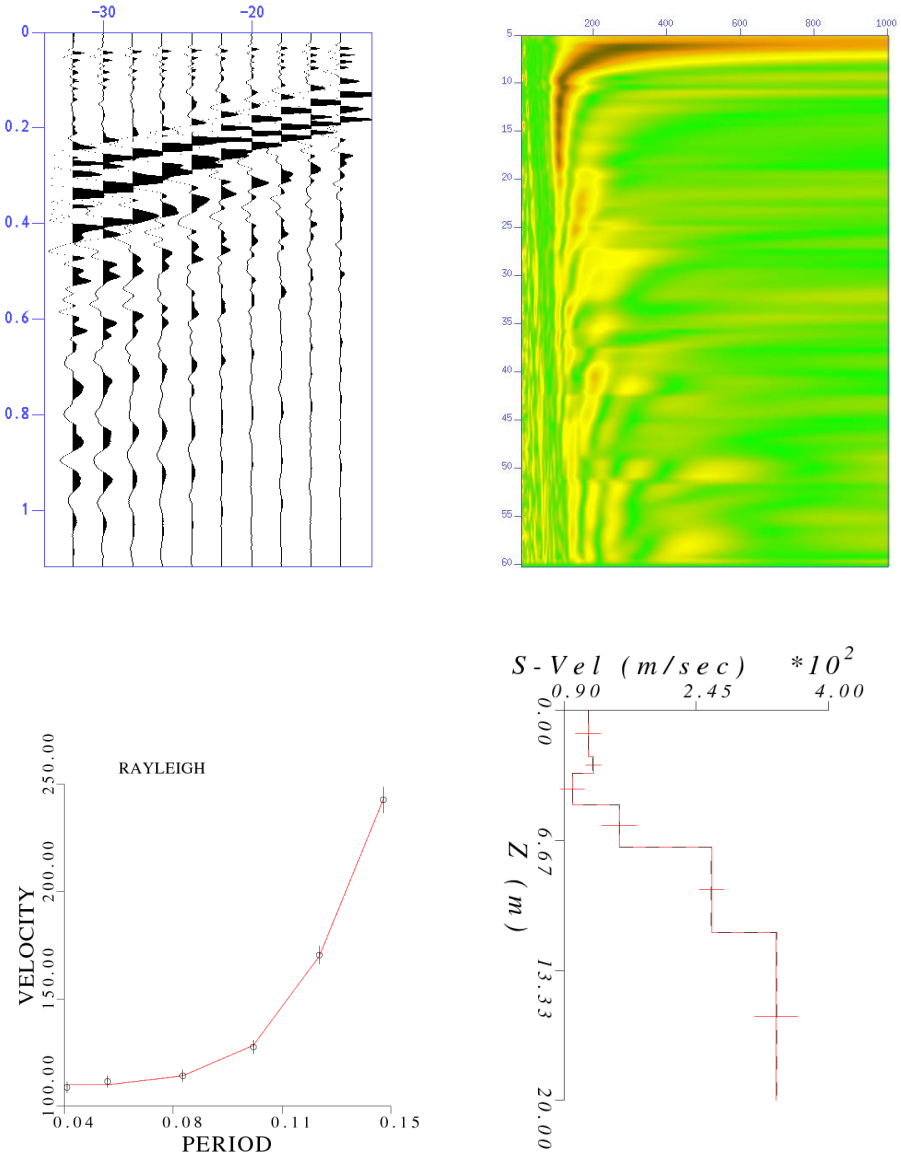

Distance receiver array: 11 – 31 m, 10 geophones. Distance source – first receiver: 13 m

Correlation coefficient: Layer 1 : 0.90

Layer 2 : 0.13

Layer 3 : 0.77

Layer 4 : 0.50

Layer 5 : 0.25

Layer 6 : 0.56

Line 1

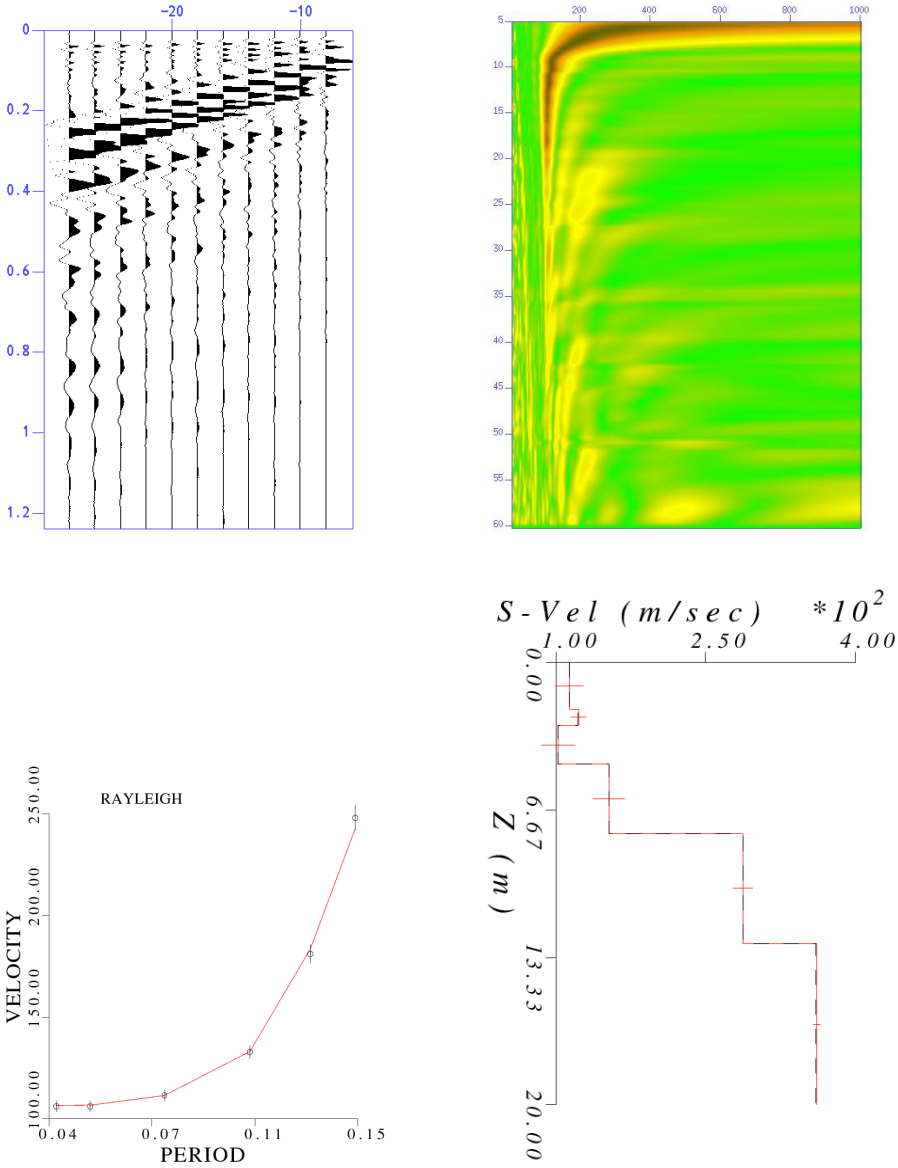

Distance receiver array: 16 – 36 m, 11 geophones. Distance source – first receiver: 8 m

Correlation coefficient: Layer 1 : 0.89

Layer 2 : 8.7E-02

Layer 3 : 0.79

Layer 4 : 0.77

Layer 5 : 9.7E-02

Layer 6 : 8.2E-03

Line 1

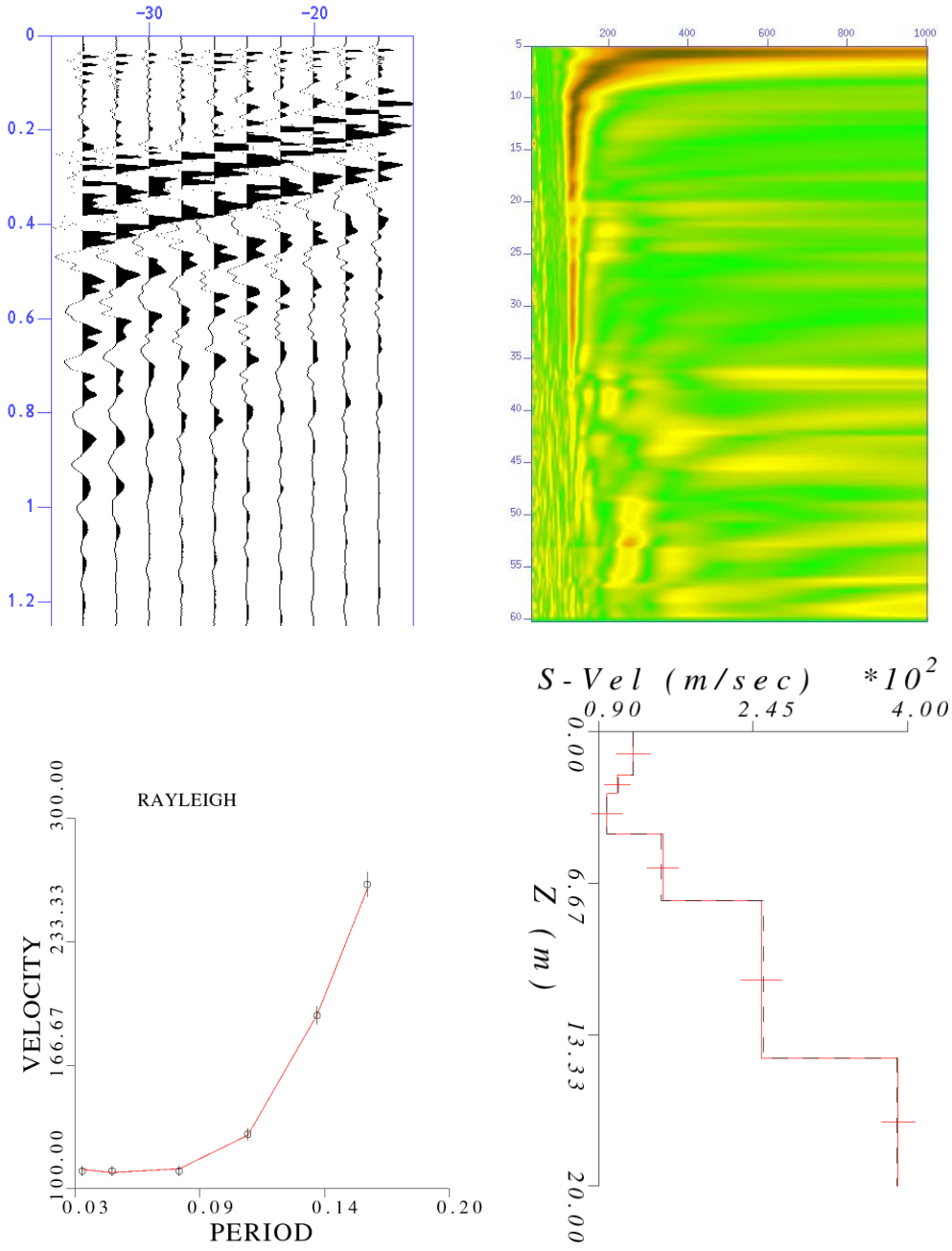

Distance receiver array: 21 – 41 m, 10 geophones. Distance source – first receiver: 15 m

Correlation coefficient: Layer 1 : error in model resolution matrix

Layer 2 : - -

Layer 3 : - -

Layer 4 : - -

Layer 5 : - -

Layer 6 : - -

Line 1

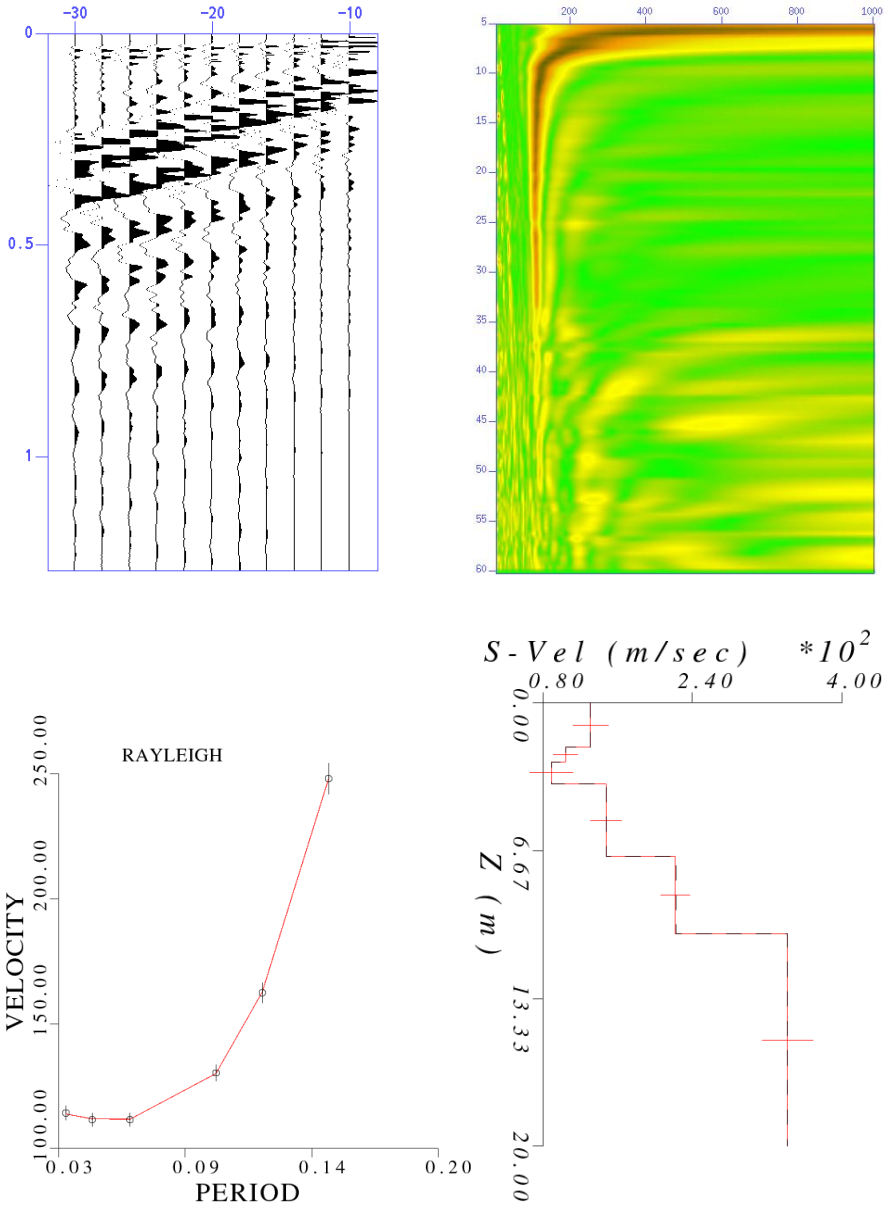

Distance receiver array: 26 – 46 m, 11 geophones. Distance source – first receiver: 10 m

Correlation coefficient: Layer 1 : 0.87

Layer 2 : 0.16

Layer 3 : 0.60

Layer 4 : 0.80

Layer 5 : 0.24

Layer 6 : 0.70

Line2

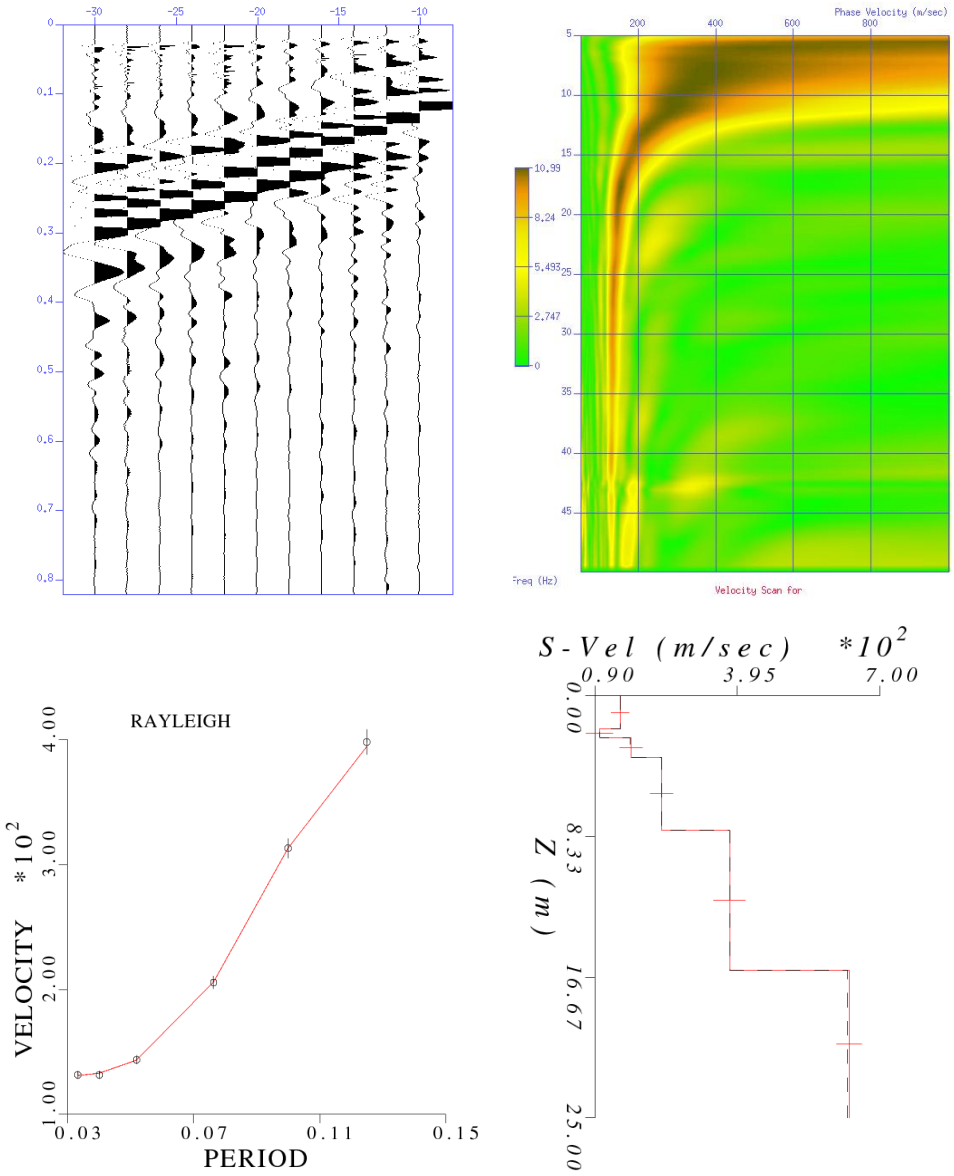

Distance receiver array: 0 – 20 m, 11 geophones. Distance source – first receiver: 10 m

Correlation coefficient: Layer 1 : 0.92

Layer 2 : 0.46

Layer 3 : 0.38

Layer 4 : 0.87

Layer 5 : 0.78

Layer 6 : 0.13

Line2

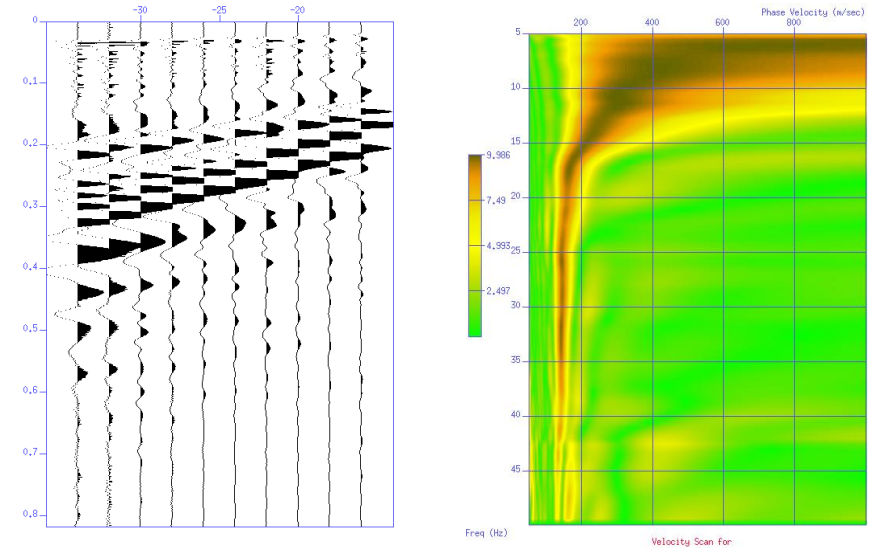

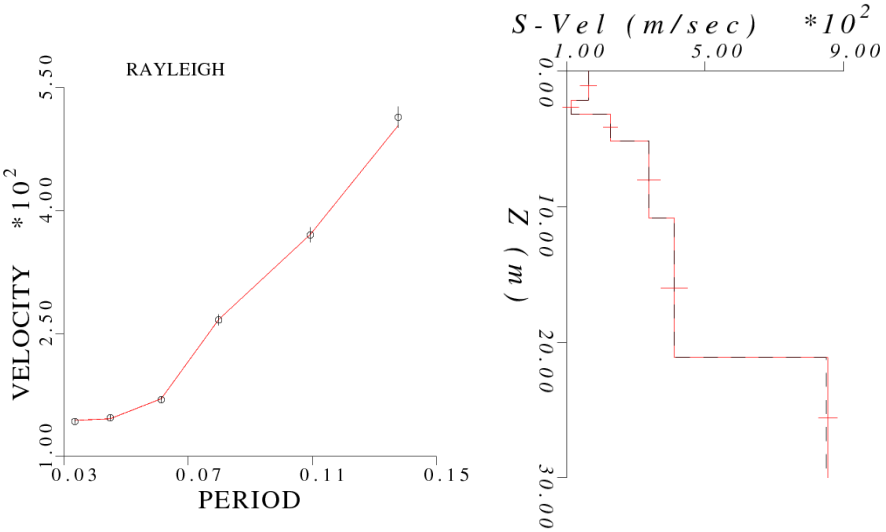

Distance receiver array: 5 – 25 m, 10 geophones. Distance source – first receiver: 15 m

Correlation coefficient: Layer 1 : 0.90

Layer 2 : 0.81

Layer 3 : 0.30

Layer 4 : 0.70

Layer 5 : 0.74

Layer 6 : 0.11

Line2

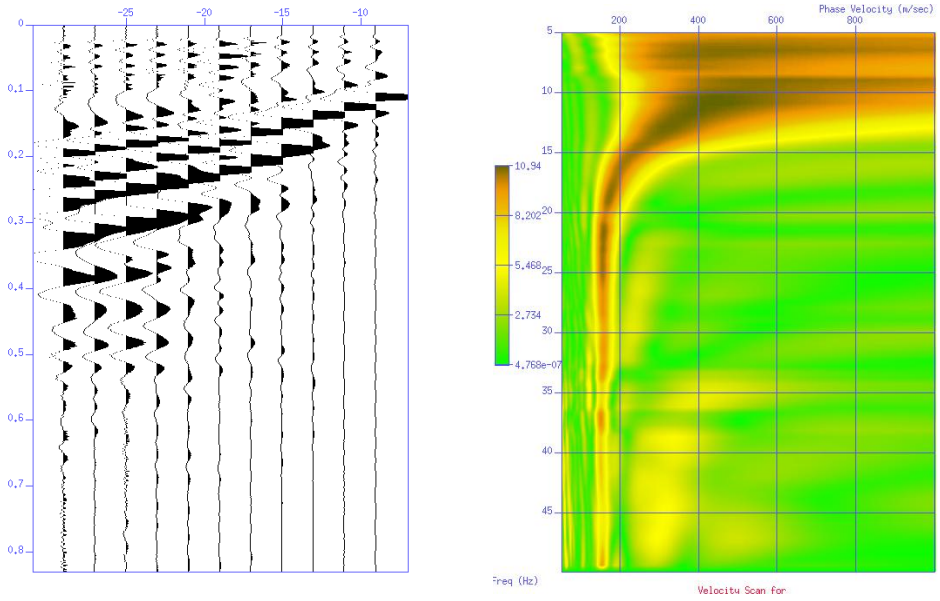

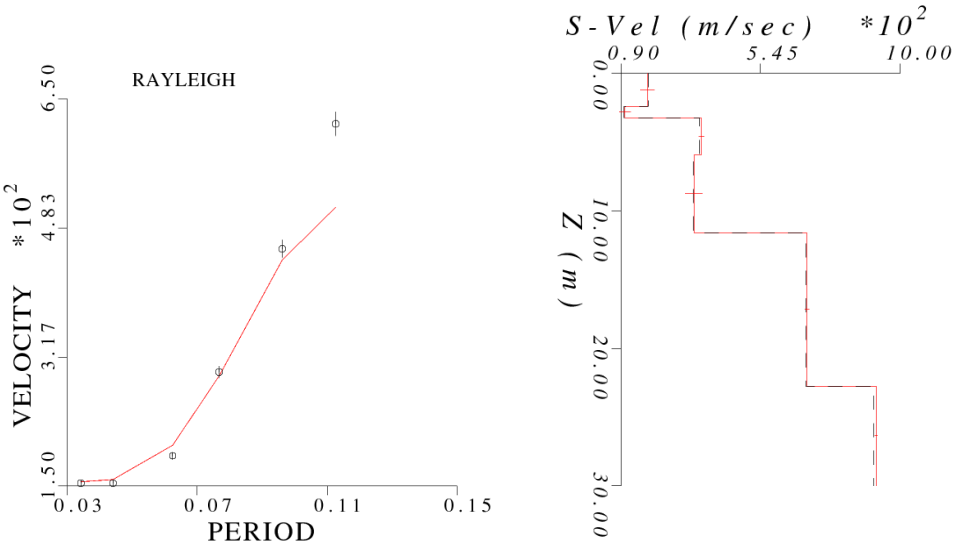

Distance receiver array: 10 – 30 m, 11 geophones. Distance source – first receiver: 8 m

Correlation coefficient: Layer 1 : 0.88

Layer 2 : 0.17

Layer 3 : 7.2E-02

Layer 4 : 0.79

Layer 5 : 1.2E-02

Layer 6 : 2.7E-03

Line2

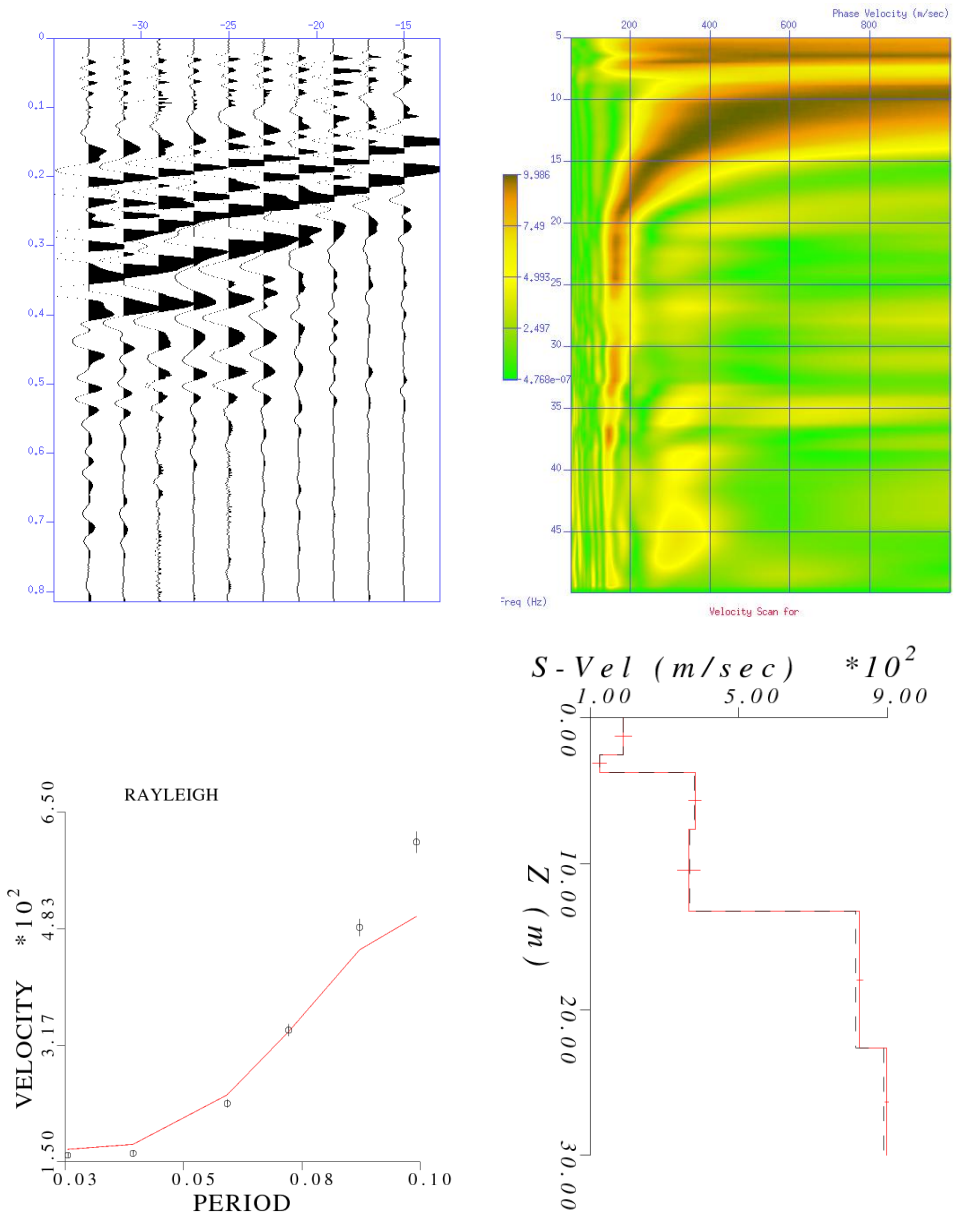

Distance receiver array: 15 – 35 m, 10 geophones. Distance source – first receiver: 13 m

Correlation coefficient: Layer 1 : 0.89

Layer 2 : 0.88

Layer 3 : 0.21

Layer 4 : 0.69

Layer 5 : 1.2E-02

Layer 6 : 3.4E-03

Line2

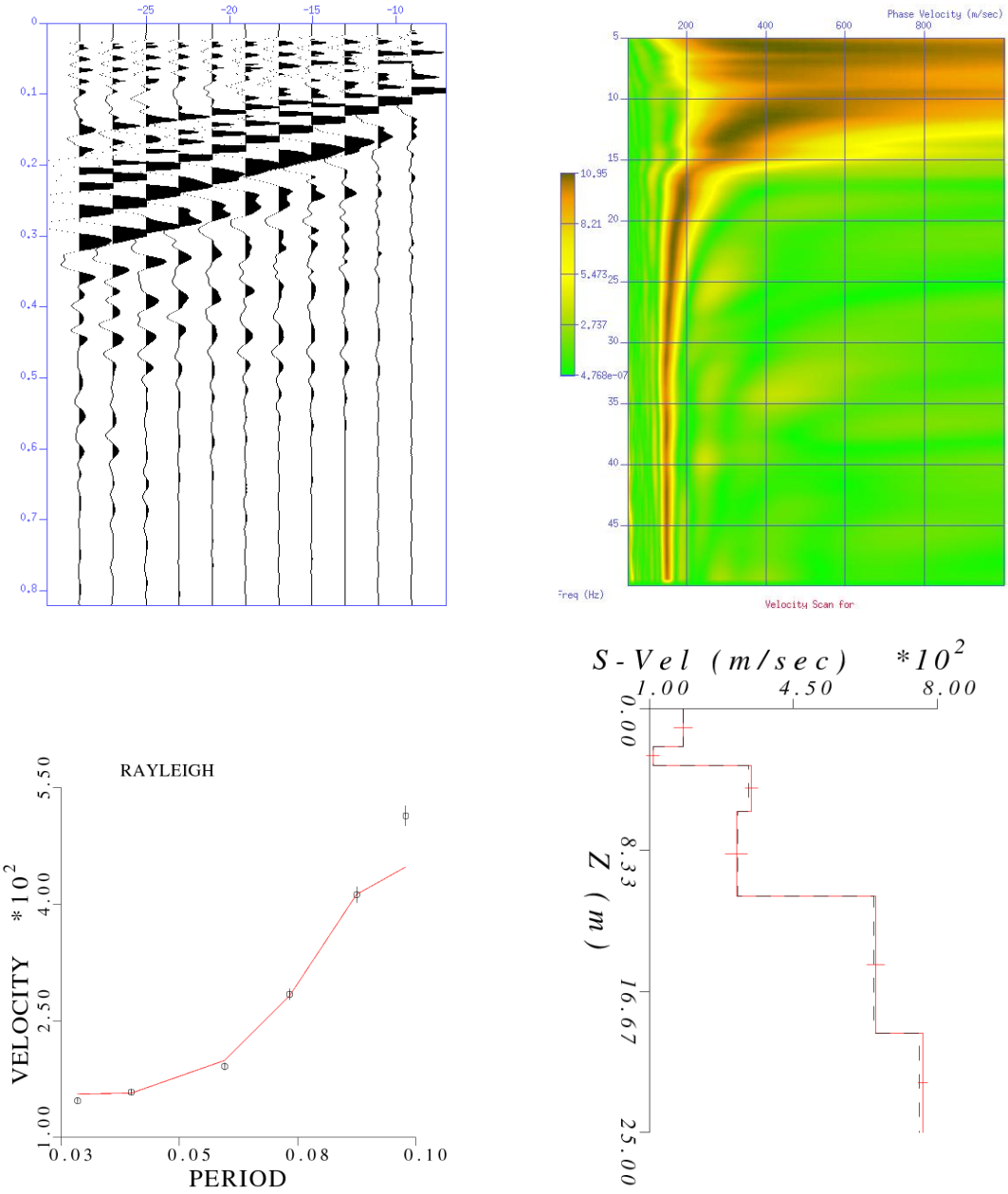

Distance receiver array: 20 – 40 m, 11 geophones. Distance source – first receiver: 9 m

Correlation coefficient: Layer 1 : 0.89

Layer 2 : 0.92

Layer 3 : 0.12

Layer 4 : 0.81

Layer 5 : 0.12

Layer 6 : 2.7E-02

Line2

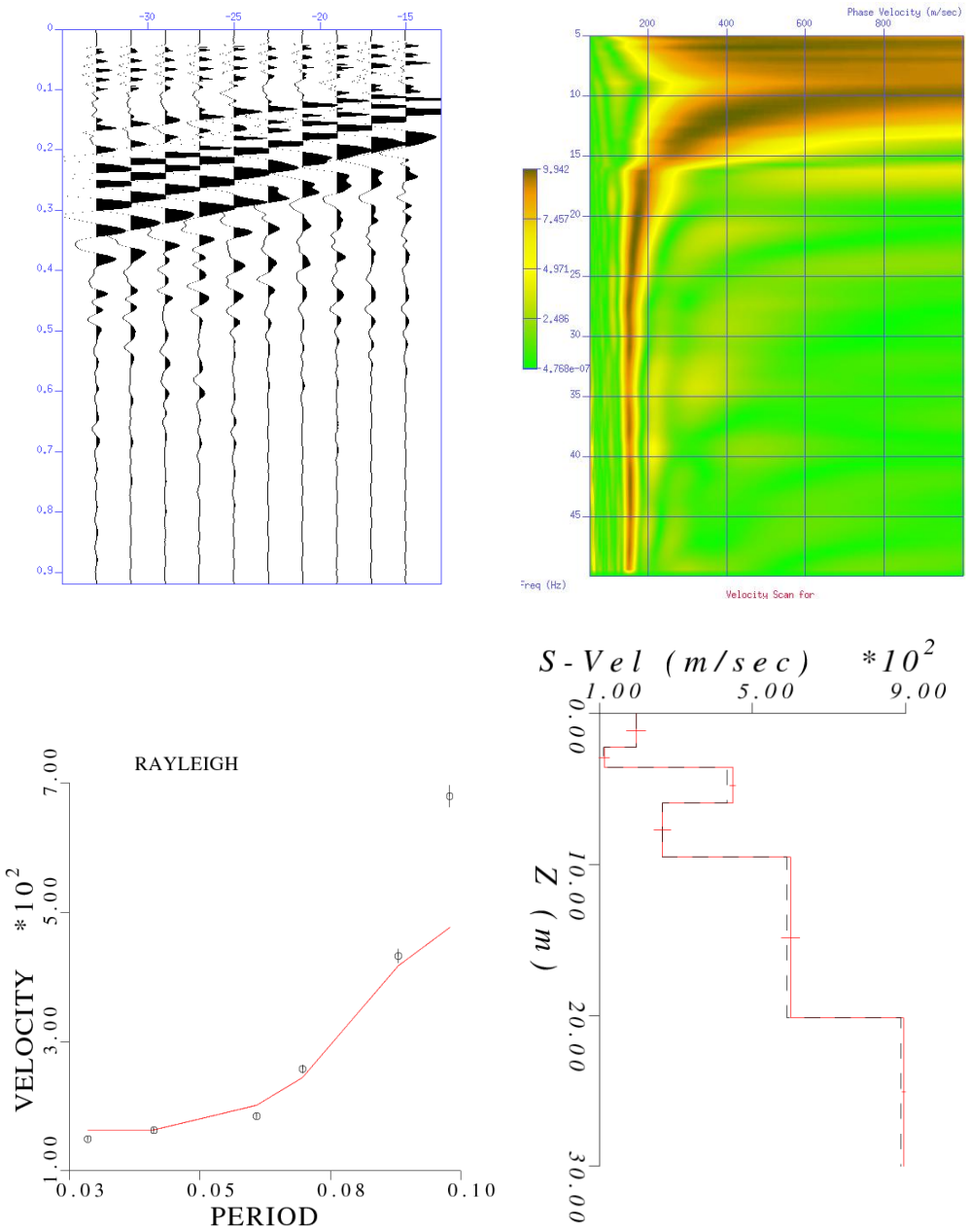

Distance receiver array: 25 – 45 m, 10 geophones. Distance source – first receiver: 14 m

Correlation coefficient: Layer 1 : 0.85

Layer 2 : 0.95

Layer 3 : 3.5E-02

Layer 4 : 0.74

Layer 5 : 0.27

Layer 6 : 5.0E-03

Line2

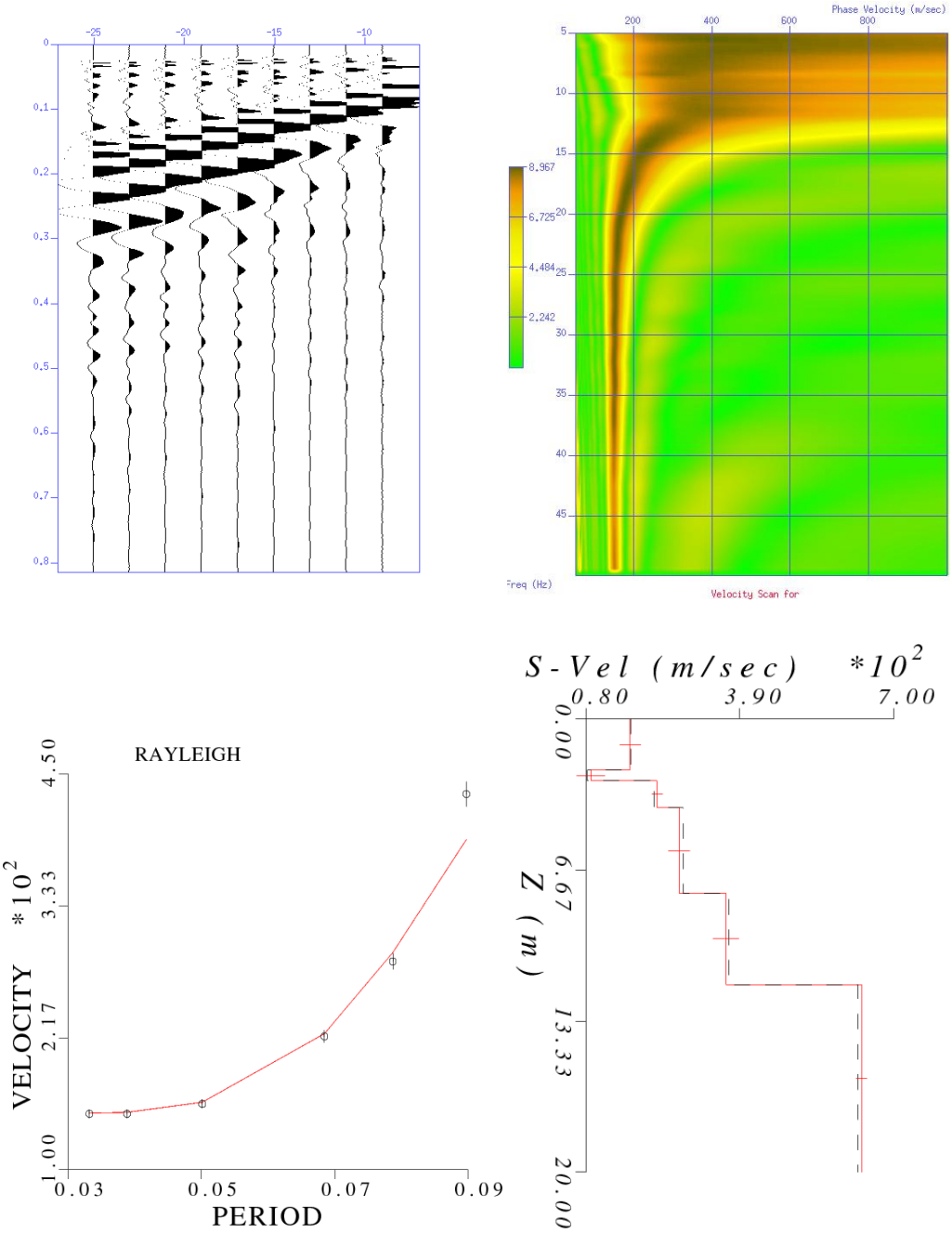

Distance receiver array: 30 – 46 m, 9 geophones. Distance source – first receiver: 9 m

Correlation coefficient: Layer 1 : 0.91

Layer 2 : 0.70

Layer 3 : 9.6E-02

Layer 4 : 0.74

Layer 5 : 0.28

Layer 6 : 2.0E-02

Line3

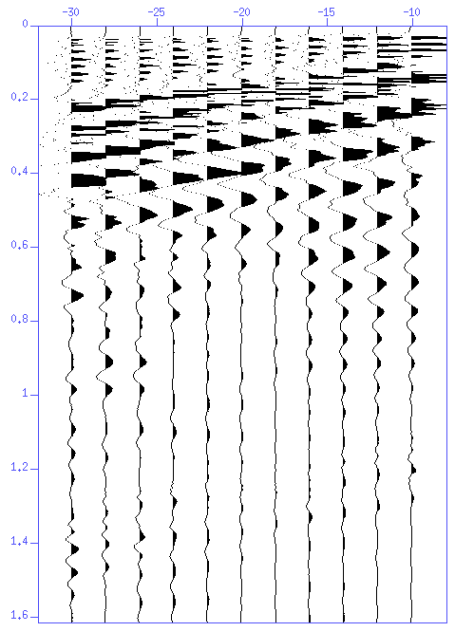

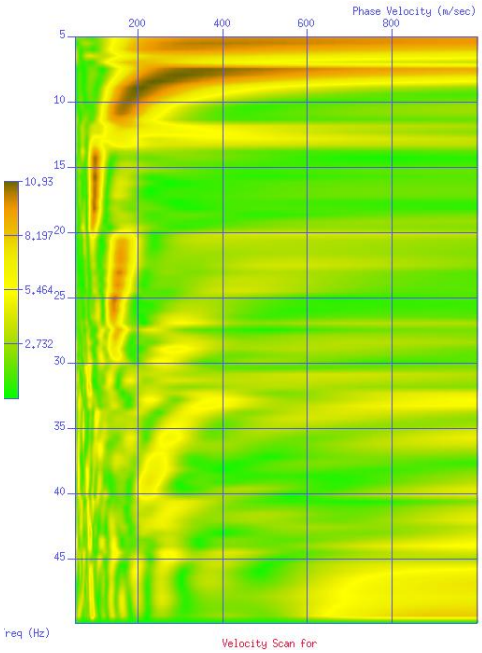

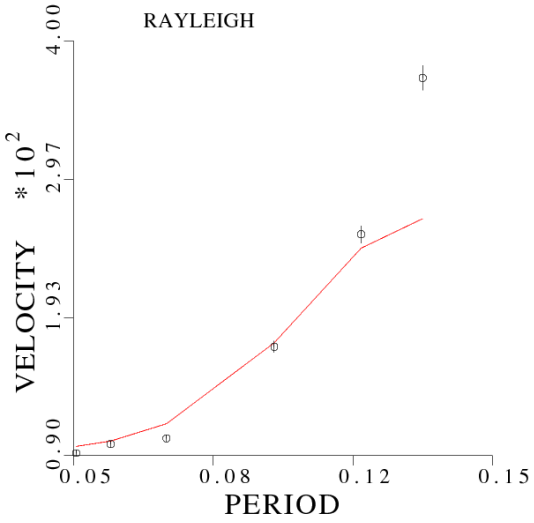

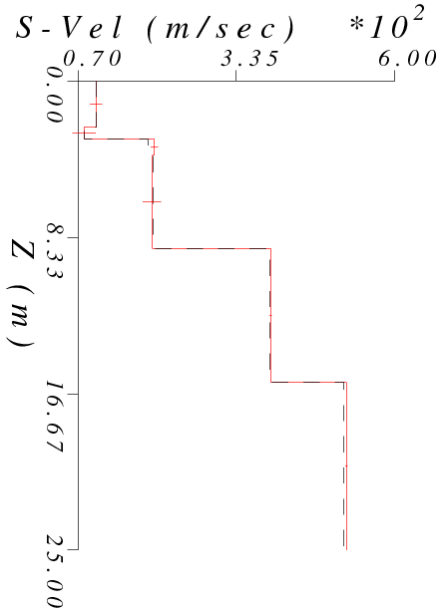

Distance receiver array: 0 – 20 m, 11 geophones. Distance source – first receiver: 10 m

Correlation coefficient: Layer 1 : 0.92

Layer 2 : 0.60

Layer 3 : 3.7E-02

Layer 4 : 0.83

Layer 5 : 4.0E-03

Layer 6 : 1.1E-03

Line3

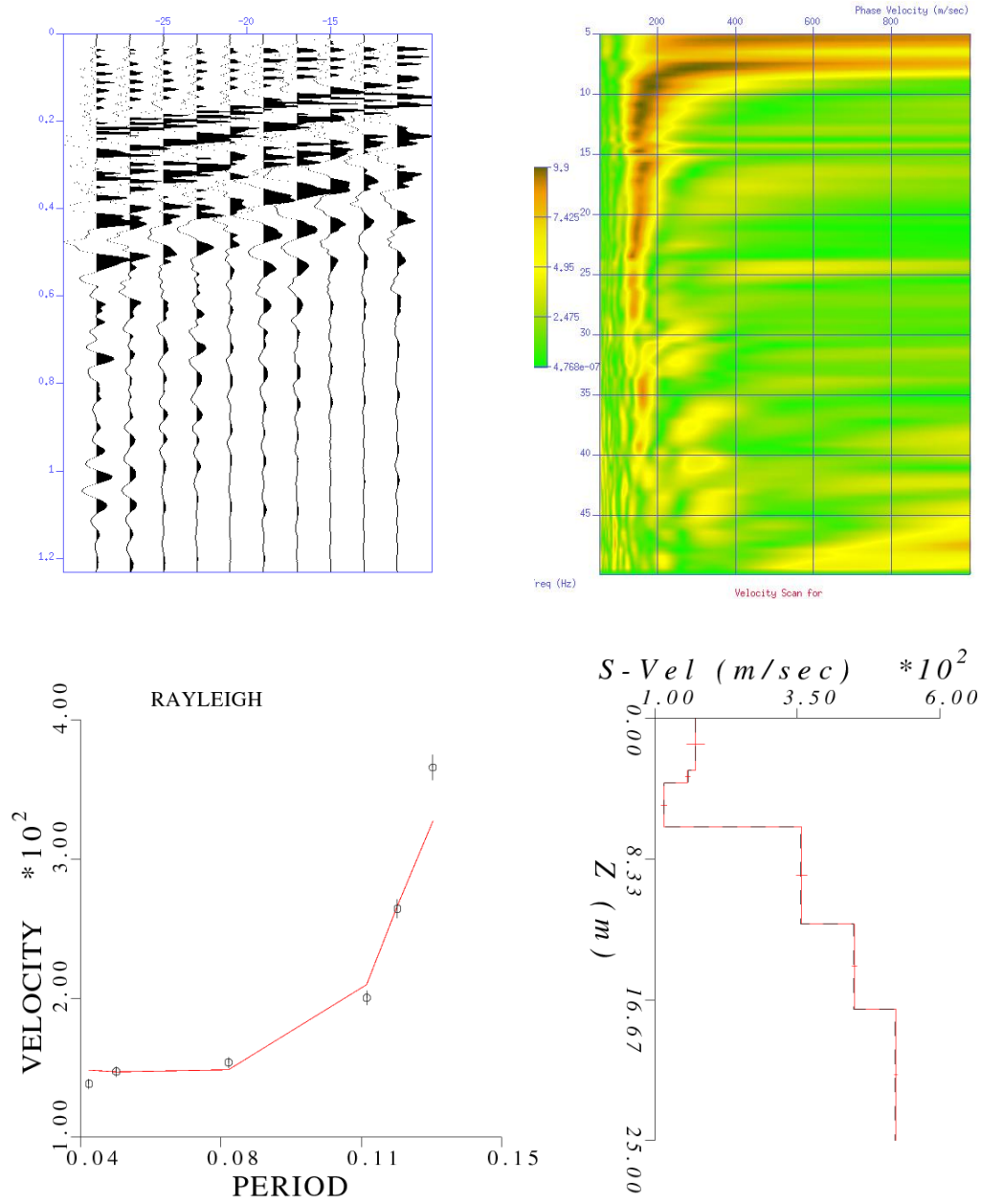

Distance receiver array: 5 – 25 m, 10 geophones. Distance source – first receiver: 10 m

Correlation coefficient: Layer 1 : 0.78

Layer 2 : 3.9E-02

Layer 3 : 0.94

Layer 4 : 9.0E-02

Layer 5 : 1.5E-02

Layer 6 : 3.6E-03

Line3

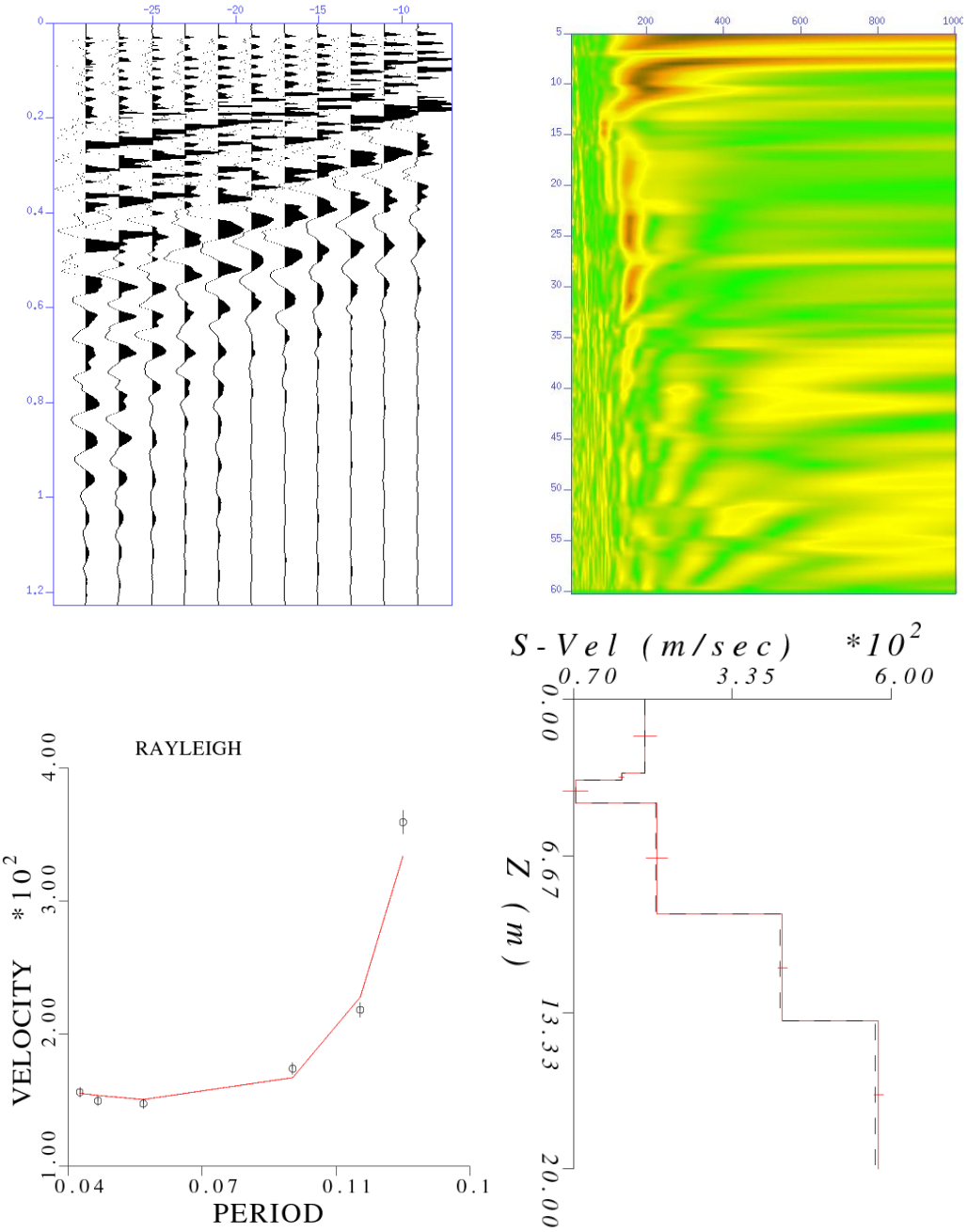

Distance receiver array: 10 – 30 m, 11 geophones. Distance source – first receiver: 9 m

Correlation coefficient: Layer 1 : 0.83

Layer 2 : 1.5E-02

Layer 3 : 0.67

Layer 4 : 0.76

Layer 5 : 4.1E-02

Layer 6 : 2.3E-02

Line3

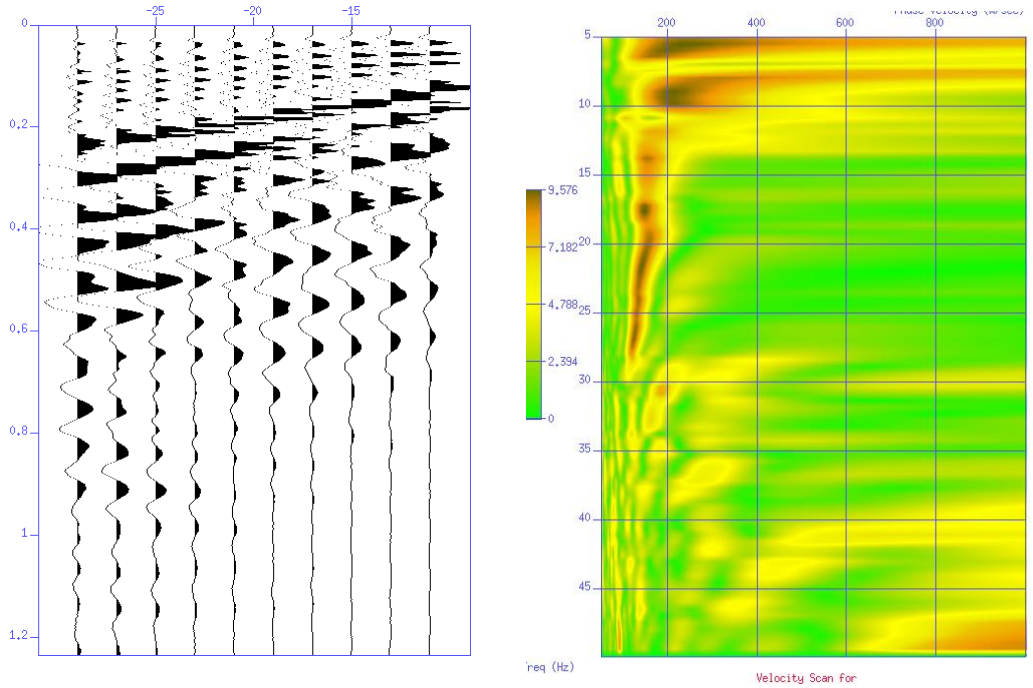

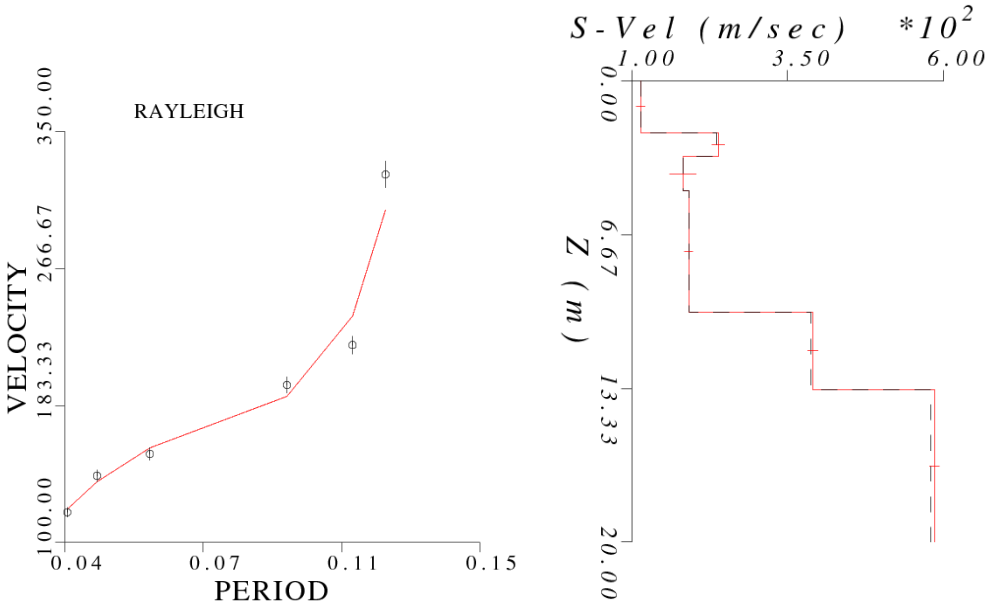

Distance receiver array: 15 – 35 m, 10 geophones. Distance source – first receiver: 10 m

Correlation coefficient: Layer 1 : 0.98

Layer 2 : 8.6E-02

Layer 3 : 0.45

Layer 4 : 0.96

Layer 5 : 5.7E-02

Layer 6 : 4.4E-02

Line3

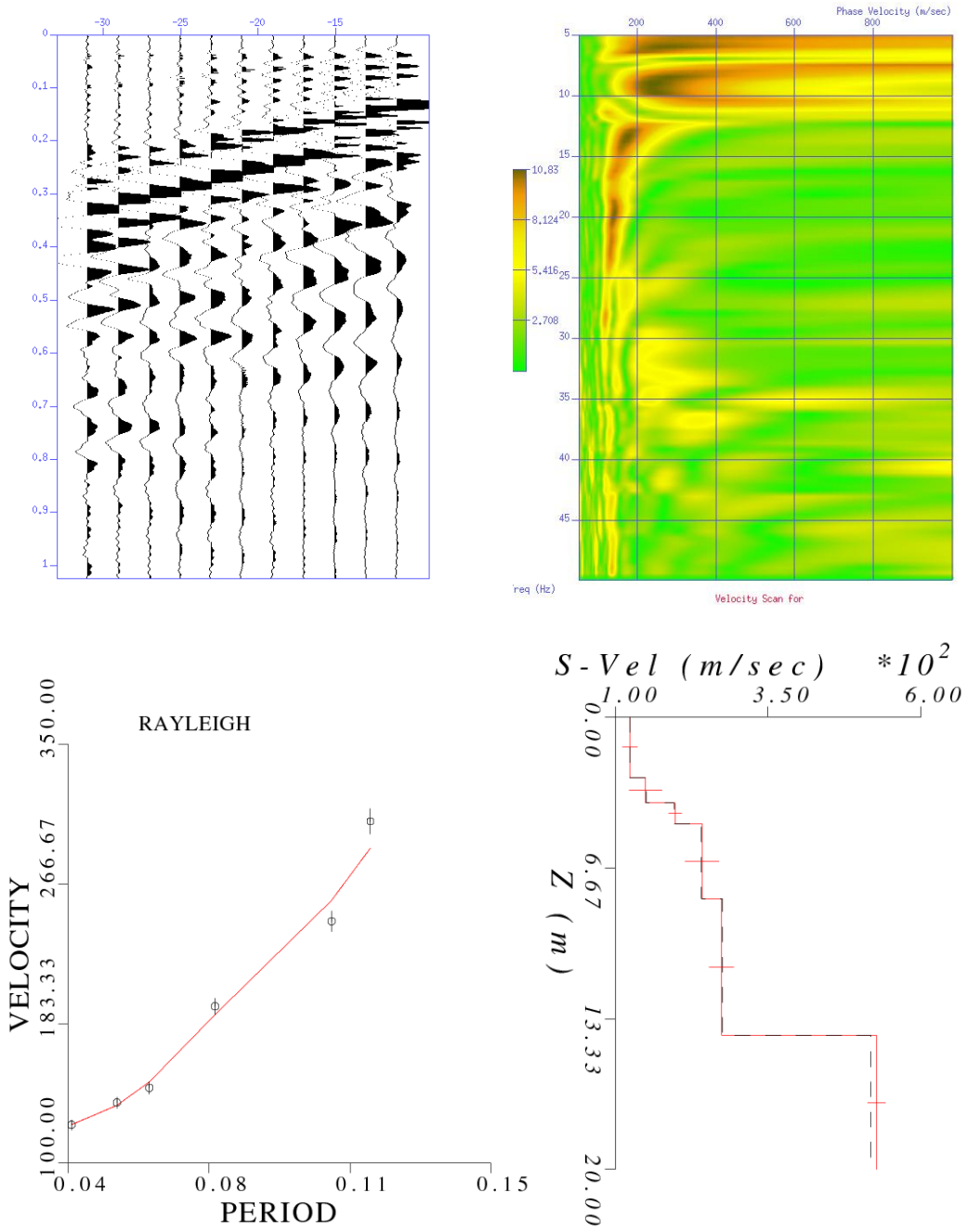

Distance receiver array: 20 – 40 m, 11 geophones. Distance source – first receiver: 11 m

Correlation coefficient: Layer 1 : 0.96

Layer 2 : 0.61

Layer 3 : 0.13

Layer 4 : 0.57

Layer 5 : 0.83

Layer 6 : 8.2E-02

Line3

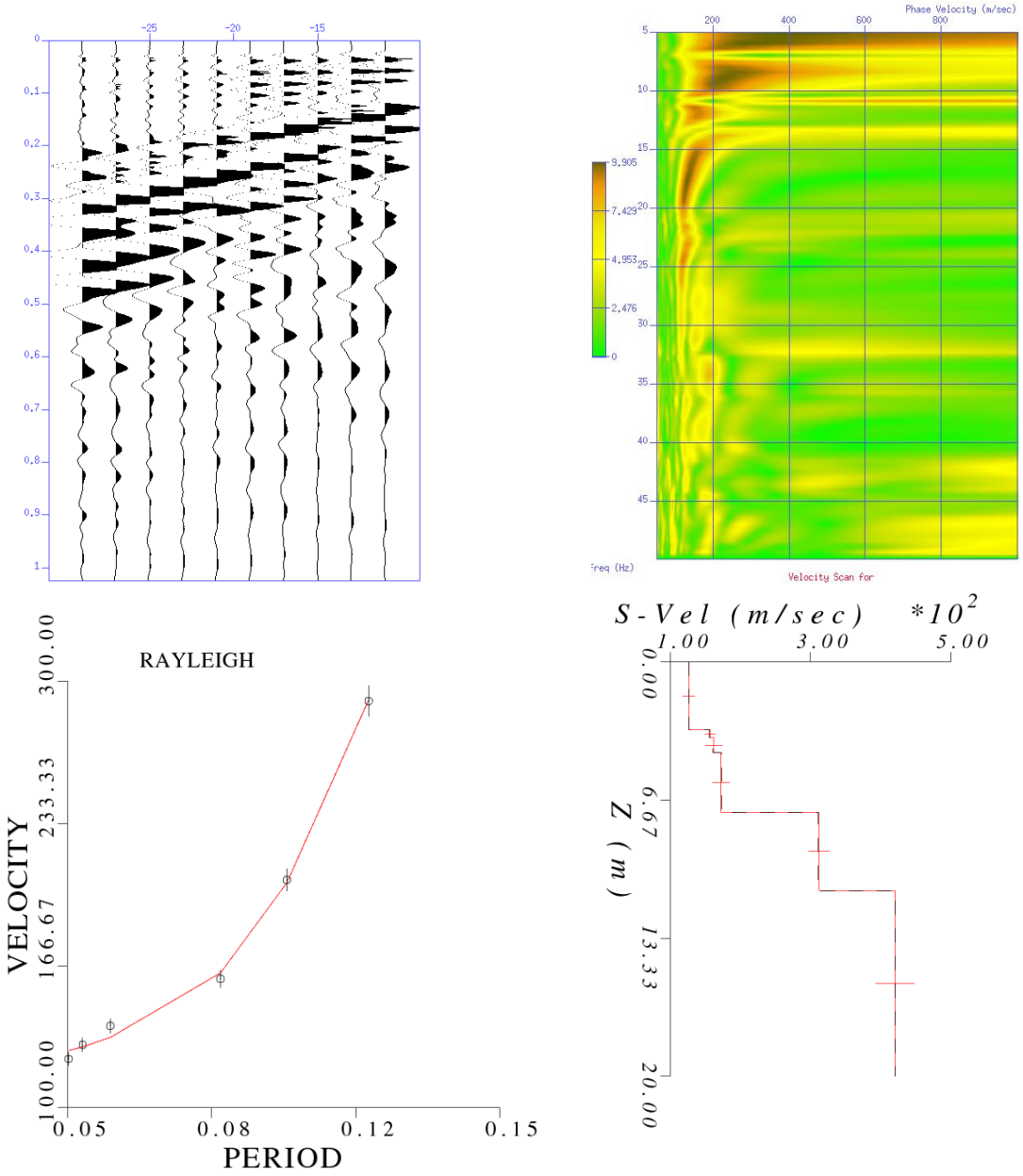

Distance receiver array: 25 – 45 m, 10 geophones. Distance source – first receiver: 10 m

Correlation coefficient:

Layer 1 : 0.98

Layer 2 : 2.9E-02

Layer 3 : 9.7E-02

Layer 4 : 0.87

Layer 5 : 0.1

Layer 6 : 0.28

Line3

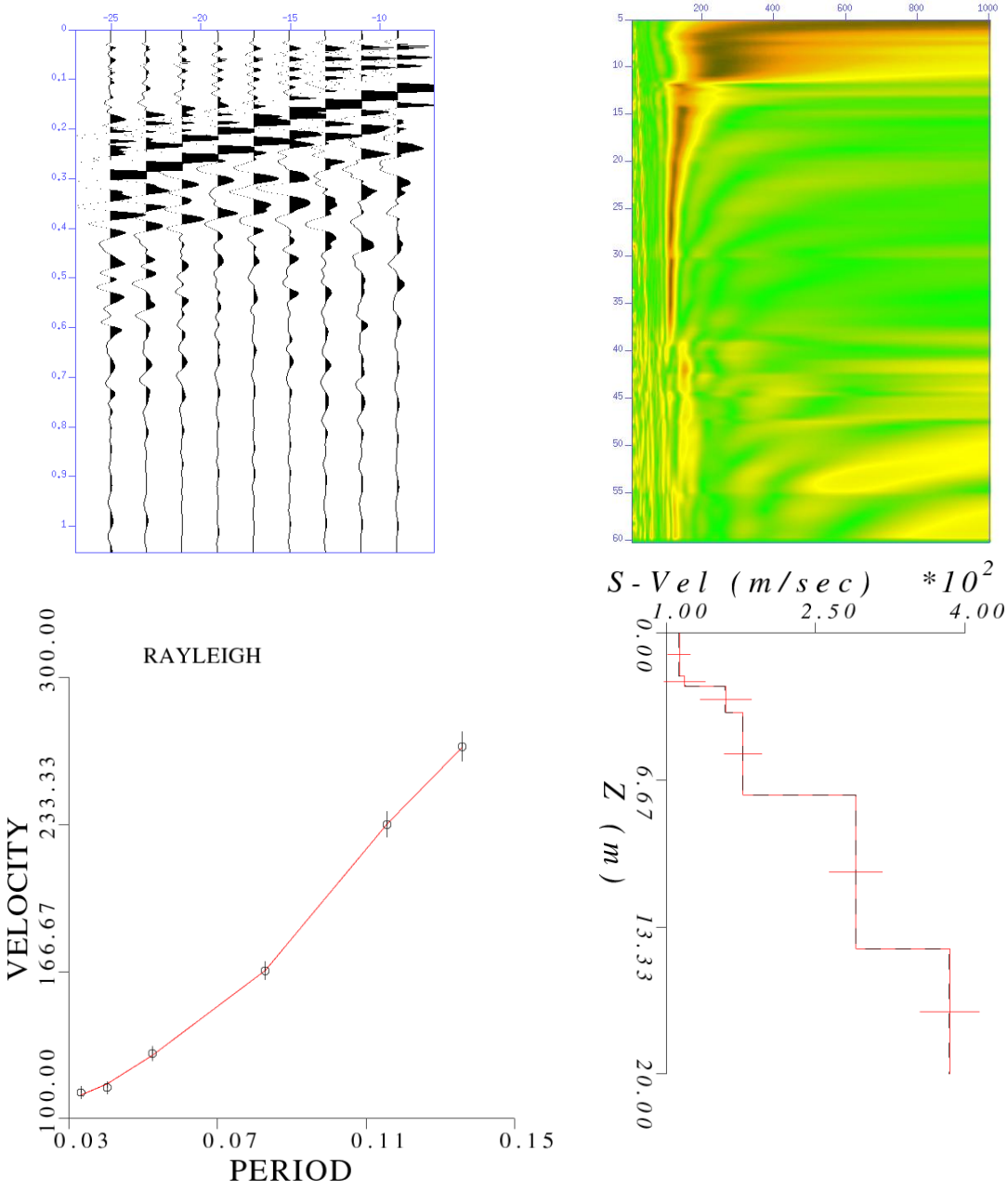

Distance receiver array: 30 – 46 m, 9 geophones. Distance source – first receiver: 9 m

Correlation coefficient: Layer 1 : 0.96

Layer 2 : 0.25

Layer 3 : 0.43

Layer 4 : 0.89

Layer 5 : 0.69

Layer 6 : 0.42

B.2 P-wave tomography by JaTS

Line1

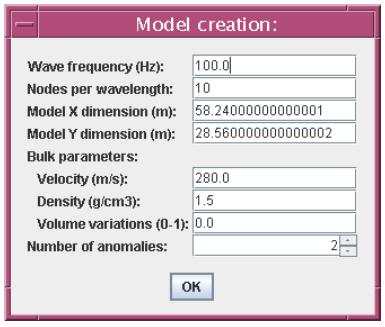

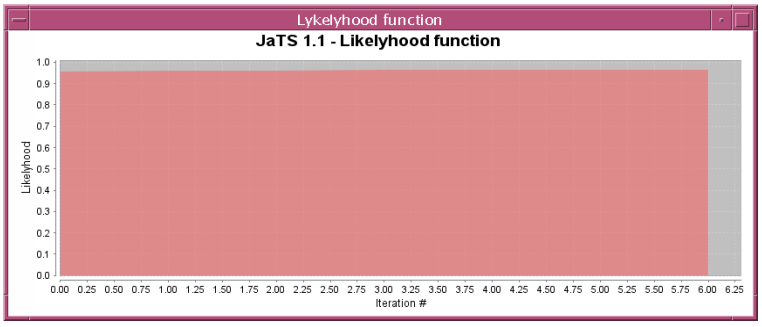

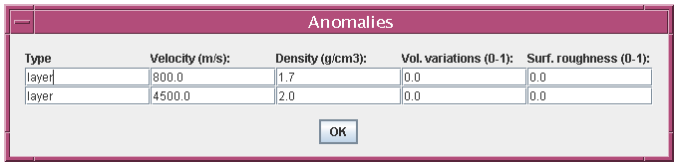

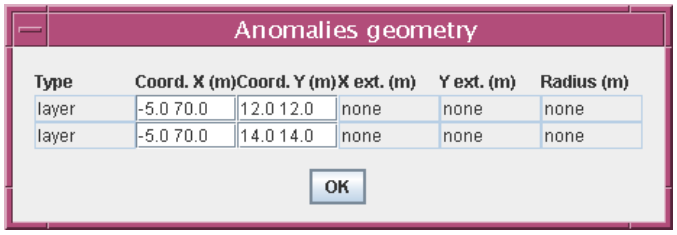

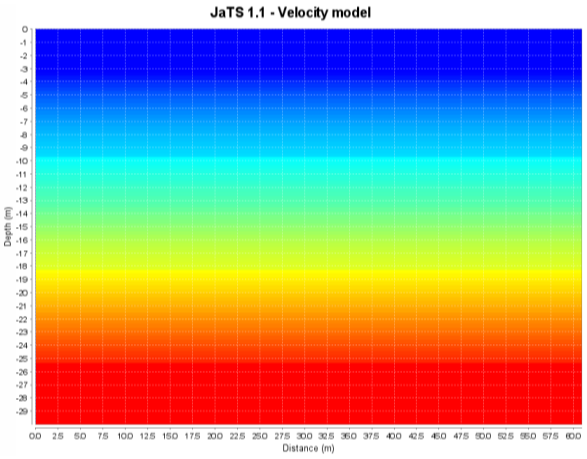

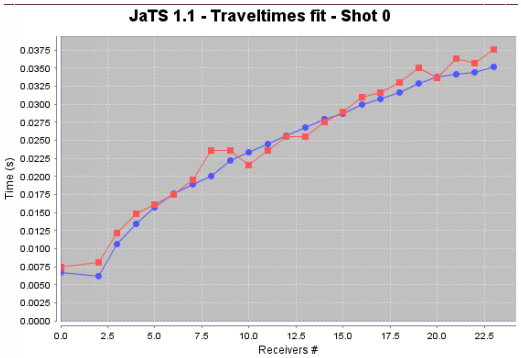

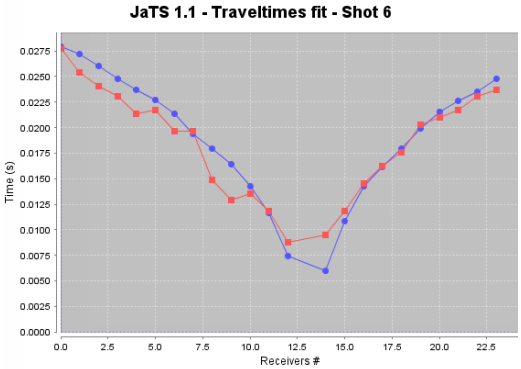

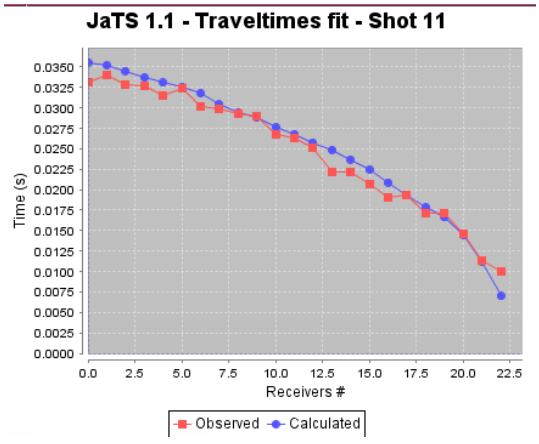

LEFT FIGURES: Initial model parameters with initial model at the bottom. Blue color represents a P-wave velocity of 280 m/s, red: 4500 m/s. Increasing velocity changes gradually.

RIGHT FIGURES: After velocity inversion. Top: Likelihood function: Likelihood between observed and calculated traveltimes.
Below: Comparison between observed and calculated traveltimes for three chosen shots.

Line2

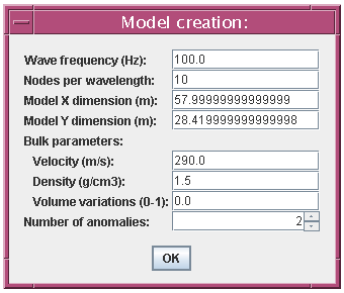

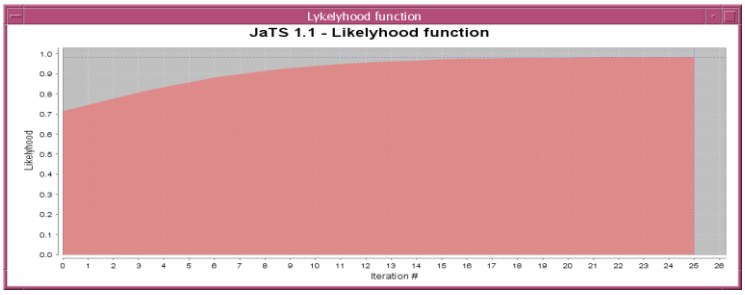

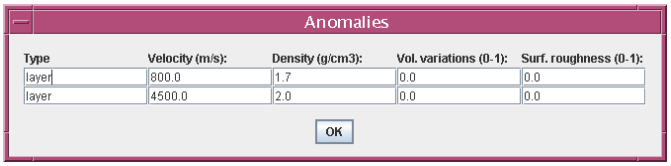

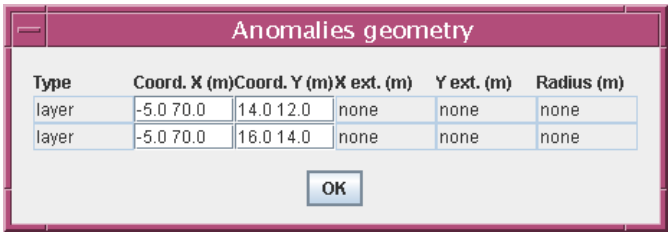

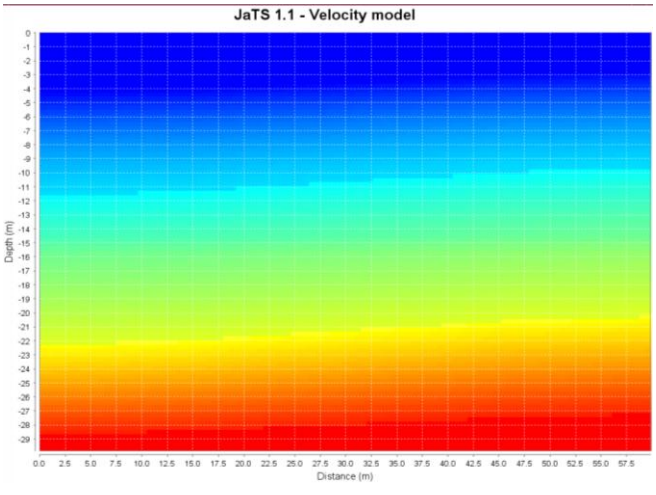

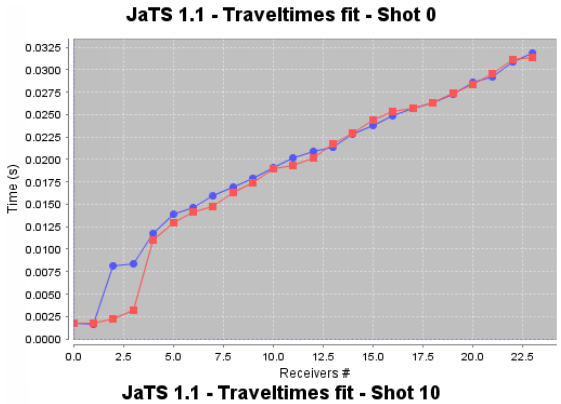

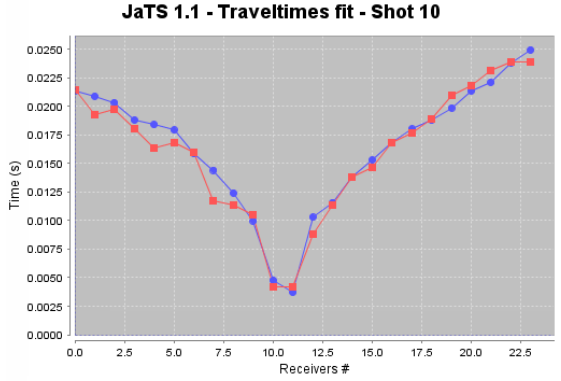

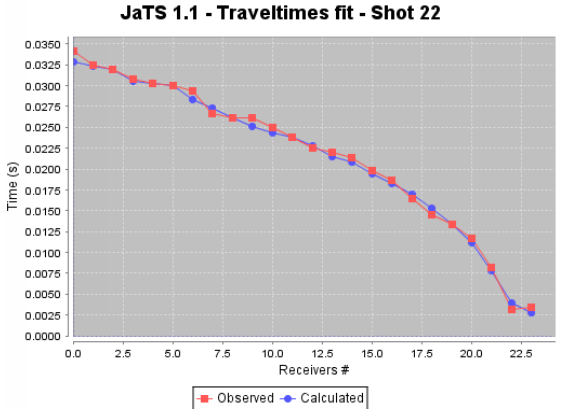

LEFT FIGURES: Initial model parameters with initial model at the bottom. Blue color represents a P-wave velocity of 100 m/s, red: 4500 m/s. Increasing velocity changes gradually.

RIGHT figures: After velocity inversion. Top: Likelihood function: Likelihood between observed and calculated traveltimes.
Below: Comparison between observed and calculated traveltimes for three chosen shots.

Line3

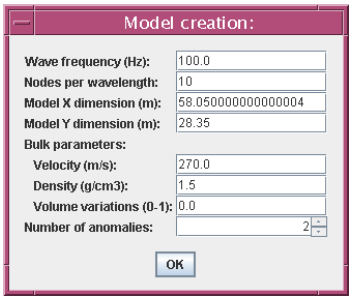

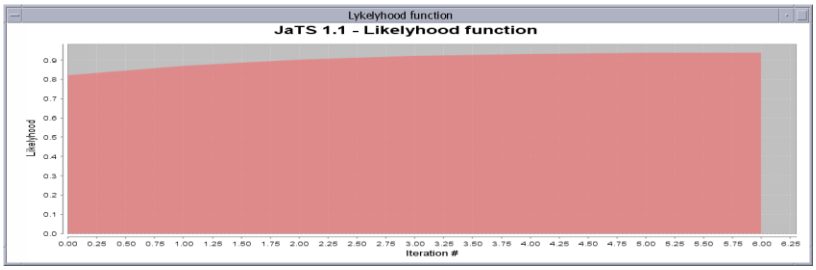

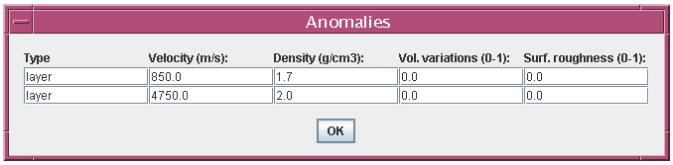

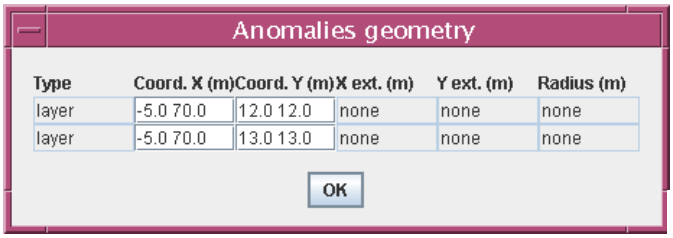

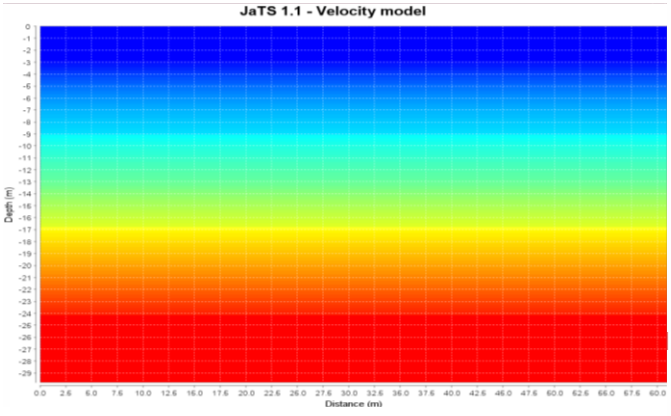

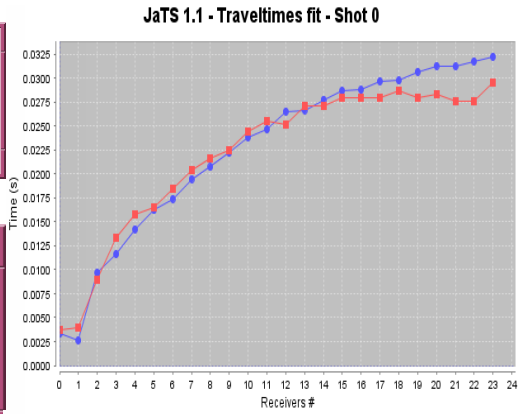

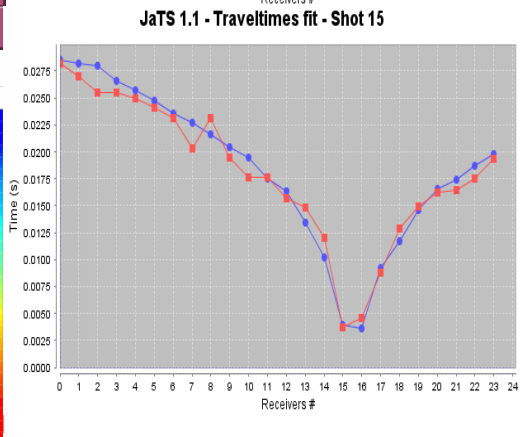

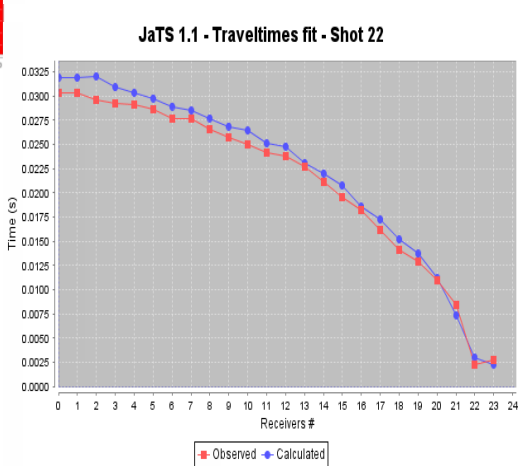

LEFT FIGURES: Initial model parameters with initial model at the bottom. Blue color represents a P-wave velocity of 270 m/s, red: 4750 m/s. Increasing velocity changes gradually.
RIGHT FIGURES: After velocity inversion. Top: Likelihood function: Likelihood between observed and calculated traveltimes. Below: Comparison between observed and calculated traveltimes for three chosen shots.

B.3 Resistivety measurements

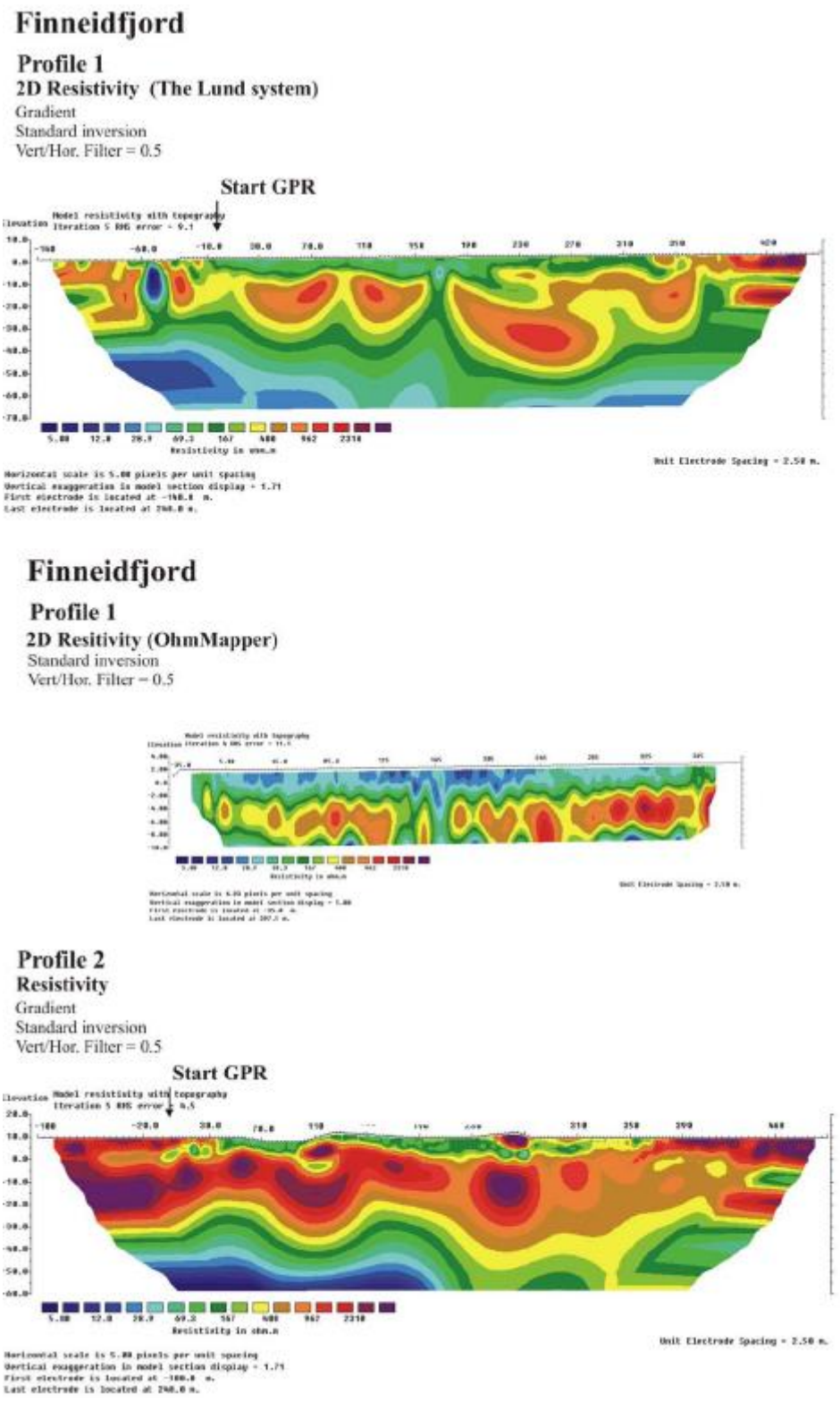

Top: Electrode-based system from the extended reference line (Fig. XX) using gradient configuration.
Middle: OhmMapper from the extended reference line (Fig. XX).
Bottom: Electrode-based system from a line parallel to the extended reference line but ~20 m further north, gradient configuration. All figures after Lecomte *et al.* (2008).

B.4 GPR CMP data

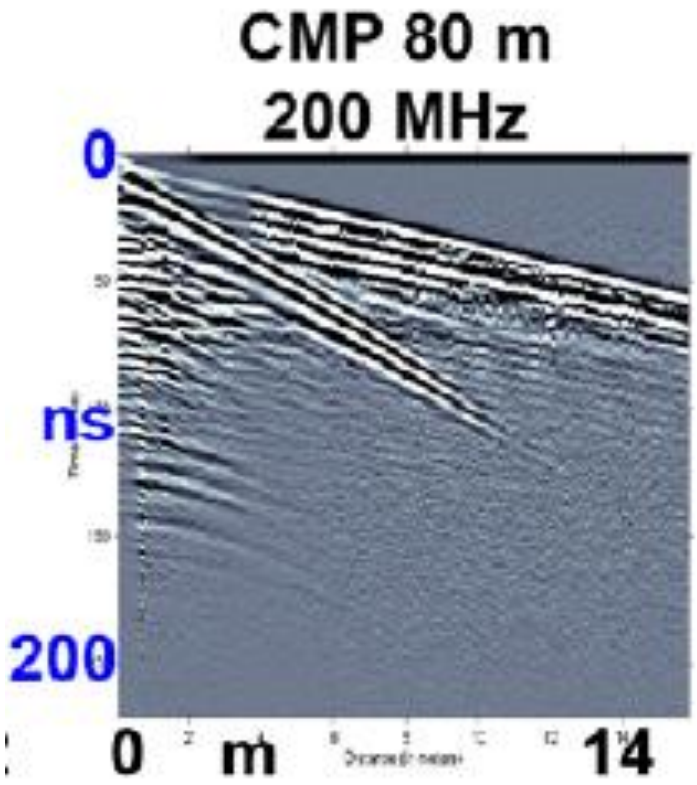

200 MHz GPR CMP data from distance 80 m on the reference profile (Fig 4.2) After Lecomte *et al.* (2008).